Implicit Large Eddy Simulation of Turbulent Duct Flows

Antonios Athanassios Mylonas

Submitted for the Degree of Ph.D.

Department of Fluid Mechanics and Computational Sciences
Cranfield University
Cranfield, UK

2010

Cranfield University

School of Engineering

PhD

Antonios Athanassios Mylonas

Implicit Large Eddy Simulation of Turbulent Duct Flows

Supervisors: Prof. Dimitris Drikakis and Dr. Evgeniy Shapiro

April, 2010

Abstract

Ducts can be found in ventilation systems, cooling ducts and blade passages of turbines, centrifugal pumps and many other engineering installations. The properties of the flow in ducts can significantly affect the performance and efficiency of these installation areas. The majority of the flows in ducts and engineering applications are turbulent.

The work presented in this thesis focuses on the analysis of turbulent flows inside square sectioned ducts and ducts with bends. The accuracy of three different high resolution high order schemes in the context of Implicit Large Eddy Simulation (ILES) is analysed. The influence of a low Mach limiting technique, Low Mach Number Treatment (LMNT) is also studied. The schemes employed are Monotonic Upwind Scheme for Scalar Conservation Laws (MUSCL) with a 2nd order Monotonized Central (MC) and 5th order limiter, and a 9th order Weighted Essential Non-Oscillatory (WENO) limiter.

The first case studied is a duct of square cross section . In the absence of experimental data for the duct case, the data from a plain channel flow is used to shed light on the results. The flow analysis points out the generation of secondary motions created by the existence of surrounding walls. All schemes employed lead to a similarly developed turbulent flow that is used to provide the turbulent boundary profile for the following case. LMNT proves to significantly assist MUSCL 2nd and 5th, that use it, in providing a turbulent profile similar to that of WENO 9th that did not employ the technique but is inherently less dissipative.

The second case under study is that of a square sectioned duct with a 90^o bend. The simulation output is in good agreement both qualitatively and quantitatively with the experimental data available in the literature. The generation of secondary flows inside the bend is observed without flow separation. Although the turbulent flow entering the domain is almost the same for all cases, differences between the schemes are noticed especially after the middle of the bend. LMNT leads to an overprediction of turbulence after that area for both schemes employing it while WENO 9th without LMNT provides the most accurate results compared to those provided by the experiment.

The results demonstrate applicability of ILES to strongly confined flows with secondary motions and shed light on cognitive properties of a wide range of state of the art schemes.

Acknowledgements

I should first thank Professor Dimitris Drikakis for offering me the unique opportunity of starting a PhD under his guidance and for his support, suggestions and priceless experience throughout this period. I would also like to thank Dr. Evgeniy Shapiro who was always eager to offer his time, help and support after just knocking on his door any time of the day. Professor Dimitris Drikakis along with Dr. Evgeniy Shapiro offered, besides their knowledge, guidance and experience, the psychological support needed for this work to reach its end.

My gratitude goes to Ioannis Kokkinakis who offered his help numerous times especially in the final stages of my study. His knowledge, experience, skills and friendship proved to be a moving force, leading me towards the end of the tunnel. Thanks also must go to all members of FMACS group since everyone was there to offer time and ideas whenever I needed them.

Special thanks go to my roommates and good friends Nikos Asproulis, Elias Tsoutsanis and Takis Tsoutsanis. Life would not be the same in Cranfield without them and Dimitris, Eleutheria, Vassilis, David, Xristos, Kwstas, Loukia, Dimitra (from back home) and all those who played even a small part in my life during this period. Need to thank Roy as well for offering me, in his own way, the help I needed in carrying on my work.

Last but certainly not least I would like to thank my family. Without their love and full support none of this would be possible. I do not think there is a way to thank my parents for all they have offered me except the promise that I will do my best to be as good a parent one day.

Dedicated to my Mother

Contents

List of Figures

List of Tables

Nomenclature

Symbols

μ	dynamic viscosity
δ_{ij}	Kronecker symbol
ϵ	rate of change of kinetic energy
γ	specific heat ratio
λ_b	bulk viscosity coefficient
$\mathbf{S}$	stress tensor
ν	kinematic viscosity
ρ	density
σ_{ij}	viscous stress tensor
ε	random number
c_p	heat at constant pressure
c_v	heat at constant volume
$F_{\omega'}$	flatness
f_i	forcing term
Q_m	mean flux
Re_τ	friction Reynolds
$S_{\omega'}$	skewness
U_0	centreline velocity
u_{rms}	turbulence intensity
v_{rms}	turbulence intensity

w_{rms}	turbulence intensity
e	energy
I	identity tensor
k	thermal conductivity
p	pressure
Pr	Prandtl number
q	heat flux
R	gas constant
Re	Reynolds Number
S	stress tensor
s	percent of perturbation
T	temperature
u	velocity

CHAPTER 1

Introduction and Objectives

1.1 Turbulent Flows

Turbulent flow is a fluid regime characterised by chaotic, stochastic property changes. A flow is usually turbulent when the inertial forces are significantly higher than the viscous ones. Although many before observed or studied turbulence its first representation using the physical properties of a fluid was that of Reynolds [1] who used a flow visualization technique in order to determine the onset of turbulence. It was his investigation that resulted in the parameter that indicates the ratio of inertial to viscous forces known as the Reynolds number.

Von Karman, Prandtl and Taylor made significant advances in the study of turbulence during the period between the two World Wars. Richardson described the physical behaviour of various sized eddies composing turbulence in the concept of energy cascade where energy transfer occurs from the large scales to the smaller, following a multi-stage procedure until energy is dissipated into heat [2]. The smallest scales in turbulence responsible for dissipating energy were determined by Kolmogorov [3].

Turbulent flow is characterised by a distribution of coherent vortical structures of various sizes and the vortex dynamics associated with the respective scales of the eddies.

Richardson's Hypothesis: From Richardson's point of view, the velocity and the size of the largest eddies present in the flow are comparable to the global scales of the mean flow. The Reynolds number for the largest scales is therefore comparable to the global Reynolds number, i.e. Re >> 1, and viscous forces have a negligible effect. Large eddies are mostly anisotropic and their shape is influenced by the boundary conditions. Very limited dissipation occurs at the large scale as the Reynolds number is sufficiently high. However, the energy of the large scale structures is transferred to small eddies generated due to instabilities, this process continues until the Reynolds number based on characteristic scale and velocity of the small eddies becomes sufficiently small for the viscous forces to

take precedence. This energy transfer is often illustrated in physical space as eddy break-up, where the inherently unstable coherent structures deform and evolve into eddies of smaller size (energy cascade).

Kolmogorov's Hypotheses and scales of turbulent flow: The idea of an energy cascade has been further developed by Kolmogorov [4]. The assumptions on the physical behaviour of the eddies made in Kolmogorov's hypotheses provide the framework for assessing the energy transfer rate and the scales involved in high Reynolds number, turbulent flows. Kolmogorov stated that the anisotropy, induced on the large scales by the boundary conditions, is gradually lost as the energy is transferred to progressively smaller eddies. The flow eventually becomes locally isotropic for the smallest scales of motion away from the boundaries and flow singularities; thus the small eddies have a statistically universal character common to all turbulent flows. The statistics mainly depend on the energy budget composed of the energy flux from the larger scales and viscous dissipation. Provided the small scales have a relatively short lifespan compared to the global time-scale, they are able to adapt quickly to the amount of energy received from the larger eddies and a dynamically balanced budget can be maintained. Based on Kolmogorov's hypotheses, considerations of dimensional analysis and energy transfer between the scales can be employed leading to the following expressions for the velocity, lengthscale and timescale of the smallest eddy, for which the local Reynolds number becomes equal to one:

$$u_\eta = (\epsilon\nu)^{\frac{1}{4}} \tag{1.1.1}$$

$$\eta = \nu^{\frac{3}{4}}\epsilon^{-\frac{1}{4}} \tag{1.1.2}$$

$$\tau_\eta = \nu^{\frac{1}{2}}\epsilon^{-\frac{1}{2}} \tag{1.1.3}$$

Here ν is the kinematic viscosity of the fluid and ϵ is the rate of change of the kinetic energy proportional to u_η^2/τ_η. The relation of the Kolmogorov scales $\left(\eta, u_\eta, \tau_\eta\right)$ to the large scales (τ_0, u_0, l_0) of the flow can then be expressed in terms of the large scale Reynolds number as follows:

$$\frac{\eta}{l_0} = Re^{-\frac{3}{4}} \tag{1.1.4}$$

$$\frac{u_\eta}{u_0} = Re^{-\frac{1}{4}} \tag{1.1.5}$$

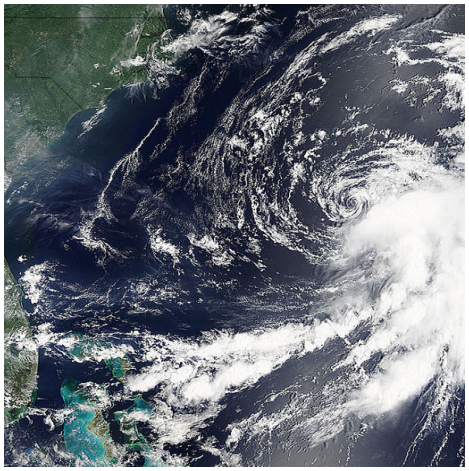

(a) Tropical Storm Franklin

(b) River flow

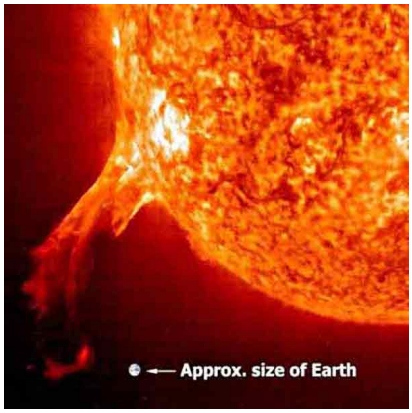

(c) Solar flare erupting from the sun

Figure 1.1: Turbulent flows in nature. (a) and (d) from http://www.nasa.gov, (b) from http://www.icwhen.com/ncc14/topics/waikato

$$\frac{\tau_\eta}{\tau_0} = Re^{-\frac{1}{2}} \tag{1.1.6}$$

The above indicates the degree of separation between the large scale and small scale motion in a high Reynolds number turbulent flow, which in turn results in significant challenges with respect to the computational modelling of turbulent flows.

Turbulent flows can be located anywhere in our surroundings in both natural and man-made flows. They exist in all kind of flows and from the smallest to the largest possible scales. The most intriguing phenomena can be found in nature such as meteorological phenomena like the formulation of tropical storms, see Figure 1.1(a). A simple flow like that of water in a river when meeting obstacles like rocks also presents many interesting characteristics, see Figure 1.1(b). An other interesting example is that of solar flares, see

(a) Airplane vortex

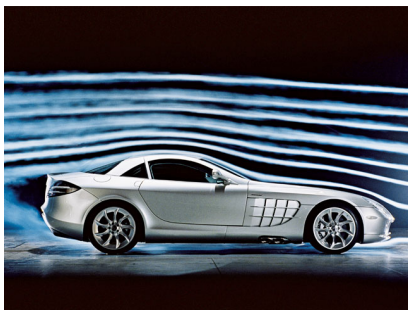

(b) Car aerodynamics

(c) Factory contaminant dispersion

Figure 1.2: Turbulent flows in Engineering. (a) to (c) from http://www.nasa.gov

Figure 1.1(c). Most, if not all, engineering flows that present interest for study are turbulent. Understanding turbulent flows plays a significant role in engineering design, optimisation and manufacturing. Aerodynamic drag due to turbulence for example is a major issue for automotive or airplane design and transportation in general, see Figures 1.2(a) and (b). Understanding turbulent flows can help studying cases like contaminant dispersion from factory emissions, see Figure 1.2(c), and solving many similar environmental issues.

Based on the vast number of applications mentioned above, turbulence can not be linked with a specific fluid. Every turbulent flow has, besides some common characteristics, certain unique ones based on its initial and boundary conditions. The randomness of the unsteady motion in both time and space is one of the most studied characteristics of turbulence. This randomness is why much of the research is based on statistical methods. Besides the chaotic motion, there is some organised motion that appears randomly at different points timewise or spatially. In these areas there is a high level of vorticity. Identifying and studying these phenomena is imperative in the prediction of turbulent flows. In this procedure large vortices gradually brake into smaller and smaller ones up to the point they dissipate into heat. Another characteristic of turbulent flows is large mixing capacity and rapid dispersion. Turbulence was and remains one of the most complex problems because of the random motion that makes an analytical method very difficult. This issue leads to the use of theoretical and numerical methods by simplifying the view of the problem. Although this concept is very useful for the study of turbulent flows it still can not be considered, in a way, an exact prediction of this kind of flows thus constant improvement of methods and techniques in the area of turbulent flows is necessary and makes their study imperative as well as very interesting and challenging.

1.2 Duct Flows

Flows in ducts, especially curved ones, are found in many different engineering problems [5] such as, heat transfer, chemical reactors, fluids transport piping systems, meandering rivers and other areas, equipment or devices [6]. Other cases related to duct flows are cooling ducts and blade passages of turbines [7], ventilators and centrifugal pumps [8]. The link to the internal environment is also significant because of ventilation systems and the need to provide comfortable and healthy conditions for the people inhabiting them [9]. For engineering applications of ducts the target is usually improved performance and efficiency. There is a great part of the literature that focuses on ventilation related flows so a small reference to those will follow before moving into other applications of ducts. Ventilation is of utmost importance in all internal environments. According to Koinakis [10], “ventilation should fulfil two basic objectives: (a) to remove the indoor pollutants and prevent the outdoor pollutants from entering, and (b) to control the indoor climate and the thermal comfort sense by intervening in the thermal balance”.

There is a large variety of cases and scenarios in the literature. Huang et al. [11]

studied the role of air in SARS transmission in Hong Kong. Their simulations showed that there is still room for improving isolation rooms in hospitals but with a significant cost. Although subways constitute an environment clearly dependent on the ventilation system and a possible target for terrorist attacks, there are only a few publications concerning the flow and ventilation inside such areas like the report submitted by Coke et al. [12]. This report was concerned with the creation of a model for the flow in the subway taking into consideration the complex subway system as well as the train motion. An interesting result of their research was that the train movement contributed to the fast expansion of contaminants to other stations. Li and Chow [13] conducted a research on the same area. Their research was concerned with the evaluation of the performance of tunnel ventilation safety systems using CFD. According to their results CFD can help in the development of tunnel ventilation systems by predicting different parameters such as vehicle emission dispersion, visibility and others. Another point they made is that simulating different fire scenarios could help the development of the system even more.

The aircraft cabin is also an area greatly dependent on duct ventilation systems since aircrafts have a closed ventilation system and in case of emergency, evacuation is, with only a few exceptions, impossible. At the same time aeroplanes are small spaces filled with humans, vulnerable to many and different dangers. The impact then if something goes wrong, especially during flight, can be enormous. Focusing on these facts, the flow provided in such an area through a ventilation system plays an important part and understanding its pattern and physics is necessary. A very interesting study of the turbulent flow inside the aircraft cabin, and its important link to the ventilation system, was conducted by Bosbach et al. [14, 15]. Their study aimed at the better understanding and optimisation of the airflow in an aircraft cabin based on numerical simulations and experimental validation based on data obtained through particle image velocity (PIV). The ventilation entrance used was of rectangular cross section and part of the duct was used in their study.

Although there are numerous cases studying internal flows linked to ventilation systems it is certainly not the only or most important application of duct flows. There is also interest in the differences between duct, channel and pipe flows. A lot of attention by many researchers when studying flows in ducts is given to heat transfer issues under transitional and turbulent flows [16]. According to Kazuhito [17] “turbulent heat and fluid flow through a passage with curvature has been one of the primary interests in the thermo-fluid engineering particularly, associated with heat exchanges and turbomachinery blading”. In such a case because of the curvature we have secondary motions affecting the turbulent strain field and consequently the level of heat transfer. The effects of a curve to the heat transfer compared to straight pipes were studied by Rosaguti et al. [18]. In their research they studied the geometric influences on the thermo-hydraulic performance of a serpentine channel of semi-circular cross-section with the results showing heat transfer enhancement.

The flow differences between pipes and square sectioned ducts were probably first studied by Nikuradse in 1926 [19]. Some numerical simulations were carried out in straight square ducts like the one by Gavrilakis [20] who studied low-Reynolds turbulent flows in straight square ducts. The results of this study had a satisfactory agreement with some ex-

perimental data at high Reynolds numbers and many flow characteristics were observed in the simulations that were not present in the experiments. This is justified by the fact that the experiments conducted could not capture well the low velocity characteristics thus making simulation results very important in order to have a better grasp of the flow physics in such geometry.

The literature around pipes, ducts and channels focuses a lot on curved geometries because of the nature of the flow and its interesting characteristics. Adding to that the fact that most of the areas mentioned before, that use ducts, have curved parts as well, the great importance of the study can be observed. In order to understand this interest of the scientific community the nature of such a flow must be examined. When a fluid element follows a curved streamline, it is influenced by an outward centrifugal force due to the curvature of the streamline [21]. This force is exactly balanced by an inward radial pressure gradient. In the case of a curved pipe flow we have an imbalance between the pressure gradient and the centrifugal force setting up a Dean-type secondary motion in the pipe. The fluid in the middle of the pipe moves outward, it collides to the outer wall and turns moving inwards along the top and bottom walls to merge at the inner wall [21]. It is therefore observed that even the laminar flow inside a curved pipe can be complex so the turbulent one will be very challenging. In his study, Ko [22] showed the conflict between improved heat transfer and the simultaneous increase in pressure loss concerning turbulent flown in curved pipes with regards to design parameters for improved performance as well.

Research on ducts and channels dates many years back. Experiments in such geometries were conducted from the mid 70s and their results are still being used for comparisons with up to date CFD studies. Laufer [23] conducted experiments on turbulent flows in channels at three different Reynolds numbers providing a descriptive picture of the energy diffusion in the centre region of the channel. Experiments in channel flows with a Reynolds range of 3,000 to 40,000 were conducted by Wei and Willmarth [24] using Laser Doppler Anemometry (LDA). The target of their experiments was testing the validity of the inner scaling laws in the range of these Reynolds numbers and the influence of different Reynolds numbers to the flow. They observed, amongst others, that the turbulent fluctuations became larger in amplitude with the increase of the Reynolds number. Melling and Whitelaw [25] conducted LDA experiments in a rectangular duct with a Reynolds number of 42,000. The main objective was to generate data and experimental results to be used for numerical models testing by the research community in the future. The experimental results produced were actually used for validation of CFD numerical methods in many papers that followed such as the one from Gessner and Emery [26]. Brundrett and Baines [27] studied the secondary flow in a square sectioned duct focusing on the Reynolds stress tensor. From their results they concluded that further studies are needed before the eddy structure which produces the Reynolds stress gradients can be predicted. Their most important conclusion was that the production of vorticity is associated with the relative proximity of an element of fluid to the wall of the duct [27].

Experiments on turbulent flows in circular curved ducts were performed by Sudo et al. [5], Enayet et al. [28] and Anwer et al. [21] aiming at better understanding the nature of the

flow in ducts with curvature. Humphrey and Whitelaw [29] studied the turbulent flow in a 90^o curved bend of square cross section and found out that the pressure driven secondary flows were much stronger than the stress driven ones. Taylor et al. [30] performed an experiment, using Laser Doppler Anemometry (LDA), on a square 90^o bend with a short upstream tangent. In their experiment they pointed out the importance of the boundary layer thickness at the entrance of the duct and the influence of the curvature to the development of the secondary motion. Using two-sensor hot-wire probes, Kim and Patel [31] measured the mean velocities and Reynold stresses for developing turbulent flow in a 90^o curved duct of rectangular cross-section. The number of numerical approaches for turbulent flows inside curved ducts are limited. One of the earliest numerical attempts to simulate this kind of flow was performed by Kreskovsky et al. [32]. The results were encouraging but not as close to the experimental ones as expected. Iacovides et al. [33] in a later study used the standard $k - \varepsilon$ eddy-viscosity model for a similar simulation. The study showed that the curvature induces a pair of counter-rotating vortices within the duct cross-section. The level of agreement in this simulation was much better.

Through the literature it is found that many different geometries and cases are studied using different methods. The difference in the geometry of a pipe can be spotted to the shape of the cross-section, the degrees of the bend etc. One of the geometries mostly studied is the duct with 180^o curve known also as a U-bend duct. Hidayat and Rasmuson [34] studied a non-isothermal gas-solid flow in a U-bend using the commercial software FLUENT, Nikas and Iacovides [35] studied the flow and heat transfer through a square-ended U-bend using low-Reynolds models. The same kind of geometry was used by Pruvost et al. [36] to study the effects of swirl motion on flow structure while Iacovides et al. [37] experimented using reflection-free differential second-moment (DSM) closures on a square-sectioned U-bend. A very interesting study was conducted by Iacovides [38] on stationary and rotating U-bends with rib-roughened surfaces.

Another geometry that presents a great interest is the 90^o bend known as the L-bend. Kuan et al. [39, 40] studied dilute gas-solid both for one and two-phase flows in a 90^o bend using a differential Reynolds stress model and validated their results using experimental data. Yang and Kuan [41] performed an experiment, investigating dilute turbulent particulate flow inside an L-bend using Laser Doppler Anemometry (LDA). Mokhtarzadeh-Dehgan and Yuan [42] measured the turbulence in developing turbulent boundary layers on the walls of a square L-bend. The pressure drop for turbulent single-phase fluid flow around sharp L-bend pipes was predicted by Crawford et al. [43].Other interesting cases include the study of flows in L-bends with spanwise rotation [44], scalar mixing in curved channels [45], flows in ducts with internal fins or ribbed passages [6, 46] and flows in internal cooling passages of turbine blades [47].

1.3 Implicit Large Eddy Simulation

There are many different ways of studying flows using CFD. The Direct Numerical Simulation (DNS) approach provides a complete time-dependent solution for turbulent flows. It provides superior accuracy because all scales of motion and time are resolved. On the other hand, the step-size of the discretised problem in time and space must be smaller than the characteristic time and the characteristic length of the smallest eddies present in the flow. The duration of the simulation and the size of the computational domain are based on the characteristic time and the characteristic length of the largest eddies. Since the range of scales observed in turbulent flows increases with progressively higher Reynolds number, it usually spans over several orders of magnitude (see Equations 1.1.4 to 1.1.6) hence the computational demands of this approach limit the practical applicability of DNS to high Reynolds number flows [48].

The most common approach to calculate a problem in engineering is the Reynolds Averaged Numerical Simulation. Reynolds averaging is based on the idea of decomposing the exact solution of the flow into an ensemble average and a fluctuating turbulent component. In the context of CFD simulations, ensemble averaging can be usually interpreted as a time averaging. In case of engineering applications, the controlled conditions such as inlet conditions in internal flows or free-stream conditions in external flows rarely change in time, thus time-averaging is preferred. Here, the resolved mean flow can be considered free of fluctuations and all the unsteadiness is contained in the unresolved turbulent scales that need to be modelled. The need for modelling results from the nonlinear nature of Navier-Stokes equations, which leads to appearance of the additional terms in equations, namely the Reynolds stress tensor, which introduces six additional unknowns. As a result, the averaged equations are always complemented by additional turbulence models that mimic the effects of the unsteady motions. Since this method requires the least possible amount of resources it gained enormous popularity in steady-state computations [49].

In unsteady flows, a time-scale associated with the organised unsteady motion exists and must be well separated from the time-scale of turbulent motion. Here, the exact solution can be seen as the sum of three contributing terms: the time average, the conditional average of the coherent motion and the random fluctuation due to turbulent motion. However, very few unsteady flows are guaranteed to exhibit deterministic low frequency motion that can, for example, be enforced externally through periodically changing inflow or free-stream conditions. If applicable, the conditional average in Unsteady Reynolds-Averaged Numerical Simulations (URANS) is therefore usually interpreted as a phase-averaged solution and the closure models are formally identical to the ones in steady-state computations [50].

The concept of Large-Eddy Simulations lies, in a sense, in between the above approaches with respect to accuracy and computational cost. In contrast to RANS, the equations of motion in classical Large-Eddy Simulations are filtered in space with respect to a filtering function. The flow field is then decomposed into an unsteady filtered compon-

ent and a fluctuating component. The latter, because of the nonlinearity of Navier Stokes equations is exhibited through the subgrid stress tensor appearing in the momentum conservation law. The larger turbulent structures then are described by the filtered flow field and directly resolved, whereas the subgrid stress tensor incorporating fluctuating components has to be modelled. This involves careful and detailed modelling, especially in the near-wall flow region [51]. Similar to the Direct Numerical Simulations, Large-Eddy Simulations provide a fully three-dimensional, time-dependent solution. As demonstrated previously, the grid requirements for DNS strongly depend on the smallest scales present in the flow, but most of the turbulent kinetic energy is contained in the larger structures. Therefore, while computing the large-scale dynamics of the flow directly, LES significantly reduces the total computing time by modelling the less energetic, but computationally demanding, small scales [52].

In the cases addressed in this thesis, based on the Reynolds number along with the experimental data available, the flows under study are turbulent. Furthermore, the Reynolds numbers considered are quite high, which prompts the application of LES. More precisely, the current thesis focuses on a particular variation of LES approach, namely Implicit Large Eddy Simulation (ILES). The numerical framework for this research is provided by an Eulerian type, unsteady, three-dimensional, compressible Navier-Stokes solver. Although both cases can be deemed incompressible, using a low Mach number coupled with a Low Mach Number Treatment technique makes this method an appropriate tool for this work. The framework that has been developed inhouse has a block-structured finite volume approach, formulated in a generalised curvilinear coordinate system. Several techniques for the discretisation in time and space are present.

The ILES approach employed here differs greatly from the classic LES one because unresolved subgrid effects are not explicitly modelled. Classically, the effects of unresolved scales are modelled in their entirety [53]. In that approach, the numerical methods should be as unobtrusive as possible. This means that approximation effects (i.e. truncation errors) should be as small as possible [53].

Figure 1.3 shows a flowchart of how theory, modelling and numerical methods interact in LES and ILES [53]. With ILES, the model and numerics are merged with the modelling, using theoretical foundations in vanishing viscosity to select entropy-satisfying weak solutions [53].

Hebrard et al. [54] used LES to study the turbulent flow in a duct with a bend and measured the heating and curvature effects. Guleren and Turan [55] used LES for strongly curved stationary and rotating U-duct flows. Finally Qin and Pletcher [56] used LES to study the turbulent heat transfer in a rotating square duct. All these studies are very recent and the use of LES methods for simulating flows of this kind is something new and under development. Although the past few years the number of studies around turbulent flows in curved ducts has increased, compared to a few years back [57], there is still a lot of room for further research. Considering the nature and the distinctive features of the flow in such geometry plus the fact that there are not any ILES studies in this area, performing

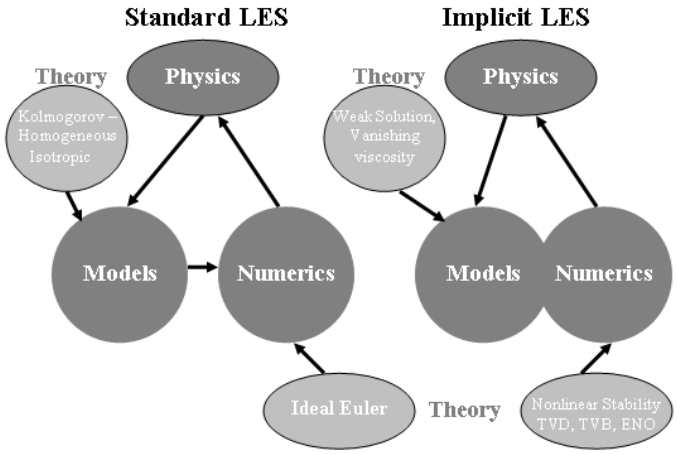

Figure 1.3: Fundamental similarities in the modelling approaches described and analysed. In both cases some more fundamental theoretical results are used to define models

computations in this framework presents a challenging and very interesting task. In order to better understand the ILES method used, as it is described in chapter 3, we should take a look at the literature regarding this kind of methods.

Conventional LES procedure involves the filtering of the large scales and explicit subgrid-scale (SGS) modelling in order to close the low-pass filtered equations [58]. The SGS stress tensor along with the commutation error term and the truncation error are added to the Navier Stokes equations. This model however has some drawbacks because structural models are too expensive (computationally) and not dissipative enough [58]. These drawbacks lead to the use of mixed models that combine this model with an eddy-viscosity one. Moreover these mixed models are computationally complex and more expensive when dealing with high Reynolds numbers [58, 59].

Because of the drawbacks connected with the traditional LES model and based on an idea for shock capturing presented by Von Neumann and Richmyer in the 50's, the scientific community started using implicit SGS models. The models of this type, primarily introduced by Boris et al. [60] are named Implicit Large Eddy Simulation (ILES). The interest in ILES the past few years is constantly increasing. The absence of explicit parameters in ILES increases the predictiveness in simulations [61]. In ILES dissipative properties of certain classes of schemes are utilised in order to mimick the dissipation introducted through the subgrid stress tensor in classical LES. Namely, the dissipation resulting from the truncation error is acting as an energy sink corresponding to small scales resulting in the correct representation of small scales in the numerical solution. A number of classes of schemes have been shown in the past to possess adequate dissipative properties and deliver ILES capability. For example MPDATA family of schemes used in the atmospheric research community [52], Flux Vector Split [59], ALDM schemes [62] and high resolution, higher order class of schemes which are the focus of the current thesis [53].

Looking into the literature focused on ILES one can find successful applications of ILES approach in a number of engineering problems including:

- Single and multi-component turbulent mixing [63–65]
- Aerospace applications and external flows [66]
- Environmental flows [67, 68]
- Marine hydrodynamics [69]
- Internal channel flows [1, 62, 70, 71]
- Geophysical flows [72]

to name but a few. The results so far for modelling turbulent flows using ILES are encouraging for the future of the method. However for both Classical and Implicit LES, modelling of wall-bounded flows dominated by the viscous interaction at the wall presents a number of challenges [53]. In particular for ILES the question of the adequacy of the dissipation introduced through the numerical scheme for wall bounded flows is important [1]. The classical flow in a curved bend features strong dependence on near wall phenomena as well as a plethora of secondary flows thus presenting an excellent benchmark case for the investigation of the behaviour of ILES schemes. There are many experiments in this area, however so far, to our knowledge, there have been no attempt to investigate this problem using ILES, which prompted the development of this thesis.

1.4 Aims and Objectives

Following the literature review it is understood that there are still a lot of areas concerning turbulent flows and the available computation techniques to be researched. The case of the curved bend presents a challenging area of study because of its link to so many different areas, as pointed out in the previous sections. Also the limited number of studies, using ILES, adds to the importance of the research.

The aim of the current PhD project is to study turbulent flows in ducts and investigate the applicability and properties of different ILES models. More specifically the project's objectives are to:

- Investigate physics of turbulent flows and applicability of ILES models for straight ducts
- Understand and analyse the physics of the flow in ducts with bends

- Investigate different solution strategies based on high-order, high-resolution methods for ducts with bends
- Assess the influence of Low Mach Number Treatment

In the following chapter the methodology used to conduct this research is presented.

Chapter 3 includes the study of the flow in a straight duct with periodic boundary conditions and the analysis of the influence of four walls and corners in this kind of a flow.

In chapter 4 the study for the L-bend duct is presented in comparison with experiments and the flow physics are analysed.

The research concludes with chapter 5 where the findings are summarised and the possibilities for further research in this area are described.

CHAPTER 2

Methodology

Further to the involvement of turbulent flows, secondary flows are also present in the cases under study. In flows like the ones in question, high gradients are frequently encountered, along with rapidly fluctuating components leading to the use of a simple explicit time integration method as the ideal one. Different non-linear schemes with a reconstruction step are used to achieve high-resolution. Finally, the code version used is fully parallelised (through a domain decomposition technique). The inhouse code used is CNS3D and it has been developed over a period of more than 20 years with several key publications outlining the computational methods and models contained within the code [53, 73–78]. It should be noted that the high resolution, high-order methods can not be found in commercially available software over 3rd order like for example ANSYS FLUENT. The computational code has been validated and used for a wide variety of simulations featuring flow physics such as low and high speed flows, shock waves, mixing of fluids, unsteady attached and separated flows, multi-component flows to name but a few eg [66, 70, 79].

In this research project, besides the inhouse code for the simulations, Gridgen V15.11 software will be used for the structured grid generation along with some inhouse codes to add boundary conditions. This brakes the geometry into blocks, thus bringing the grid in the desired form to be utilised by the Implicit Large Eddy Simulation (ILES) inhouse code in its fully parallelised version.

2.1 The Governing Equations

The Navier-Stokes Equations (NSE) govern the physics of all (Newtonian) fluid flows. The set of NSE (continuity, momentum and energy equations) in their differential form is as follows:

$$\frac{\partial \rho}{\partial t} + \nabla \cdot (\rho \mathbf{u}) = 0 \tag{2.1.1}$$

$$\frac{\partial \rho \mathbf{u}}{\partial t} + \nabla \cdot (\rho \mathbf{u} \otimes \mathbf{u}) = -\nabla \cdot \mathbf{S} \tag{2.1.2}$$

$$\frac{\partial e}{\partial t} + \nabla \cdot (e\mathbf{u}) = -\nabla \cdot (\mathbf{S} \cdot \mathbf{u}) - \nabla \cdot \mathbf{q} \tag{2.1.3}$$

where $\mathbf{u}$, ρ, e, and $\mathbf{q}$ stand for the velocity components, the density, the total energy per unit volume, and the heat flux, respectively. The stress tensor $\mathbf{S}$ represents the effects of the thermodynamic pressure p and the viscous stresses, yielding

$$\mathbf{S} = p\mathbf{I} - \lambda_b(\nabla \cdot \mathbf{u})\mathbf{I} - \mu[(\nabla \mathbf{u}) + (\nabla \mathbf{u})^T] \,, \tag{2.1.4}$$

where $\mathbf{I}$ is the identity tensor, μ is the dynamic viscosity coefficient relating the stress to the rate of strain for a Newtonian fluid and λ_b is the bulk viscosity coefficient accounting for the dilatation of the fluid. The bulk viscosity coefficient is defined according to the Stokes hypothesis as:

$$\lambda_b = -\frac{2}{3}\mu \,. \tag{2.1.5}$$

Because of the temperature differences in the flow the heat flux occurring can be linked to the temperature gradients based on Fourier's heat conduction law

$$\mathbf{q} = -\kappa \nabla T \,, \tag{2.1.6}$$

For a specific gas, the specific heats at constant pressure c_p and constant volume c_v are related by:

$$c_p - c_v = R$$

where R is the gas constant equal to $287.05^{J}/_{kg \cdot K}$ for air and

$$\gamma = \frac{c_p}{c_v}$$

where γ is the specific heat ratio and equals 1.4 under standard atmospheric conditions for air.

The above are also defined as:

$$c_p = \frac{\gamma R}{\gamma - 1}$$

and

$$c_v = \frac{R}{\gamma - 1}$$

The total density-energy is then given by:

$$\rho E = \rho e + \frac{\rho}{2}\left(u^2 + v^2 + w^2\right) \tag{2.1.7}$$

where e stands for the internal energy. The calorific equation of state is used in order to calculate the internal energy:

$$e = c_v T = \frac{RT}{\gamma - 1} = \frac{\rho RT}{\rho\left(\gamma - 1\right)} = \frac{p}{\rho\left(\gamma - 1\right)} \tag{2.1.8}$$

where c_v is the specific heat at constant volume, e is the internal energy and T is the absolute temperature.

Equation of State:

The equation of state for a perfect gas with negligible inter-molecular forces is used:

$$p = \rho RT \tag{2.1.9}$$

with R being typically equal to $287.05\,\mathrm{Nm/(kg \cdot K)}$ for air and T standing for temperature.

Diffusion Coefficients: The diffusion coefficients are comprised of the thermal conductivity k, and the viscous coefficients λ and μ which are related to the thermodynamic variables by means of kinetic gas theory. Several of the assumptions on which their derivation is based are semi-empirical in nature with a detailed account of their derivation given by Schlichting [19]. The Prandtl number Pr can be calculated and is identified as

$$Pr = \frac{\mu c_p}{k} \tag{2.1.10}$$

Sutherland's Law: The physical properties of the flow with Sutherland's law for the variation of the dynamic viscosity coefficient μ, with the air temperature T, results:

$$\frac{\mu}{\mu_0} = \left(\frac{T}{T_0}\right)^{3/2} \frac{T_0 + S_u}{T + S_u} \tag{2.1.11}$$

where T and S_u are in Kelvin and μ_0 is a reference viscosity at a reference temperature T_0. In most cases, the reference values for viscosity and temperature are taken at standard atmospheric conditions at sea level, thus $\mu_0 = 1.7894 \times 10^{-5} kg/\left(m \cdot s\right)$ and $T_0 = 288.16K$. Moreover the Sutherland temperature is taken as $S_u = 110.4K$. All the above assume air as the working medium.

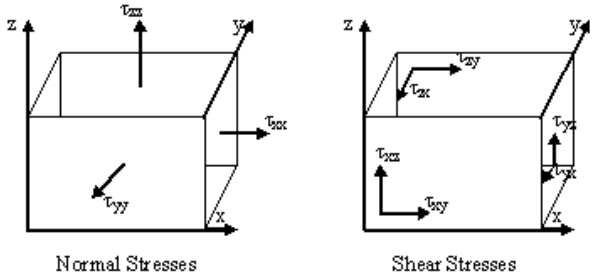

Figure 2.1: Stresses

Shear and Normal Stresses: The viscous stresses arise from the friction between the fluid and the surface of an element and is described by the stress tensor **T**. In Cartesian coordinates the general form is given as

$$\mathbf{T} = \begin{bmatrix} \tau_{xx} & \tau_{xy} & \tau_{xz} \\ \tau_{yx} & \tau_{yy} & \tau_{yz} \\ \tau_{zx} & \tau_{zy} & \tau_{zz} \end{bmatrix} \tag{2.1.12}$$

where the first subscript character denotes the axis at which the plane is perpendicular to and the second character depicts the direction of the stress on that plane as shown below in Figure 2.1. Stresses with identical characters in their subscript denote normal stresses whereas otherwise denote shear stresses.

The computation of the shear stresses depends on the dynamical properties of the medium considered. Assuming air, Isaac Newton stated that the shear stress is proportional to the velocity gradient. Hence, a fluid of such attribute is referred to as a *Newtonian Fluid*. For a Newtonian fluid such as air, the components of the viscous stress tensor (as derived by George Stokes) are given by the following relations:

$$\begin{aligned} \tau_{xx} &= \lambda_b \left(\frac{\partial u}{\partial x} + \frac{\partial v}{\partial y} + \frac{\partial w}{\partial z} \right) + 2\mu \frac{\partial u}{\partial x} \\ \tau_{yy} &= \lambda_b \left(\frac{\partial u}{\partial x} + \frac{\partial v}{\partial y} + \frac{\partial w}{\partial z} \right) + 2\mu \frac{\partial v}{\partial y} \\ \tau_{zz} &= \lambda_b \left(\frac{\partial u}{\partial x} + \frac{\partial v}{\partial y} + \frac{\partial w}{\partial z} \right) + 2\mu \frac{\partial w}{\partial z} \\ \tau_{xy} &= \tau_{yx} = \mu \left(\frac{\partial u}{\partial y} + \frac{\partial v}{\partial x} \right) \\ \tau_{xz} &= \tau_{zx} = \mu \left(\frac{\partial u}{\partial z} + \frac{\partial w}{\partial x} \right) \\ \tau_{yz} &= \tau_{zy} = \mu \left(\frac{\partial v}{\partial z} + \frac{\partial w}{\partial y} \right) \end{aligned} \tag{2.1.13}$$

Applying 2.1.5 to the normal stresses gives:

$$\begin{aligned}\tau_{xx} &= 2\mu\left(\frac{\partial u}{\partial x} - \frac{1}{3}\nabla\cdot\mathbf{u}\right)\\ \tau_{yy} &= 2\mu\left(\frac{\partial v}{\partial y} - \frac{1}{3}\nabla\cdot\mathbf{u}\right)\\ \tau_{zz} &= 2\mu\left(\frac{\partial w}{\partial z} - \frac{1}{3}\nabla\cdot\mathbf{u}\right)\end{aligned} \tag{2.1.14}$$

2.1.1 Dimensionless Form

In Computational Fluid Dynamics, the Navier-Stokes Equations (2.1.1) to (2.1.3) are commonly used in their dimensionless form. This procedure simplifies the physical system by removing the units of the variables. This results to a reduction of the number of parameters used and facilitates the comparison with experimental data, turning the decreased number of parameters characterising the flow to a significant advantage.

The non-dimensionalisation is achieved by relating all quantities to characteristic reference values for the density (ρ_c), velocity (u_c), dynamic viscosity (μ_c) and length (l_c). Time is non-dimesionalised by the characteristic flow time l_c/u_c. After this procedure we get the following set of dimensionless variables:

$$\begin{aligned} t^* &= \frac{t}{l_c/u_c}, & x^* &= \frac{x}{l_c}, & y^* &= \frac{y}{l_c}, & z^* &= \frac{z}{l_c},\\ \rho^* &= \frac{\rho}{\rho_c}, & u^* &= \frac{u}{u_c}, & v^* &= \frac{v}{u_c}, & w^* &= \frac{w}{u_c},\\ e^* &= \frac{e}{\rho_c u_c^2}, & p^* &= \frac{p}{\rho_c u_c^2}, & \mu^* &= \frac{\mu}{\mu_c}. \end{aligned} \tag{2.1.15}$$

An additional characteristic value T_c for the temperature is needed in order to obtain a dimensionless heat flux for energy conservation. With Equations (2.1.6) and (2.1.10), the heat flux in the non-dimensional form of Equation (2.1.3) can now be written as:

$$\mathbf{q}^* = -\frac{c_v\gamma}{Re\,Pr}\frac{T_c}{u_c^2}\nabla T^*\,, \tag{2.1.16}$$

where Re is the Reynolds number given by:

$$Re = \frac{\rho_c u_c l_c}{\mu_c}\,. \tag{2.1.17}$$

The reference velocity u_c and the reference Temperature T_c are chosen to satisfy:

$$c_v\rho_\infty T_c = e_\infty = \rho_\infty u_c^2\,, \tag{2.1.18}$$

where the subscript ∞ refers to the properties of the free-stream. For a perfect gas, this leads to the following definitions for u_c and T_c

$$u_c = a_\infty \sqrt{\frac{1+\frac{\gamma}{2}(\gamma-1)Ma_\infty^2}{\gamma(\gamma-1)}} , \tag{2.1.19}$$

$$T_c = \frac{a_\infty^2}{c_v}\frac{1+\frac{\gamma}{2}(\gamma-1)Ma_\infty^2}{\gamma(\gamma-1)} , \tag{2.1.20}$$

where $a_\infty = \sqrt{\gamma p_\infty/\rho_\infty}$ is the speed of sound and $Ma_\infty = u_\infty/a_\infty$ is the Mach number. Based on the above, Equation (2.1.16) can now be simplified to:

$$\mathbf{q}^* = -\frac{\gamma}{Re\,Pr}\nabla T^* . \tag{2.1.21}$$

l_c , which is the reference value, can be replaced with any length representing the characteristic dimensions of the case studied with the reference density being equal to the free-stream density $\rho_c = \rho_\infty$. Finally, in order to ensure consistency between the numerical Reynolds number and the experimental Reynolds number, the characteristic viscosity μ_c is defined as:

$$\mu_c = \frac{u_c}{u_\infty}\mu_\infty . \tag{2.1.22}$$

The above equation is used to achieve the necessary Mach and Reynolds numbers simultaneously and is only a convenient scaling equation.

Replacing the above relations into the Navier-Stokes Equations (2.1.1) to (2.1.3) yields their dimensionless form:

$$\frac{\partial \rho^*}{\partial t^*} + \nabla\cdot(\rho\mathbf{u}^*) = 0 , \tag{2.1.23}$$

$$\frac{\partial \rho^*\mathbf{u}^*}{\partial t^*} + \nabla\cdot(\rho^*\mathbf{u}^*\otimes\mathbf{u}^*) = -\nabla\cdot\mathbf{S}^* , \tag{2.1.24}$$

$$\frac{\partial e^*}{\partial t^*} + \nabla\cdot(e^*\mathbf{u}^*) = -\nabla\cdot(\mathbf{S}^*\cdot\mathbf{u}^*) - \nabla\cdot\mathbf{q}^* , \tag{2.1.25}$$

$\mathbf{S}^*$ being the nondimensional stress tensor:

$$\mathbf{S}^* = p^*\mathbf{I} + \frac{2}{3\,Re}(\nabla\cdot\mathbf{u}^*)\mathbf{I} - \frac{1}{Re}[(\nabla\mathbf{u}^*) + (\nabla\mathbf{u}^*)^T] . \tag{2.1.26}$$

Here, the nabla operator ∇ denotes the gradients and vector derivatives with respect to the dimensionless coordinates x^*, y^* and z^*. In the following sections the supercript $*$ does not appear for simplicity reasons.

2.1.2 Matrix Form

In order to simplify and organise the logic into a computational method, Equations (2.1.23) to (2.1.25) are written in conservative Cartesian matrix form, resulting in a single equation representing the entire system of governing equations:

$$\frac{\partial \mathbf{U}}{\partial t} + \frac{\partial \mathbf{E}}{\partial x} + \frac{\partial \mathbf{F}}{\partial y} + \frac{\partial \mathbf{G}}{\partial z} = \frac{\partial \mathbf{L}}{\partial x} + \frac{\partial \mathbf{M}}{\partial y} + \frac{\partial \mathbf{N}}{\partial z}\,, \tag{2.1.27}$$

where $\mathbf{U}$ is the array of the conservative variables; $\mathbf{E}, \mathbf{F}, \mathbf{G}$ are the inviscid and $\mathbf{L}, \mathbf{M}, \mathbf{N}$ are the viscous flux vectors associated with the Cartesian x-, y- and z-direction, respectively,

$$\mathbf{U} = \begin{pmatrix} \rho \\ \rho u \\ \rho v \\ \rho w \\ e \end{pmatrix},\ \mathbf{E} = \begin{pmatrix} \rho u \\ \rho u^2 + p \\ \rho v u \\ \rho w u \\ (e+p)u \end{pmatrix},\ \mathbf{F} = \begin{pmatrix} \rho v \\ \rho u v \\ \rho v^2 + p \\ \rho w v \\ (e+p)v \end{pmatrix},\ \mathbf{G} = \begin{pmatrix} \rho w \\ \rho u w \\ \rho v w \\ \rho w^2 + p \\ (e+p)w \end{pmatrix},$$

$$\mathbf{L} = \frac{1}{Re}\begin{pmatrix} 0 \\ \tau_{xx} \\ \tau_{xy} \\ \tau_{xz} \\ u\tau_{xx} + v\tau_{xy} + w\tau_{xz} - q_x \end{pmatrix},\ \mathbf{M} = \frac{1}{Re}\begin{pmatrix} 0 \\ \tau_{yx} \\ \tau_{yy} \\ \tau_{yz} \\ u\tau_{yx} + v\tau_{yy} + w\tau_{yz} - q_y \end{pmatrix},$$

$$\mathbf{N} = \frac{1}{Re}\begin{pmatrix} 0 \\ \tau_{zx} \\ \tau_{zy} \\ \tau_{zz} \\ u\tau_{zx} + v\tau_{zy} + w\tau_{zz} - q_z \end{pmatrix}.$$

In Equation (2.1.27), $q_{x,y,z}$ represents the net rates of heat transfer along x, y and z direction and τ_{ij} stands for the viscous stress in the j direction exerted on a plane normal to the i axis.

2.1.3 Generalised Curvilinear Coordinates

The Cartesian coordinate system, however, restrains the choice of cases that can be studied as a majority of the problems require arbitrary, body-fitted grids that permit the use of curved geometries. Because of this, the conversion of the Cartesian matrix form to a generalised curvilinear coordinate system given by $\xi = \xi(x, y, z, t)$, $\eta = \eta(x, y, z, t)$, $\zeta = \zeta(x, y, z, t)$ and $\tau = t$, e.g. see Drikakis' book [53], is the next step. In order to achieve this, Equation (2.1.27) is multiplied with the Jacobian determinant of the transformation from Cartesian

(x, y, z) to curvilinear (ξ, η, ζ) coordinates

$$J = \left|\frac{\partial(x, y, z)}{\partial(\xi, \eta, \zeta)}\right| = x_\xi \left(y_\eta z_\zeta - y_\zeta z_\eta\right) + y_\xi \left(z_\eta x_\zeta - z_\zeta x_\eta\right) + z_\xi \left(x_\eta y_\zeta - x_\zeta y_\eta\right) \tag{2.1.28}$$

and substituting the partial derivatives for non-moving grids

$$\begin{aligned}
\frac{\partial}{\partial x} &= \left(\frac{\partial}{\partial \xi}\right)\frac{\partial \xi}{\partial x} + \left(\frac{\partial}{\partial \eta}\right)\frac{\partial \eta}{\partial x} + \left(\frac{\partial}{\partial \zeta}\right)\frac{\partial \zeta}{\partial x}\,, \\
\frac{\partial}{\partial y} &= \left(\frac{\partial}{\partial \xi}\right)\frac{\partial \xi}{\partial y} + \left(\frac{\partial}{\partial \eta}\right)\frac{\partial \eta}{\partial y} + \left(\frac{\partial}{\partial \zeta}\right)\frac{\partial \zeta}{\partial y}\,, \\
\frac{\partial}{\partial z} &= \left(\frac{\partial}{\partial \xi}\right)\frac{\partial \xi}{\partial z} + \left(\frac{\partial}{\partial \eta}\right)\frac{\partial \eta}{\partial z} + \left(\frac{\partial}{\partial \zeta}\right)\frac{\partial \zeta}{\partial z}\,, \\
\frac{\partial}{\partial t} &= \frac{\partial}{\partial \tau}\,.
\end{aligned} \tag{2.1.29}$$

The compressible Navier-Stokes Equations in curvilinear coordinates are now represented by:

$$J\frac{\partial \mathbf{U}}{\partial \tau} + J\frac{\partial \mathbf{E}}{\partial \xi}\xi_x + J\frac{\partial \mathbf{E}}{\partial \eta}\eta_x + J\frac{\partial \mathbf{E}}{\partial \zeta}\zeta_x + \ldots = J\frac{\partial \mathbf{L}}{\partial \xi}\xi_x + J\frac{\partial \mathbf{L}}{\partial \eta}\eta_x + J\frac{\partial \mathbf{L}}{\partial \zeta}\zeta_x + \ldots\,, \tag{2.1.30}$$

where the subscripts indicate the partial derivatives with respect to spatial dimensions.

Using this relation (in 1D):

$$J\frac{\partial \mathbf{E}}{\partial \xi}\xi_x = \frac{\partial (J\mathbf{E}\xi_x)}{\partial \xi} - \mathbf{E}\frac{\partial}{\partial \xi}(J\xi_x) \tag{2.1.31}$$

will lead to further simplification of this expression and its equivalent for the other flux derivatives, resulting:

$$\frac{\partial \tilde{\mathbf{U}}}{\partial t} + \frac{\partial \tilde{\mathbf{E}}}{\partial \xi} + \frac{\partial \tilde{\mathbf{F}}}{\partial \eta} + \frac{\partial \tilde{\mathbf{G}}}{\partial \zeta} = \frac{\partial \tilde{\mathbf{L}}}{\partial \xi} + \frac{\partial \tilde{\mathbf{M}}}{\partial \eta} + \frac{\partial \tilde{\mathbf{N}}}{\partial \zeta}\,, \tag{2.1.32}$$

with

$$\begin{aligned}
\tilde{\mathbf{U}} &= J\mathbf{U} \\
\tilde{\mathbf{E}} &= J(\mathbf{E}\xi_x + \mathbf{F}\xi_y + \mathbf{G}\xi_z)\,, \\
\tilde{\mathbf{F}} &= J(\mathbf{E}\eta_x + \mathbf{F}\eta_y + \mathbf{G}\zeta_z)\,, \\
\tilde{\mathbf{G}} &= J(\mathbf{E}\zeta_x + \mathbf{F}\zeta_y + \mathbf{G}\zeta_z)\,, \\
\tilde{\mathbf{L}} &= J(\mathbf{L}\xi_x + \mathbf{M}\xi_y + \mathbf{N}\xi_z)\,, \\
\tilde{\mathbf{M}} &= J(\mathbf{L}\eta_x + \mathbf{M}\eta_y + \mathbf{N}\eta_z)\,, \\
\tilde{\mathbf{N}} &= J(\mathbf{L}\zeta_x + \mathbf{M}\zeta_y + \mathbf{N}\zeta_z)\,,
\end{aligned} \tag{2.1.33}$$

This system of equations is applied to the body-fitted grid, like a uniform and rectangular computational grid. As a result, the numerical treatment for solving the equations in Cartesian matrix form and generalised curvilinear matrix form is exactly the same. Again for simplicity reasons, the superscript ˜ is omitted for the remainder of this chapter.

2.2 Time Marching

The time-dependent Navier-Stokes Equations can be considered for both steady and unsteady flows. A time-marching algorithm that progressively determines the dependent variables in steps of time is used to find the solution. In case of steady flow, a constant state is approached asymptotically during the course of the simulation, while for unsteady cases, the inherently transient solution is predicted.

Explicit Runge Kutta time integration methods are chosen in this work for their ability to temporally resolve the rapidly fluctuating velocity components encountered in unsteady separated flows and for their simplicity. This approach constructs the solution as a linear combination of multiple stages where the number of stages is determined by the desired accuracy of the algorithm [53]. Before applying a Runge Kutta method to Equation (2.1.32), however, the time derivative has to be isolated

$$\frac{\partial \mathbf{U}}{\partial t} = -\frac{\partial \mathbf{E}}{\partial \xi} - \frac{\partial \mathbf{F}}{\partial \eta} - \frac{\partial \mathbf{G}}{\partial \zeta} + \frac{\partial \mathbf{L}}{\partial \xi} + \frac{\partial \mathbf{M}}{\partial \eta} + \frac{\partial \mathbf{N}}{\partial \zeta} = f(\mathbf{U}, t) \,, \tag{2.2.1}$$

2.2.1 Timestep Calculation

A common value needed to be obtained for any numerical temporal discretisation is that of Δt. For an explicit time stepping scheme, however, it can be shown that the solution will remain stable only up to a certain maximum value of Δt. The restriction results from the local speed of the fastest wave s, propagating through a cell in the entire computational domain. A simple way to visualise this is by examining Figure 2.2.

One can notice in Figure 2.2 that the wave propagates at a speed s_1 for a timestep duration Δt within the cell domain (considering x-direction). Thus, the solution obtained can be said to remain stable. However, if a faster wave speed exists, such as s_x, and within the same timestep length of Δt, it 'escapes' the cell domain, then the solution is said to be unstable. For a time-stepping scheme to be stable it has to meet the Courant-Friendrichs-Lewy condition (CFL) which states that if a wave is crossing a discrete grid, then the timestep must be less than the time for the wave to travel adjacent grid points. As a corollary, when the grid point separation is reduced, the upper limit for the timestep also decreases. As will be seen later this has the effect of reducing the timestep to a very small size when dealing with solid surfaces leading to considerable computational time requirements.

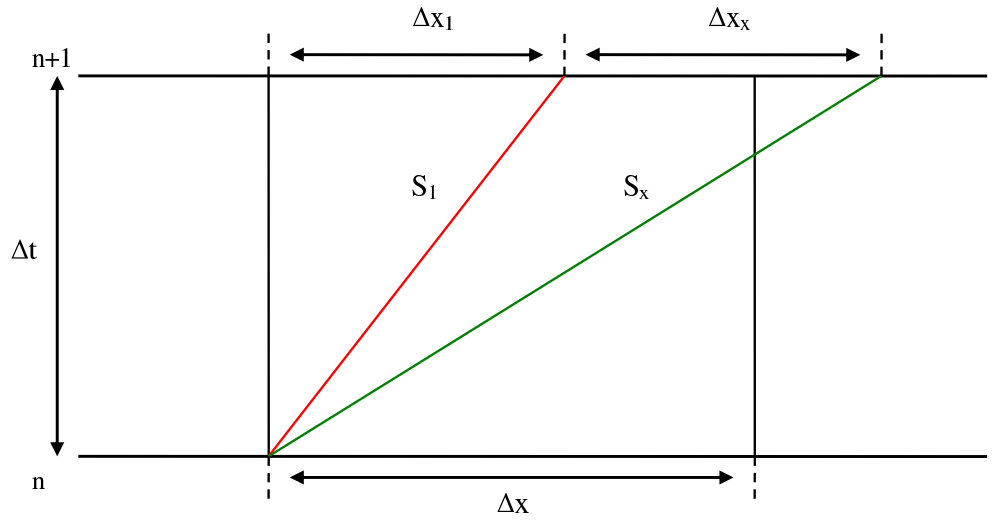

Figure 2.2: Fluxes and cell centre values

2.2.2 Global Timestep

For time-dependent flows, the same global timestep Δt has to be used for time marching in all computational cells, which, for a given Courant-Friedrichs-Lewy (CFL) number, is defined as

$$\Delta t = min\left(J\frac{CFL}{max(|\lambda_0^\xi|,|\lambda_+^\xi|,|\lambda_-^\xi|,|\lambda_0^\eta|,|\lambda_+^\eta|,|\lambda_-^\eta|,|\lambda_0^\zeta|,|\lambda_+^\zeta|,|\lambda_-^\zeta|)}\right), \tag{2.2.2}$$

with J denoting the Jacobian determinant and λ are the eigenvalues associated with the advective fluxes **E**, **F**, **G**, respectively.

For the forward Euler method from Equation (2.2.3), the theoretical value of $CFL \leq 1$ leads to a stable integration in time. This means that the length of the timestep is equal or less than the time it takes for the fastest acoustic wave to travel from one grid point to the next. Although setting CFL to less than 1 is necessary, it does not guarantee the stability of the algorithm, as instabilities in the sense of permitting large errors may still appear. To resolve this issue, the CFL is lowered until a stable solution is obtained. Note that it is introduced due to the non-linear nature of the governing equations in which case it is possible for a wave to vary in a non-linear manner and therefore reach the adjacent grid point within the time calculated by the assumed linear wave.

2.2.3 Third-Order Runge Kutta

The standard third-order accurate Runge Kutta method consists of the following stages:

$$\begin{aligned}\frac{\mathbf{U}^1-\mathbf{U}^n}{\Delta t} &= \frac{1}{3}f(\mathbf{U}^n,t^n)\,,\\ \frac{\mathbf{U}^2-\mathbf{U}^n}{\Delta t} &= \frac{2}{3}f(\mathbf{U}^1,t^{n+1/3})\,,\\ \frac{\mathbf{U}^{n+1}-\mathbf{U}^n}{\Delta t} &= \frac{1}{4}\left[f(\mathbf{U}^n,t^n)+3f(\mathbf{U}^2,t^{n+2/3})\right]\,.\end{aligned} \tag{2.2.3}$$

Similar to the two-stage algorithms, a third-order accurate TVD Runge Kutta can be formulated

$$\begin{aligned}\frac{\mathbf{U}^1-\mathbf{U}^n}{\Delta t} &= f(\mathbf{U}^n,t^n)\,,\\ \frac{\mathbf{U}^2-\mathbf{U}^n}{\Delta t} &= \frac{1}{4}\left[f(\mathbf{U}^n,t^n)+f(\mathbf{U}^1,t^{n+1/3})\right]\,,\\ \frac{\mathbf{U}^{n+1}-\mathbf{U}^n}{\Delta t} &= \frac{1}{6}\left[f(\mathbf{U}^n,t^n)+4f(\mathbf{U}^2,t^{n+2/3})+f(\mathbf{U}^1,t^{n+1/3})\right]\,.\end{aligned} \tag{2.2.4}$$

Additionally, time integration schemes can be designed with extended stability properties in mind, leading to the alternative three-stage, third-order accurate algorithm given by:

$$\begin{aligned}\frac{\mathbf{U}^1-\mathbf{U}^n}{\Delta t} &= \frac{1}{2}f(\mathbf{U}^n,t^n)\,,\\ \frac{\mathbf{U}^2-\mathbf{U}^n}{\Delta t} &= \frac{1}{2}f(\mathbf{U}^1,t^{n+1/3})\,,\\ \frac{\mathbf{U}^{n+1}-\frac{2}{3}\mathbf{U}^2-\frac{1}{3}\mathbf{U}^n}{\Delta t} &= \frac{1}{3}\left[f(\mathbf{U}^2,t^{n+2/3})+f(\mathbf{U}^1,t^{n+1/3})\right]\,.\end{aligned} \tag{2.2.5}$$

Higher order methods can be constructed as above, but the level of improvement in the results is insignificant compared to the increased computational cost observed in most cases. For this reason, higher order methods will not be discussed here.

2.3 Discretisation

Discretisation is the process of transferring continuous models and equations into discrete counterparts. This process is usually carried out as a first step towards making them suitable for numerical evaluation and implementation on digital computers. Discretisation is also concerned with the transformation of continuous differential equations into discrete difference equations, suitable for numerical computing.

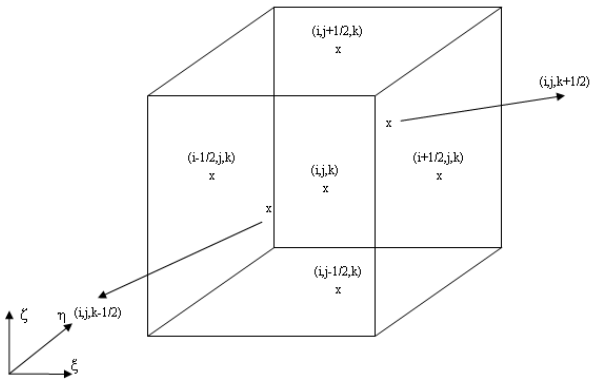

Figure 2.3: 3D notation for a finite volume cell

The inter-cell flux values across the faces defined by the subscripts $(i \pm 1/2, j, k)$, $(i, j \pm 1/2, k)$ and $(i, j, k \pm 1/2)$ are used to discretise the spatial derivatives at the centre of the control volume (i, j, k) as shown in Figure 2.3.

Based on the above statement, Equation (2.2.1) in semi-discretised form can now be written:

$$\begin{aligned}\frac{\partial \mathbf{U}}{\partial t} = &- \frac{\mathbf{E}_{i+1/2,j,k} - \mathbf{E}_{i-1/2,j,k}}{\Delta\xi} - \frac{\mathbf{F}_{i,j+1/2,k} - \mathbf{F}_{i,j-1/2,k}}{\Delta\eta} - \frac{\mathbf{G}_{i,j,k+1/2} - \mathbf{G}_{i,j,k-1/2}}{\Delta\zeta} \\ &+ \frac{\mathbf{L}_{i+1/2,j,k} - \mathbf{L}_{i-1/2,j,k}}{\Delta\xi} + \frac{\mathbf{M}_{i,j+1/2,k} - \mathbf{M}_{i,j-1/2,k}}{\Delta\eta} + \frac{\mathbf{N}_{i,j,k+1/2} - \mathbf{N}_{i,j,k-1/2}}{\Delta\zeta} ,\end{aligned} \tag{2.3.1}$$

with the terms on the right-hand side being solved independently and the complete system integrated in time after all the discretised fluxes are summed.

A central difference scheme is used to calculate the linear viscous fluxes **L**, **M** and **N**, while the non-linear advective fluxes **E**, **F** and **G** are evaluated using a high-resolution Godunov-type method.

2.4 Low Mach Number Treatment

Kolmogorov states [80] that the leading order kinetic energy dissipation rate is proportional to $u^3/\Delta x$ for decaying turbulence. In the ILES approach as presented in [81] the dissipation rate substantially amends the high wave-number performance. To control any excessive dissipation for decreasing local Mach numbers, the Low Mach Mach Number Treatment (LMNT) has been proposed [81, 82]. This method has been designed in order to assure uniform dissipation of the kinetic energy within the limit of Mach number $M = 0$.

The working idea of this treatment stands as a correction operation in the reconstruction procedure. The LMNT is employed on discontinuity at the cell interface between the left and right values. The addition of a function z in the velocity discontinuity assures reasonable numerical dissipation rate and does not exceed that of the original scheme. Equation 2.4.1 illustrates the modification with function z

$$\overrightarrow{u}^{R}_{i+1/2,j,k} = \frac{\overrightarrow{u}^{L} + \overrightarrow{u}^{R}}{2} + z\frac{\overrightarrow{u}^{R} - \overrightarrow{u}^{L}}{2} \quad , \quad \overrightarrow{u}^{L}_{i+1/2,j,k} = \frac{\overrightarrow{u}^{L} + \overrightarrow{u}^{R}}{2} + z\frac{\overrightarrow{u}^{L} - \overrightarrow{u}^{R}}{2} \tag{2.4.1}$$

where z is defined as

$$z = \min\left(M_{total}, 1\right) \quad , \quad M_{total} = \max\left(M_L, M_R\right) \tag{2.4.2}$$

Where M_L and M_R are the local Mach number subscript L and R denote the left and right of the cell face. This augmentation leads to a progressive blending in of central differencing for the velocity components, where central cifferencing is recovered for $M = 0$. The correction extends the applicability of the Godunov-type methods to a least $M \approx 10^{-4}$ ([81, 82]). At the same time it can be considered as a 'realistic' physical law addition to the standard Godunov method because of the new treatment of the velocity jumps; otherwise Godunov's method would set up artificially large jumps not really present in a low Mach number flowfield.

As probably noticed, the reconstructed left and right density and pressure are not modified, but since the velocity flux has altered, the total energy flux will need to be corrected to accommodate for the new kinetic energy (KE) flux. It is important to point out that the reconstruction is modified based on the local properties of the flowfield, hence the same governing equations are solved throughout the domain and thus it's additional computational 'effort' is considerably small.

However, Low Mach Number Treatment was designed for freestream flows. It was designed to counteract uniformly low Mach freestream flows which would otherwise cause excess dissipation in Godunov type solvers. ILES is, as stated before, sensitive to numerical dissipation so low (local) Mach numbers near the walls can have a significant effect in the simulations. Here is where the effect of a method like LMNT can be tested for wall bounded turbulent flows to deal with the local low Mach numbers. LMNT could prove an important tool in producing improved results in ILES simulation for this kind of flows and is an important part of this study.

2.5 Riemann Solver

In order to introduce the concept of the Riemann solver, it is helpful to consider in the first instance the physical problem of a closed tube initially divided into two sections separated by a diaphragm, one with a high pressure and the other with a low one as displayed by Figure 2.4(a) with the fluid resting. An instant removal of the diaphragm leads to a shock wave, caused by the high pressure gradient, moving to the right, an isentropic expansion wave propagating to the left and a contact surface separating the two different fluids emerging due to the different process they underwent, Figure 2.4(b). The main difference in the two resulting fluids emerges from the fact that the shock wave will cause a change in enthalpy whereas the isentropic expansion will not thus resulting in a contact surface where the two fluids meet. The solution of the flowfield in the shock tube as sketched in Figure 2.4 is referred to as the Riemann problem, named after the German mathematician G.F. Bernhard Riemann who first attempted it's solution in 1858, and is a direct analytic solution of the unsteady, one-dimensional Euler equations. First, all the properties of regions 1 and 4 are known before the diaphragm is removed and remain the same in the regions not reached by the shock or the expansion wave. An "exact" solution to the remaining problem can be found applying conservation laws across the waves in the problem [83]. However the exact method leads to a transcendental equation for pressure which has to be solved iteratively.

A piecewise-average representation of data in a finite volume solver presents a similar discontinuity at each cell face. The main difference being that in the context of a finite volume solver, not only pressure, density and temperature are varying in the initial condition but also the velocity can vary across the discontinuity. This modified Riemann problem can be solved in the same manner as the shock tube problem resulting in the values at the cell face which are required in order to determine intercell fluxes for the finite volume scheme. S.K. Godunov [84] was the first to suggest such a method leading to an "exact" Godunov solver.

Because the exact Riemann solver is too costly, some approximations are necessary resulting to the approximate Riemann solvers. In the approximate Riemann solvers, the intercell fluxes are directly approximated. An approximated expression of the fluxes is produced by applying the integral form of the conservation laws.

There are many different approximated solvers with some examples being:

- The Roe approximate Riemann solver, devised by Roe [85].
- The HLLC, introduced by Toro [86].
- Rotated-hybrid Riemann solvers that were introduced by Nishikawa and Kitamura [87].

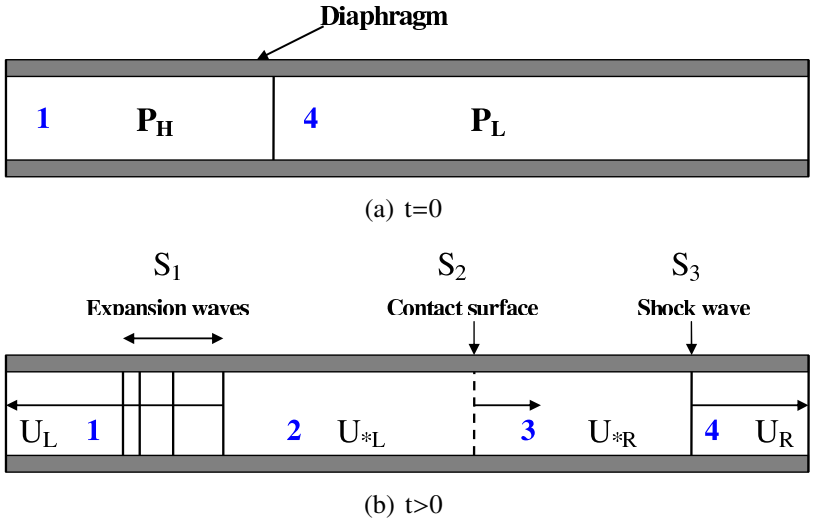

Figure 2.4: Shock Tube

In this thesis, the advective fluxes were solved using the HLLC solver as presented by Toro [86, 88]. The Harten, Lax and van Leer solver (HLL) is a robust approximate Godunov method. Toro, implemented a version where missing contact and shear waves are restored, resulting to a modified version of the HLL scheme known as HLLC with C representing the Contact.

2.5.1 HLLC

The approximate Riemann solver assumes a wave configuration that separates the constant states of the solution. The difference between the HLL and HLLC solvers is the number of waves. In the HLL the three constant states U_L, U_R and the *Star Region* (intermediate region) are separated by two waves S_L and S_R. The HLLC solver, on the other hand, contains three waves, thus creating four regions. The missing contact wave mentioned above is now represented by the additional wave. The waves, the regions, and the split of the *Star Region* in two parts are shown in Figure 2.5 [88].

The newly obtained wave speeds are used to calculate the fluxes by combining them with the constant states of the variables.

Based on Toro [88] the fluxes are calculated though the following procedure:

The left and right states of the primitive variables are calculated from the reconstruction step using High Resolution schemes, described in the previous subsection. The pressure in the star region is estimated by using the left and right states of the primitive variables:

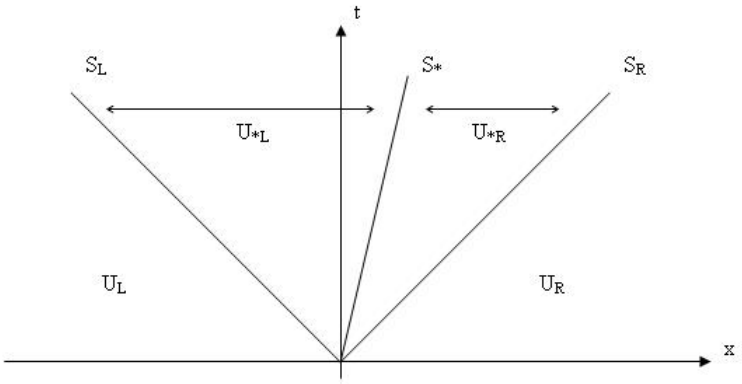

Figure 2.5: HLLC Riemann Solver

$$p_* = \frac{1}{2}(p_L + p_R) - \frac{1}{2}(u_R - u_L)(\bar{\rho}\bar{a}) \ . \tag{2.5.1}$$

where $\bar{\rho}$ and $\bar{a}$ are the averaged density and speed of sound respectively:

$$\bar{\rho} = \frac{1}{2}(\rho_L + \rho_R) \tag{2.5.2}$$

$$\bar{a} = \frac{1}{2}(a_L + a_R) \tag{2.5.3}$$

The S_L and S_R speeds are then calculated using the following equations:

$$S_L = u_L - a_L q_L \ , \quad S_R = u_R - a_R q_R \ , \tag{2.5.4}$$

with

$$q_K = \begin{cases} 1 & \text{if} \quad p_* \le p_K \\ \left[1 + \frac{\gamma+1}{2\gamma}(p_*/p_K - 1)\right]^{\frac{1}{2}} & \text{if} \quad p_* > p_K \end{cases} \ . \tag{2.5.5}$$

where K indicates the left or right states

The star wave speed is calculated as follows:

$$S_* = \frac{p_R - p_L + \rho_L u_L(S_L - u_L) - \rho_R u_R(S_R - u_R)}{\rho_L(S_L - u_L) - \rho_R(S_R - u_R)} \ . \tag{2.5.6}$$

and the U_{*L} and U_{*R} states are given by:

$$\mathbf{U}_{*K} = \rho_K \left(\frac{S_K - u_K}{S_K - S_*} \right) \begin{pmatrix} 1 \\ S_* \\ v_K \\ w_K \\ \frac{E_K}{\rho_K} + (S_* - u_K) \left[S_* + \frac{p_K}{\rho_K (S_K - u_K)} \right] \end{pmatrix}. \tag{2.5.7}$$

Finally, the flux is calculated by applying the Rankine-Hugoniot conditions:

$$\mathbf{F}_{i+1/2}^{HLLC} = \begin{cases} \mathbf{F}_L & if \quad 0 \le S_L \\ \mathbf{F}_L + S_L(\mathbf{U}_{*L} - \mathbf{U}_L) & if \quad S_L \le 0 \le S_* \\ \mathbf{F}_R + S_R(\mathbf{U}_{*R} - \mathbf{U}_R) & if \quad S_* \le 0 \le S_R \\ \mathbf{F}_R & if \quad 0 \ge S_R \end{cases}. \tag{2.5.8}$$

2.6 High-Resolution Methods

Use of high-resolution high-order methods in ILES is innovative and challenging and has been the focus of some researchers the past few years. There is a wide range of cases (mostly turbulent flows) that are being studied using these methods. An important issue with the use of these methods in ILES is the universality of the approach for many different flows. Given this uncertainty the challenge for the use of these methods is significant. Some of the cases that have been studied so far using these methods include open cavity flows [63, 89], highly swept wings [90] and low resolution decaying turbulence [91]. More cases can be seen in the introduction of this study. Upwind methods are typically overly dissipative for simulations of homogenous decaying turbulence when using second and third order methods [92]. High order methods improve this situation but do not cure the problem completely [91] so more detailed research of different cases would be beneficial. Further evaluation of the methods in turbulent flows will provide usefull information for their future use, accuracy and affordability.

The search for a new family of numerical schemes that combine the need for a highly accurate simulation and the preservation of monotonicity, that is a basic property of the exact solution, lead to the use of modern high-resolution methods. Monotone, first-order methods, may avoid spurious oscillations, but they are inaccurate for practical simulations.

High-resolution schemes use a type of nonlinear methods to manage oscillations in the solution, compared to to linear methods that use the same differencing stencil throughout. High-resolution of the numerical solver is achieved by extrapolating the variables as linear, quadratic or higher-order functions in a cell, whereas first-order algorithms follow a

piecewise constant approach. This is the general basis of the non-linear mechanism that distinguishes modern methods from classical linear schemes. Additionally, high-resolution methods are able to adapt to the behaviour of the local solution instead of treating each part of the solution identically, resulting in a sensitivity to the state of the flow.

In this research, two forms of reconstruction methods are used and presented: different variants of the *Monotonic Upwind Scheme for Scalar Conservation Laws* (MUSCL) as originally introduced by Leer [93], and a *Weighted Essentially Non-Oscillatory* (WENO) scheme following the ideas of Liu [94].

2.6.1 MUSCL Schemes

According to Toro [88], the left and right states of the conservative variables $\mathbf{U}$ at the cell interface $(i + 1/2)$ are computed for the MUSCL schemes as presented here:

$$\begin{aligned}\mathbf{U}_{L,i+1/2} =&\mathbf{U}_i \quad + \frac{1}{4}\left[(1-k)\,\phi\,(r_L)\,(\mathbf{U}_i - \mathbf{U}_{i-1}) + (1+k)\,\phi\left(\frac{1}{r_L}\right)(\mathbf{U}_{i+1} - \mathbf{U}_i)\right] ,\\ \mathbf{U}_{R,i+1/2} =&\mathbf{U}_{i+1} - \frac{1}{4}\left[(1-k)\,\phi\,(r_R)\,(\mathbf{U}_{i+2} - \mathbf{U}_{i+1}) + (1+k)\,\phi\left(\frac{1}{r_R}\right)(\mathbf{U}_{i+1} - \mathbf{U}_i)\right] ,\end{aligned} \tag{2.6.1}$$

where k is a free parameter in the interval $[-1, 1]$ and ϕ is a limiter function based on the slopes of the conserved variables within, for the second- and third-order accurate schemes, the four-point stencil given by the cell averaged values at positions $(i - 1)$, (i), $(i + 1)$ and $(i + 2)$. For $k = -1$ or $k = 0$ the MUSCL extrapolation in Equations (2.6.1) is essentially a full upwind scheme or a central difference scheme, respectively, and third-order of accuracy can be obtained for $k = 1/3$ if the limiter is not entirely symmetric [88].

Second-order limiters: All second- and third-order accurate limiter functions use the following definitions of the left and the right ratio of the slopes:

$$\begin{aligned} r_L =& \frac{\mathbf{U}_{i+1} - \mathbf{U}_i}{\mathbf{U}_i - \mathbf{U}_{i-1}} ,\\ r_R =& \frac{\mathbf{U}_{i+1} - \mathbf{U}_i}{\mathbf{U}_{i+2} - \mathbf{U}_{i+1}} .\end{aligned} \tag{2.6.2}$$

$$\phi_{MC} = \begin{cases} 0 & \text{if } r \le 0 \\ min(\frac{1+r}{2}, 2, 2r) & \text{if } r > 0 \end{cases} , \tag{2.6.3}$$

with *MC* representing the Monotonized Central limiter.

Fifth-order limiter: A fifth-order accurate MUSCL scheme was presented by [95] applying a six-point stencil, as opposed to the classical four-point stencil employed previously. The slope ratios are defined as:

$$\begin{aligned} r_{L,i} &= \frac{\mathbf{U}_{i+1} - \mathbf{U}_i}{\mathbf{U}_i - \mathbf{U}_{i-1}} , \\ r_{R,i} &= \frac{\mathbf{U}_i - \mathbf{U}_{i-1}}{\mathbf{U}_{i+1} - \mathbf{U}_i} , \end{aligned} \tag{2.6.4}$$

and ϕ is calculated by

$$\begin{aligned} \phi^*_{L,M5} &= \frac{-2/r_{L,i-1} + 11 + 24 r_{L,i} - 3 r_{L,i} r_{L,i+1}}{30} , \\ \phi^*_{R,M5} &= \frac{-2/r_{R,i+2} + 11 + 24 r_{R,i+1} - 3 r_{R,i+1} r_{R,i}}{30} . \end{aligned} \tag{2.6.5}$$

2.6.2 WENO Schemes

Essentially Non-Oscillatory (ENO) concept originally proposed by Harten [96] has been developed as a higher-order interpolation method. ENO aims at constructing high-order schemes in smooth regions and through the use of adaptive stencils achieve high accuracy up to discontinuities while at the same time providing high order solutions that are free of spurious oscillations [53]. The ENO schemes select an interpolating stencil in which the solution is supposed to be the smoothest one. If a cell is near a discontinuity, the smoothest possible solution is assigned to this cell avoiding spurious oscillations [53]. So to sum it up, high-degree polynomials are prone to oscillations even if the underlying data is smooth. In order to control these oscillations, without using limiter functions like the MUSCL schemes, ENO chooses the smoothest of many possible stencils to avoid disastrous overshoots or undershoots, and as a result, does not formally satisfy the non-linear stability criteria.

WENO is an extension of the ENO concept. WENO methods are primarily based on the work of Balsara, Jiang and Liu [94, 97, 98]. Instead of choosing a single stencil, WENO combines all possible stencils in order to produce a convexly weighted average based on their smoothness. The sensitivity to small changes in the samples and the effects of the truncation errors are significantly reduced with the use of the averaging. WENO schemes ideally reach an order of accuracy calculated by $2s - 1$, with s being the number of sample points, whereas ENO methods achieve lower orders of accuracy because they discard most of the points.

The WENO method employed in this thesis uses a stencil of five cells to either side of the interface, resulting in a ninth order accurate scheme in one dimension. A third-order WENO reconstruction derived from a linear interpolation with $s = 2$ is presented here in order to illustrate the basic concept of the method. For the reconstruction within a cell i,

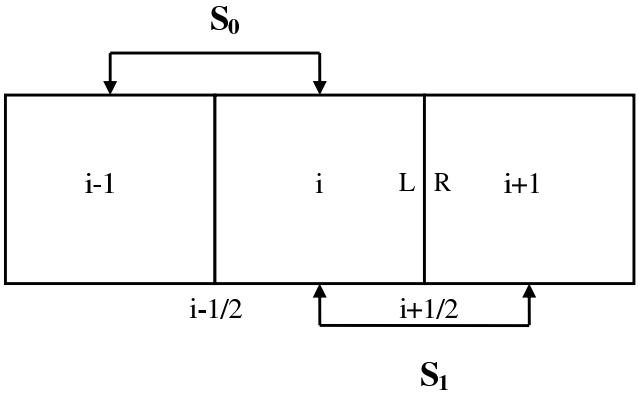

Figure 2.6: Third-order WENO reconstruction stencils

two stencils $S_{0,1}$ comprising the cell-averaged values of two samples each are considered (Figure 2.6)

$$\begin{aligned} S_0 &= (x_{i-1}, x_i) \ , \\ S_1 &= (x_i, x_{i+1}) \ . \end{aligned} \tag{2.6.6}$$

A standard linear interpolation using the stencils 0 and 1 leads to the following polynomials

$$\begin{aligned} \mathbf{p}_0(x) &= \mathbf{U}_i + \frac{\mathbf{U}_i - \mathbf{U}_{i-1}}{\Delta x} (x - x_i) \ , \\ \mathbf{p}_1(x) &= \mathbf{U}_i + \frac{\mathbf{U}_{i+1} - \mathbf{U}_i}{\Delta x} (x - x_i) \ , \end{aligned} \tag{2.6.7}$$

where the right interface value at $i - 1/2$ and the left interface value at $i + 1/2$ are obtained for x equal to $x_{i-1/2}$ and $x_{i+1/2}$, respectively. The weighted average **P** calculation gives the reconstructed variables at the cell faces $\mathbf{U}_{R,i-1/2}$ and $\mathbf{U}_{L,i+1/2}$. The convex combination is defined by:

$$\mathbf{P}(x) = \frac{\mathbf{a}_0}{\mathbf{a}_0 + \mathbf{a}_1} \mathbf{p}_0(x) + \frac{\mathbf{a}_1}{\mathbf{a}_0 + \mathbf{a}_1} \mathbf{p}_1(x) \ , \tag{2.6.8}$$

with

$$\begin{aligned} \mathbf{a}_0 &= \frac{C_0}{(\epsilon + \mathbf{IS}_0)^2} \ , \\ \mathbf{a}_1 &= \frac{C_1}{(\epsilon + \mathbf{IS}_1)^2} \ . \end{aligned} \tag{2.6.9}$$

where ϵ is a small positive number introduced in order to avoid a division by zero in a perfectly smooth flow and $C_{0,1}$ are the optimal weights. The smoothness indicators are

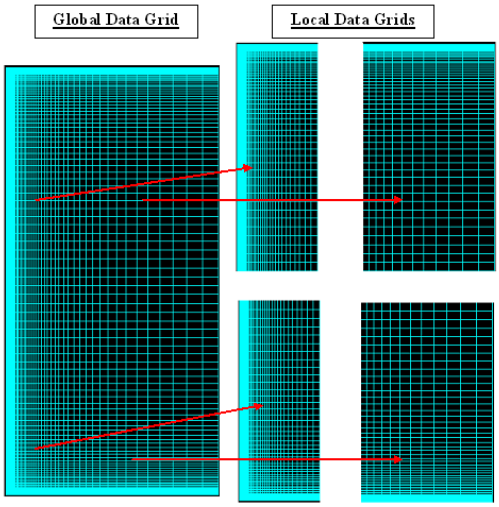

Figure 2.7: Decomposition of a 2D global data domain over four processors

calculated by:

$$\begin{aligned} \mathbf{IS}_0 &= (\mathbf{U}_i - \mathbf{U}_{i-1})^2 \ , \\ \mathbf{IS}_1 &= (\mathbf{U}_{i+1} - \mathbf{U}_i)^2 \ . \end{aligned} \tag{2.6.10}$$

Higher-order method derivation follows the same idea but due to the equation complexity, it can not be presented here. More details however can be found in [53, 97, 98].

2.7 Domain Decomposition

The study of turbulent three-dimensional flows using ILES is computationally expensive because of the large amount of data required. In order to reduce the cost in time, the cases must be solved using a set number of processors. This inevitably leads to an increase of the cost in computational resources. The computational domain is divided into several smaller ones that are assigned to a different processor. Each processor then solves the governing equations in parallel with the other ones, splitting the problem into several smaller (local) ones. This way the simulation time is significantly reduced, see Figure 2.7 .

The degree of domain decomposition is dependent on the number of processes available. Using parallel computing allows the calculation of problems that otherwise are memory bound. A pre-processing programme is used to split the domain into its smaller parts. For the simulation to work as if it was running in one processor, an exchange of data between processors is required. In every iteration the neighbouring processors exchange data according to the MPI-1 standard [99, 100]. With the use of MPI, the computational

time is significantly reduced and the code remains in a portable form.

2.8 Forcing Term

The final issue that needs resolving is that of the periodic boundary conditions for the straight duct case. Since the mass flux of the flow needs to be preserved, a forcing term is introduced in the streamwise pressure gradient at the NSE and due to that it influences the entire flow. Originally a compressible flow technique [101], it utilises an extra streamwise pressure gradient achieving the target mass flux through a pressure drop. After the introduction of the forcing term the momentum and energy equations are written as:

$$\frac{\partial}{\partial t}(\rho u_i) + \frac{\partial}{\partial x_i}(\rho u_i u_j) + \frac{\partial p}{\partial x_i} + f_i \delta_{i1} = \frac{\partial \sigma_{ij}}{\partial x_j} \tag{2.8.1}$$

$$\frac{\partial E}{\partial t} + \frac{\partial}{\partial x_i}(E + p)u_j + f_i u_1 = \frac{\partial}{\partial x_j}(\sigma_{ij} u_i) - \frac{\partial}{\partial x_j} q_j \tag{2.8.2}$$

where t and x_i the time and space variables, f_i the forcing term, σ_{ij} the viscous stress tensor, δ_{ij} the Kronecker symbol where $\delta_{ij} = 1$ if $i = j$ and $\delta_{ij} = 0$ otherwise and q_j the heat flux. The process of the calculation of the forcing term is presented below.

After the momentum equation is averaged over xy planes and integrated in the wall normal direction it produces:

$$\frac{\partial}{\partial t} Q_m = \frac{1}{Re} L_y \left[\langle \mu \rangle_{xy} \frac{\partial \langle u_1 \rangle}{\partial z} \right]_{z=0}^{2} - L_y L_z f_1 \tag{2.8.3}$$

with $\langle \rangle_{xy}$ being the average over the xy plane, L_z the width of the duct, L_y the duct span and Q_m the mean flux of the flow at yz plane.

Providing that:

$$\langle \mu \rangle_{xy} \frac{\partial \langle u_1 \rangle}{\partial z} \|_{z=2} = - \langle \mu \rangle_{xy} \frac{\partial \langle u_1 \rangle}{\partial z} \|_{z=0} \tag{2.8.4}$$

we get:

$$\frac{\partial}{\partial t}Q_m = -L_y L_z f_1 - 2\frac{1}{Re}L_y \langle\mu\rangle_{xy} \frac{\partial \langle u_1 \rangle}{\partial z}\|_{z=0} \tag{2.8.5}$$

It can be concluded from the above equation that the use of a constant forcing term will lead to the decrease of the mass flux due to the higher shear stress of the transitional flow.

As a result, in order to have a constant mass flux for a fully developed turbulent flow, the forcing term must have a time depended behaviour.

The previous method has been developed further in [102] in order to be time depended:

$$f_1^{n+1} = f_1^n + \frac{\Delta t}{L_y L_z}\left[a(Q^{n+1} - Q_0) + \beta(Q^n - Q_o)\right] \tag{2.8.6}$$

with Q_0, Q^n and Q^{n+1} being the conserved mass flux, the mass flux at time step n and $n+1$ computed from

$$Q^{n+1} = Q^n - \Delta t g^n \tag{2.8.7}$$

$$g^n = L_y L_z f^n + \frac{4L_y}{Re}\langle\mu^n\rangle_{xy} \frac{\partial \left\langle u_1^n \right\rangle}{\partial z}\|_{z=0} \tag{2.8.8}$$

In the above formula we multiply by 4 taking into account that there are four walls compared to the two walls in a channel flow. This also means that this formula can be used for a square sectioned duct since span and gap lengths are equal. In an unsteady flow the forcing term will be fluctuating near a mean value while in a steady case it will be constant.

CHAPTER 3

Straight Duct Flow

Channel flows are a traditional research topic for studying turbulence. Many cases can be found in the literature regarding this area. The case of the duct flow though (especially at high Reynolds numbers) can present even more interesting results considering its basic difference to the channel, where instead of two parallel plates we have four. The flow is confined in this space and surrounded by four walls. The basic difference to the channel flow is the existence of the four corners whose effect can present an interesting study. The flow is significantly affected by the existence of four walls because of the surrounding turbulent boundary layer. All the above make this a suitable case for studying the ability of a CFD algorithm to model turbulence in the presence of solid surfaces. Here, the flow inside a straight duct with periodic boundary conditions will be studied. Different grids and schemes will be employed in the investigation of the flow.

Besides the obvious and aforementioned reasons for studying the flow inside a straight duct, there was one more reason for this study. The resulting developed turbulent flow will be used to supply the L-bend case study, with a developed turbulent flow instead of simply using a boundary profile that would be complicated to develop for a square sectioned case. This way less time and more accuracy can be achieved in those simulations.

3.1 Problem Description

The geometry under investigation is a square sectioned duct with four walls with a 1 H distance between them. The size of the duct is 6.28H x 1H x 1H in length (L), spanwise width (W) and height (H) in x, y, z directions respectively. In this case since it is a square sectioned duct (W) equals (H). The length of 6.28H or 2πH was based on a similar case for a plane channel [1] where this was proved to be the length needed for the flow to develop. A periodic boundary condition is used in the streamwise direction and a no-slip (wall) condition along the surrounding walls. All the above are shown in Figures 3.1 and 3.2.

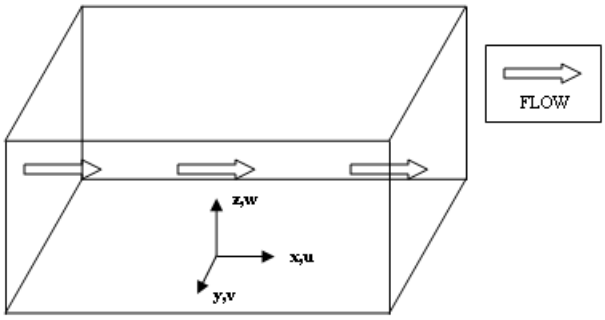

Figure 3.1: Duct coordinate system

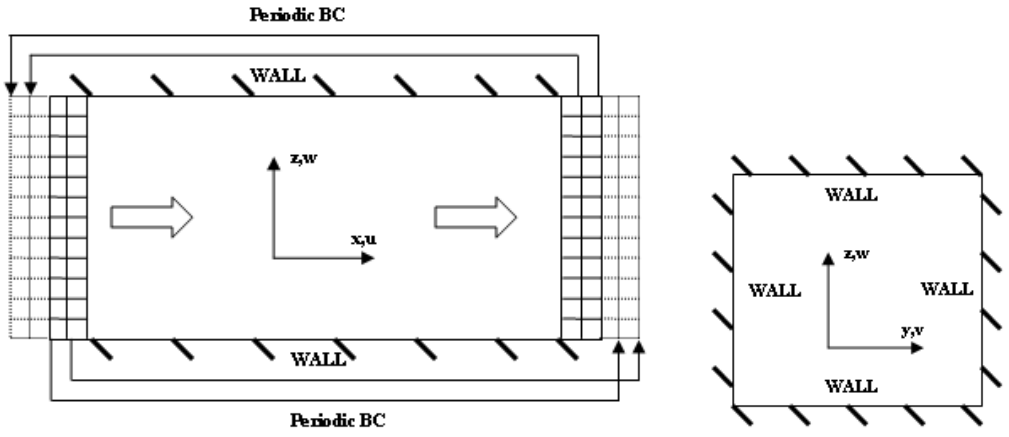

(a) X-Z plane BCs (b) Y-Z plane BCs

Figure 3.2: Boundary conditions

Air at standard atmospheric ground level conditions is used as the modelled flow. The Reynolds number is equal to 40,000 based on the bulk flow velocity. There are no experimental data for a straight duct at this Reynolds number so the results obtained will be compared to an experiment conducted by Laufer [23] on a channel flow. The results will be compared to the channel flow in order to locate the main differences between the two cases and see how closely the profile is captured by the different grids and schemes. This will not be a validation procedure since the cases are not identical and do not allow such assumptions but will provide a comparison base for the differences between duct and channel flows as well as useful information for the L-bend case that follows. The Reynolds number of 40,000 was used since the flow developed inside the duct will be used as the incoming flow in the case that follows for which that case there is an experiment providing a large amount of data at this Reynolds number.

3.2 Computations

In this section the grid used along with the initial conditions and the methods for calculating the flow properties are presented.

3.2.1 Grid

For the purposes of the simulations, three grids were generated using Gridgen V15.11. These three grids were based on the same geometry but had a different number of cells (coarse and fine grids). Most of the cells were located in the near wall region since that is the more important area of study in this case. Besides the existence of smaller turbulent scales in this region there is also a boundary layer because of the solid wall and viscous flow combination. This way an additional parameter that needs to be captured is introduced.

The number of points in the z and y direction was the same and equalled to 49 for the course, 73 for the medium and 97 for the fine grid. In the x direction 66, 96 and 129 points were used respectively resulting to the three grids of size 49x49x66, 73x73x96 and 97x97x129. The grid sizes and the distance of the first point from the wall are shown in Table 3.1. Finally in Figures 3.3, 3.4 and 3.5 the grids are shown in order to make the difference in clustering visually clear. The grid generation was based on the work of Kokkinakis [1] for a plain channel adjusted in this case, based on the Reynolds number to ensure that the simulation is wall resolved.

As mentioned before, the near wall region is very important in this (and all similar) case. The near wall clustering is essential for the correct capture of the boundary layer.

Grid	Grid Size	Δz	y^+
Coarse	49x49x66	0.001	2.4
Medium	73x73x96	0.00075	1.8
Fine	97x97x129	0.0005	1.2

Table 3.1: Grid and first cell sizes

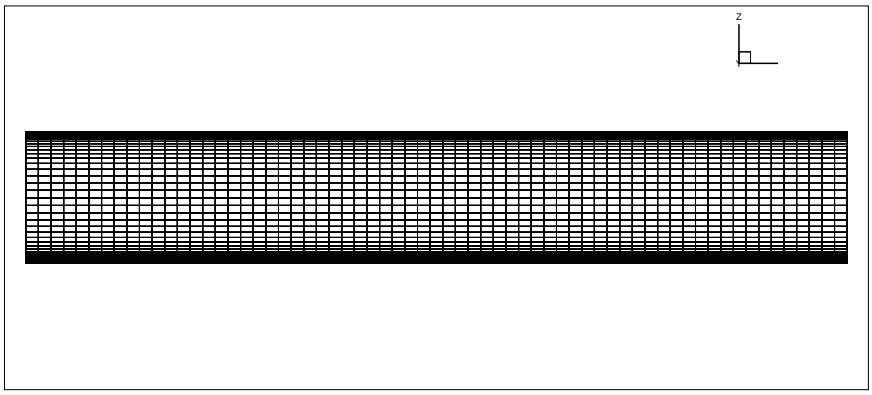

(a) coarse grid for straight duct

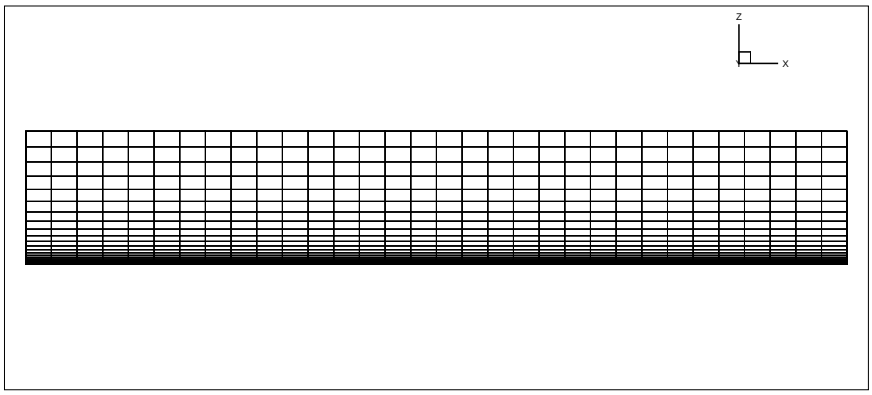

(b) coarse grid closer to wall

Figure 3.3: Coarse Grid

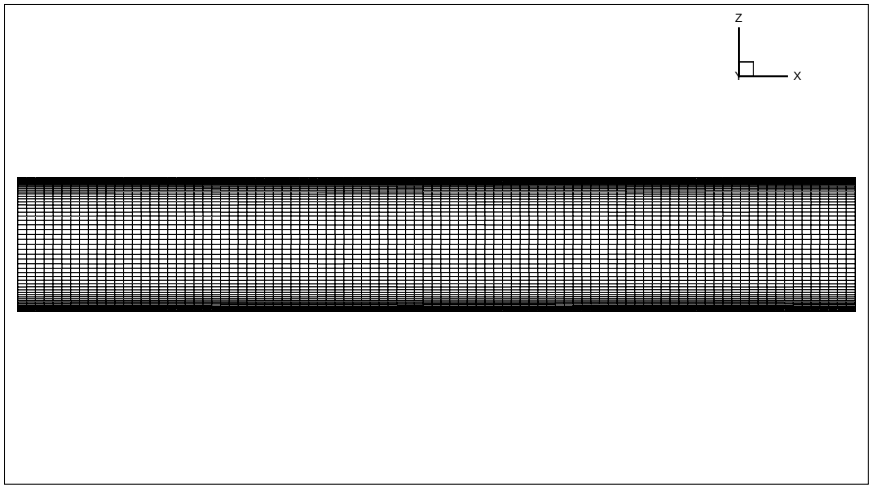

(a) medium grid for straight duct

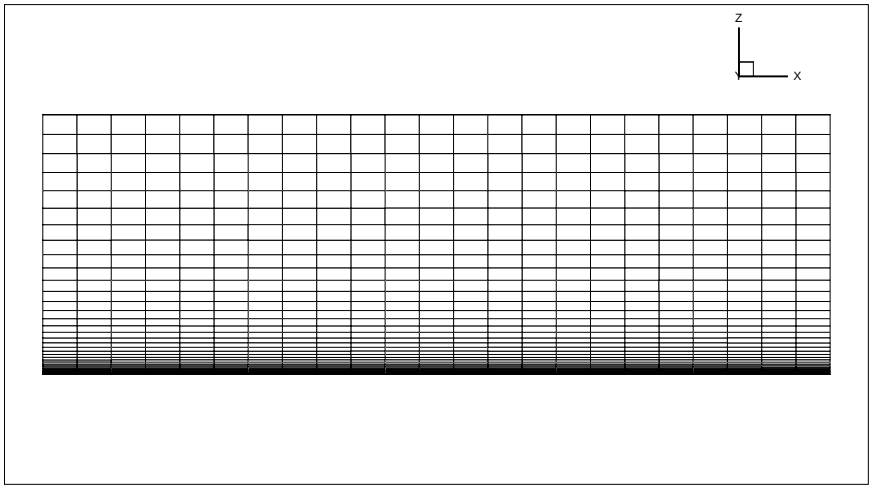

(b) medium grid closer to the wall

Figure 3.4: Medium Grid

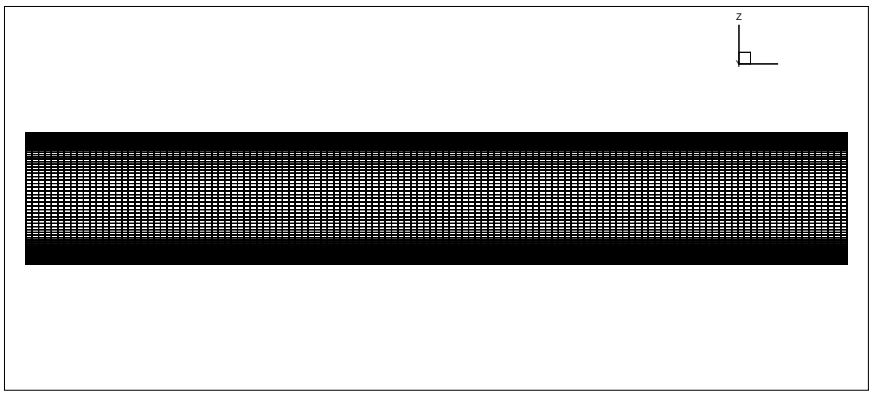

(a) fine grid for straight duct

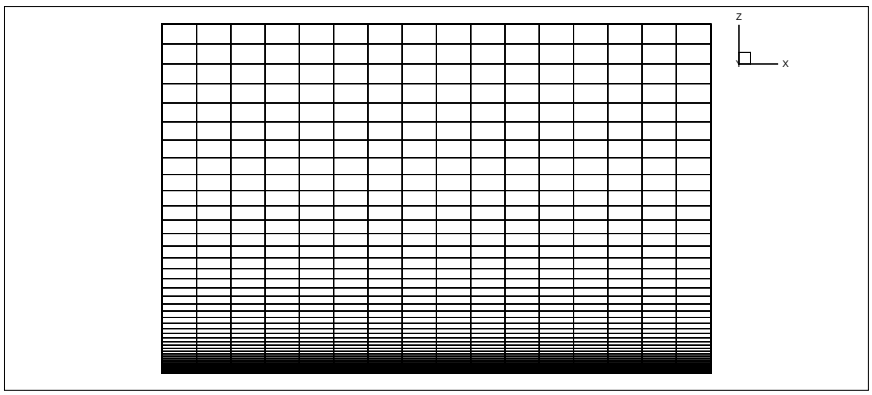

(b) fine grid closer to the wall

Figure 3.5: Fine Grid

3.2.2 Initial Conditions

A laminar parabolic profile along with perturbations (random noise ε) is used for the streamwise velocity u initialisation while v and w velocities are calculated based on u.

$$\begin{aligned} p(t=0) &= 1 \\ u(t=0,z) &= U_0\left[1-(z-1)^2\right](1+s\varepsilon) \\ v(t=0,z) &= s\varepsilon \times u(t=0,z) \\ w(t=0,z) &= s\varepsilon \times u(t=0,z) \\ E(t=0,z) &= \frac{p}{\gamma-1} + \frac{\rho}{2}\left(u^2+v^2+w^2\right) \end{aligned} \tag{3.2.1}$$

where U_0 is the centreline velocity, p is the pressure, s is the percent of perturbation and ε is a random number from -1 to 1. For the simulations s was equal to 0.1 as a perturbation of 10% was considered enough to help the flow reach a turbulent state.

The schemes employed were MUSCL 2nd MC with Low Mach Number Treatment (referred to from now on as MC and plotted as MC_LMNT), MUSCL 5th with LMNT (referred to from now on as MUSCL 5th and plotted as Mus5th_LMNT) and finally WENO 9th with no LMNT (referred to from now on as WENO 9th and plotted as Weno9th_NLMNT). The reason for not simulating using WENO 9th with LMNT is that the method becomes so under-dissipative, as also pointed out by Kokkinakis [1], that it was not possible to obtain a solution for any timestep chosen. At the same time the other two methods provided significantly improved results when using LMNT [1].

3.2.3 Mean Flow Properties

In the simulations the timestep keeps changing since it is recalculated based on the new solution obtained. This has to be taken into account since every timestep has a different weight in the averaging procedure. The averaging is performed based on time and not iteration number, thus taking into account the difference in duration of every timestep as mentioned before. The mean value of a variable ω in time is obtained through:

$$\bar{\omega}(t) = \frac{1}{t_{start}-t_{end}} \sum_{t_{start}}^{t_{end}} \omega \Delta t \tag{3.2.2}$$

and is used, in its discretised form:

$$\bar{\omega}^{N+1} = \bar{\omega}^{N} \frac{T^{N}_{total}}{T^{N+1}_{total}} + \omega^{N+1} \frac{T^{N+1}_{current}}{T^{N+1}_{total}} \tag{3.2.3}$$

This averaging procedure will be used to obtain the averaged values mentioned in the following subsection.

3.2.4 High Order Statistics

For the analysis of the results some statistics were implemented to export, variable profiles, Reynolds stresses, skewness and flatness. The following equation:

$$\omega^{'} = \omega - \bar{\omega} \tag{3.2.4}$$

is used to calculate the variables fluctuating component so that the Reynolds stresses can be calculated, with ω being the unsteady variable, $\left(^{'}\right)$ denotes the fluctuating component and $\bar{()}$ the mean value of the variable. It should be noted that since the conservative form of the NSE is used (calculation of momentum) the compressible solver can lead to variations in density. In order to account for the compressibility effects, velocity needs to be decoupled from the density and this is achieved through Favre averaging:

$$\bar{\omega} = \frac{\overline{\rho\omega}}{\bar{\rho}} \tag{3.2.5}$$

where the overbars (e.g. $\overline{\rho\omega}$) denote averages using the Reynolds decomposition. With the fluctuating velocity fields the rest of the statistics can be obtained like the root mean square (RMS):

$$\omega_{rms} = \overline{\sqrt{\omega'^2}} \tag{3.2.6}$$

Skewness and flatness are high order statistics that can determine if the flow is fully developed and are calculated as follows:

Skewness:

$$S_{\omega'} = \frac{\overline{\omega'^3}}{\overline{\sqrt[3]{\omega'^2}}} \tag{3.2.7}$$

Flatness:

$$F_{\omega'} = \frac{\overline{\omega'^4}}{\overline{\omega'^2}^2} \tag{3.2.8}$$

Skewness and flatness factors of velocity are statistical properties representing characteristics of turbulence. The production of the rate of dissipation of turbulent kinetic energy is directly related to skewness in isotropic turbulence [103].

3.3 Results and Discussion

In this section, some of the results obtained through the simulations will be presented. All the results obtained are based on a Reynolds number of 40,000 (based on the bulk velocity). In most similar channel or duct cases, an incompressible solver is used. In this case though, since CNS3D is a compressible solver, a low mach number along with Low Mach Number Treatment (LMNT) for some of the schemes were used. All the simulations here were carried out at a Mach number of 0.2 as that was the best for the incompressible nature of the flow based on a research conducted by Thornber [81].

The experimental data used for the following comparisons are based on an investigation carried out by Laufer [23] for a plain channel flow. His experiments were conducted at three Reynolds numbers, 12,300, 30,800 and 61,600. From a first study of the experimental data it can be noticed that the differences between Reynolds of 30,800 and 61,600 are very small compared to those of 12,300 to 30,800 thus allowing the assumption that although in the simulations a Reynolds number of 40,000 is used, a comparison with the experimental data at 30,800 can be performed.

The averaging window for this case is shown in Figure 3.6. From the fluctuations of the value of Re_τ and v velocity (for part of the window) it is made clear that the large scales are repeated inside this window thus ensuring the statistical steady state. The averaging time after the flow had developed was enough to ensure the statistical convergence of all length scales.

The averaged data used and presented in the following sections were extracted from the centre area of the domain along a line for the spacewise comparisons and from a marker in the middle for the pointwise data as shown in Figure 3.7. Linear interpolation is used whenever arbitrary lines are sampled from the computed flow field and presented here. Since the solver operates in dimensionless variables, when instantaneous results are presented, the dimensionless solution time t^* is given. The actual physical time can be recovered by taking into account the non-dimensionalisation applied, which is described by Equations 2.1.15.

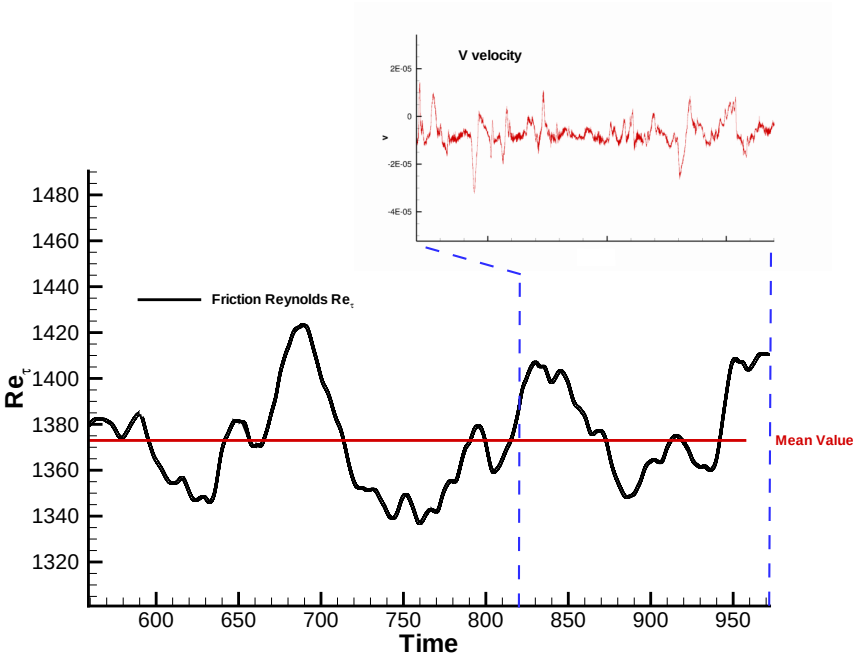

Figure 3.6: Averaging window

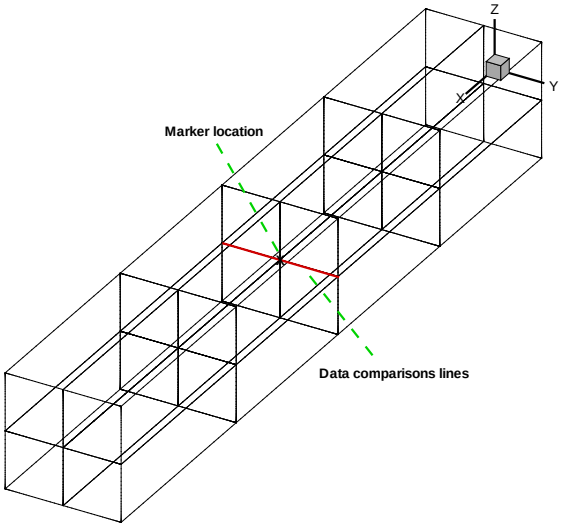

Figure 3.7: Data extraction areas for the straight duct

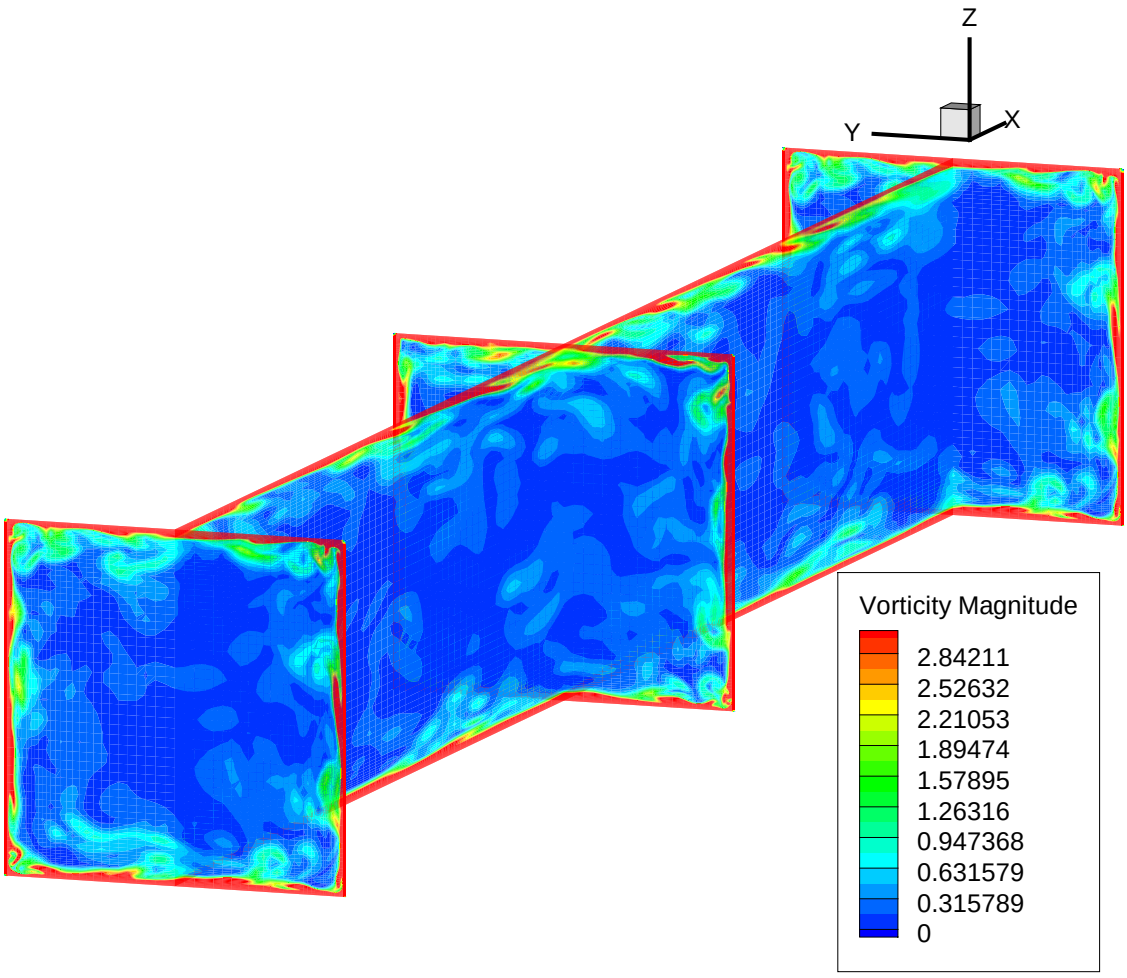

Figure 3.8: Vorticity magnitude for straight duct (t^*=969)

3.3.1 Flow development

In this subsection flow features obtained from the fine grid, with the WENO 9th with No Low Mach Number Treatment (NLMNT) scheme, are presented. The choice of this scheme for presenting the results is based on the work of Kokkinakis [1] where in a similar research (on a channel flow), it was the scheme presenting the most accurate results. The same was true in comparisons following in the next subsections. This will help in an initial evaluation of the code set-up. The different schemes will be compared more thoroughly and evaluated in the next chapter where a more complex flow will be studied.

From the results most of the flow characteristics expected in this kind of a flow and geometry were seen. Top velocities are located at the centre of the duct while velocities drop as the flow gets closer to the walls. In Figure 3.8 where the instantaneous vorticity magnitude is presented it can be seen that the highest values of vorticity are located near the

walls and corners. The turbulent characteristics of the flow are, as expected, located near the walls due to the boundary condition used. From a first observation of the results the capture of the physics of the flow was as expected and correctly located along the domain.

An interesting part of the flow is the generation of secondary motion near the corners. The corners cause secondary flows evident by the counter rotating vortices that can be seen in the area. These secondary flows are stress indused duw to the existance of the walls present in the area. Those flows are then transferred along the domain following the stream due to the streamwise velocity. Those effects are not clearly visible in 3D images of averaged or even instantaneous results so a closer look in the area is needed. Figure 3.9 presents the 2D vector projections for a duct slice along with a zoom close to a corner. The figure shows how the secondary motion appears near all four corners. The results presented in the figure were based on averaged data.

3.3.2 Grid comparisons

In order to perform an initial evaluation of the three different grids the WENO 9th scheme results will be used again for the reasons explained earlier. The results obtained from this method are presented here and compared to the channel experiment results. Because of the geometrical difference between the two cases and the influence of the two extra walls in the straight duct, all results were divided by the maximum value of the mean velocity in order to compensate for the non uniform shear stress effects. The comparisons were performed in the area shown in Figure 3.7.

The comparisons of the three grid sizes along with data from the experiment [23] are shown in Figure 3.10. The differences in streamwise velocity (a) are very small between the three grids providing satisfactory results compared to the experiment. The near wall difference is caused by the difference in boundary thickness between the channel and the duct and will be analysed in the following section when the schemes are compared. The turbulent intensity in the streamwise direction (b) is underestimated by the coarse grid in comparison to the medium and fine ones. The values closer to the wall are expected to be higher in the duct but then they are expected to follow a similar profile to that of the channel. The fine grid is in better agreement to the experimental data with the medium one following closelly. The final comparisons are those of v_{rms} and w_{rms} (c,d) where the differences between the produced results from the different grid sizes are made more obvious. Fine grid is in total agreement with the experimental data while the coarse grid significantly underestimates the turbulent intensity. The medium grid results are significantly closer to the fine grig ones than the coarse ones. In these two directions, duct results are expected to be closer to the channel flow data. Although the coarse grid follows the same pattern as the fine grid and the experiment, the values are significantly underestimated. The medium grid underestimates the values as well but with values much closer to the fine grid ones and the experiment.

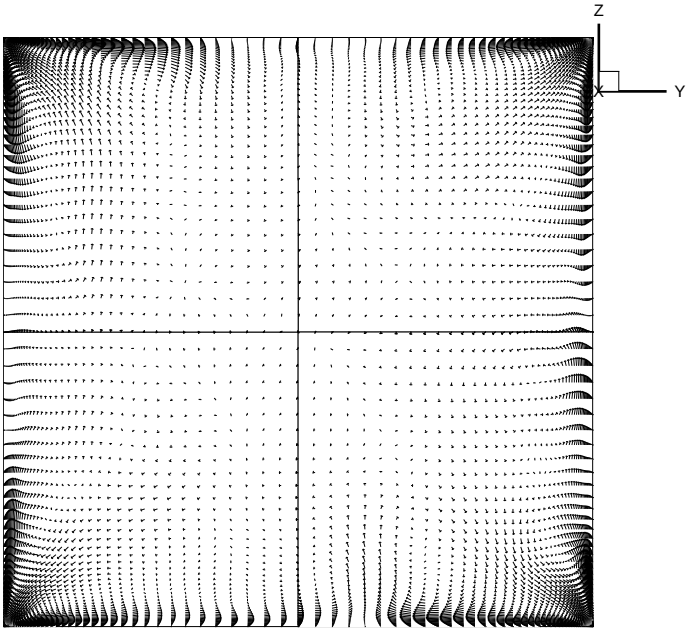

(a) slice at the middle of the duct

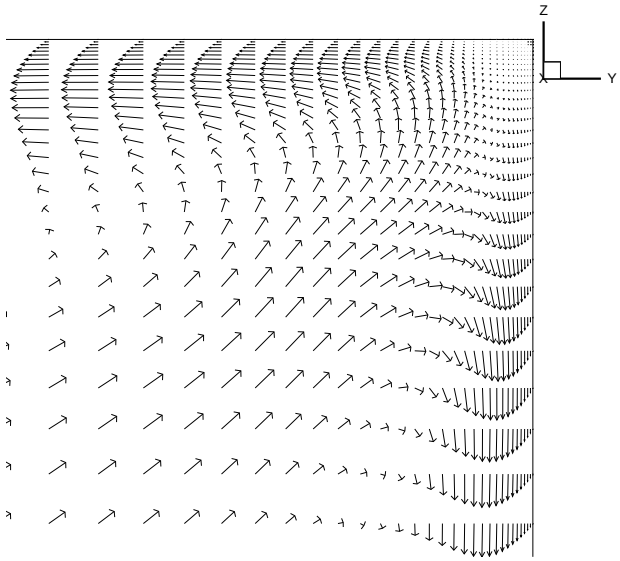

(b) corner zoom

Figure 3.9: Velocity vectors at the middle of the duct (averaged field)

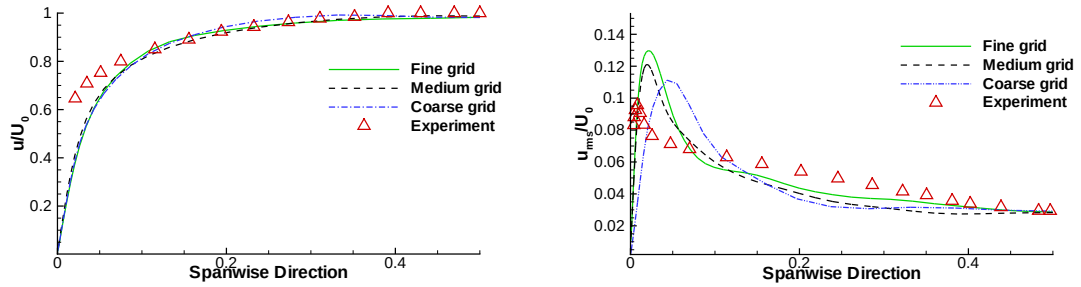

(a) Streamwise Velocity

(b) u_{rms}

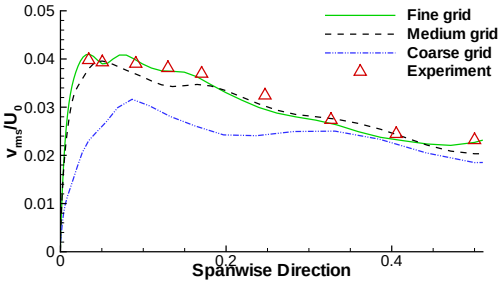

(c) v_{rms}

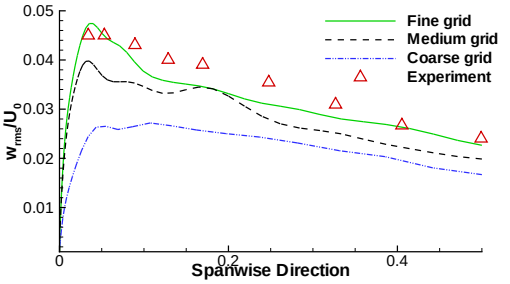

(d) w_{rms}

Figure 3.10: Grid comparisons at the centre of the duct

These observations lead to the safe conclusion that the flow inside the coarse grid may have reached a turbulent state with the help of the high order schemes employed but its magnitude was significantly lower to the one expected. The medium grid provided signifacantly imroved results compared to those of the coarse grid and in closer aggreement to those of the fine grid and the experimental data. Finally the fine grid presented a good agreement to the experimental data in the areas where comparisons were possible and where secondary motion effects from the duct corners were not so intense. From these comparisons the convergence towards the solution while the size of the grid increases is made obvious. The dicrease in discrepancies between the fine and the medium grid compared to those between the medium and the fine lead to the choice of the fine grid as the best choice for the comparisons that will follow.

More analysis on the differences between the duct and the channel flow are presented in the next subsection where the schemes employed are compared.

3.3.3 Numerical scheme comparisons

In this part the numerical results, in conjunction with experimental data for the channel [23], are presented. The results acquired from the fine grid will be presented here since they provide a better capture of the flow profile inside the duct as was also shown in the previous subsection. The schemes compared for the simulations are, as mentioned earlier, MC, MUSCL 5th and WENO 9th. The data for the comparisons are again drawn from the same area as for the grid comparisons and shown in Figure 3.7.

Figure 3.11 presents the comparisons between the different schemes and the channel experimental data for streamwise velocity and the turbulent intensity for all components of velocity. Through these comparisons not only the differences between the schemes can be seen but also the differences of the flow in a duct and a channel. The streamwise velocity (a) is captured almost in the same way by all three schemes especially closer to the middle of the bend (symmetry area) where the influence of the upper and lower walls in the duct is not so intense. In the near wall region though there are some discrepancies as can be expected. The flow in the channel accelerates closer to the wall compared to what happens in the duct since there is less friction in the experiment because of the absence of a top and bottom wall. Overall MUSCL 5th and WENO 9th have almost the same numerical results and present the best resemblance to the velocity profile provided by the experiment.

In the v_{rms} and w_{rms} comparisons (c,d) there are not significant differences expected between the duct and the channel flow. In both figures all schemes capture the profile found in the experimental results with WENO 9th ones though presenting the maximum accuracy. Especially in w_{rms} MUSCL 5th and MC seem to underestimate the intensity while WENO 9th presents good results even for the near wall region. The final value for comparisons that also presents interest in the differences between the simulation and experimental geometries effect in the streamwise turbulence intensity u_{rms} (b). As was mentioned in the flow analysis

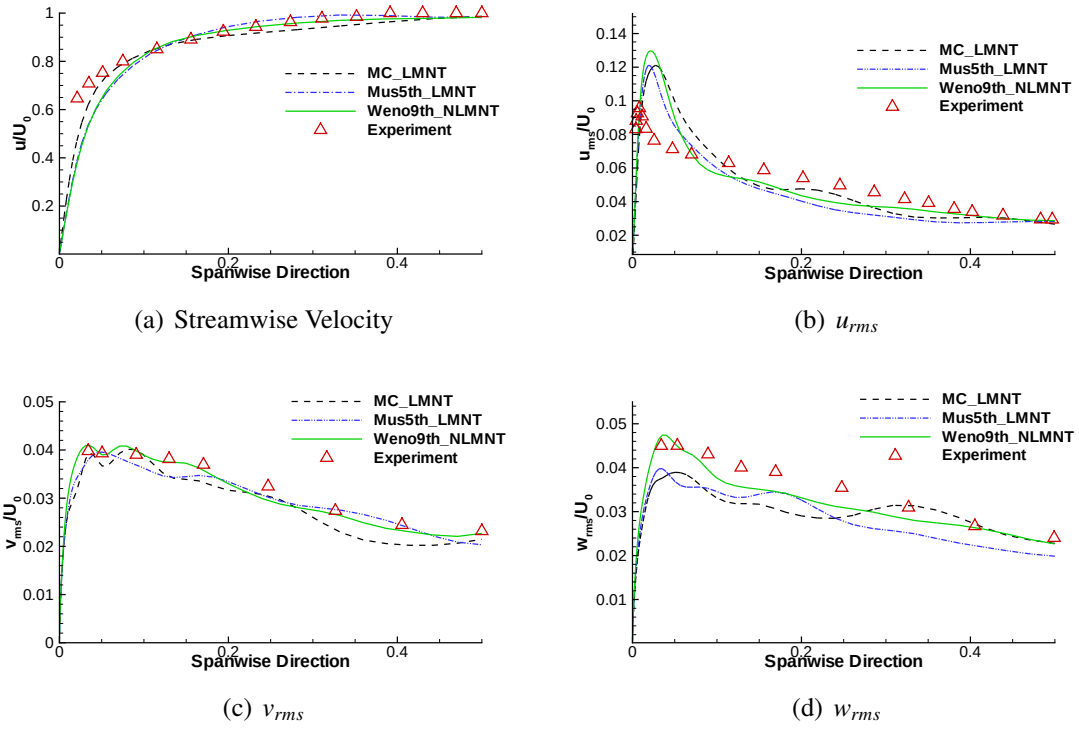

(a) Streamwise Velocity

(b) u_{rms}

(c) v_{rms}

(d) w_{rms}

Figure 3.11: Scheme comparisons at the centre of the duct

the existence of corners in the duct causes secondary flows that travel streamwise. Those are expected to affect the streamwise values compared to a channel flow where they do not appear. The duct case has a thicker boundary layer to that of the channel something that also affected the streamwise velocity as presented in (a). All these differences lead to two observations deriving from the numerical comparisons. The channel flow reaches its maximum turbulent intensity closer to the wall than the duct one but in the same time the maximum values for the duct are significantly higher. Also the maximum values of the turbulence intensity are retained for a larger area near the wall.

In order to locate differences between the schemes employed, small scales in the flow need to be studied so instantaneous results will be used. Vorticity magnitude iso-surfaces are presented in Figure 3.12. In theses plots only half of the domain is shown from the wall to the symmetry area and at a value of vorticity magnitude equal to 0.5. All three schemes seem to capture many small scales throughout the domain. The turbulence is mostly located near the walls as expected with more of the small scales located in that area. No clear differences in the turbulence intensity between the schemes can be seen in this figure. Figure 3.13 shows the vorticity magnitude for a slice in the middle of the domain. The higher vorticity is located in the surrounding walls with the only difference between the schemes being the distance from the wall where these intense phenomena present themselves. MC and MUSCL 5th seem to have high vorticity distributed from the wall, up to a distance of 0.1 from it while WENO 9th has high vorticity magnitude values closer to the wall. In general WENO 9th captures more small scales closer to the symmetry area compared to the other schemes proving to be slightly under dissipative compared to the other methods as was expected. LMNT though seems to assist both MC and MUSCL 5th in developing a turbulent flow almost identical to that of WENO 9th that does not employ it. The results presented in these figures where from instantaneous results since the small scales are better visible this way, compared to averaged ones.

High order statistics like skewness and flatness along with the power spectra can provide additional information about the nature of the flow. The data used are extracted from the centre of the domain (centre marker) as seen in Figure 3.7. The changes of u velocity at the marker over time are used to calculate the power spectra as well as the skewness and flatness. The power spectra for all schemes is presented in Figure 3.14. Table 3.2 presents the slopes in comparison to Kolmogorov's $-\frac{5}{3}$ slope [104]. It is apparent, from the presented data, that the flow is turbulent and not homogeneous but based on the slopes not far from a similar state. It is remarkable that all three methods have an almost identical slope pointing out again to the fact that turbulence is captured in almost the same way by all methods. A higher computed value of the slope might indicate that the actual state of the flow as computed is in fact less turbulent than one would have expected. Indeed it has been observed in the past that values of the slope, higher than 5/3 are typical for transitional flow regimes (e.g. [105]). One should however note that this "less turbulent" state inicated by the spectral properties might be due to the fact that the sampling points for the spectra were located in the middle of the duct, based on the assumption that the flow in the middle of the duct is likely to be more homogeneous and less affected by the secondary flows. However, the drawback of this approach is that due to the substantial clustering towards the

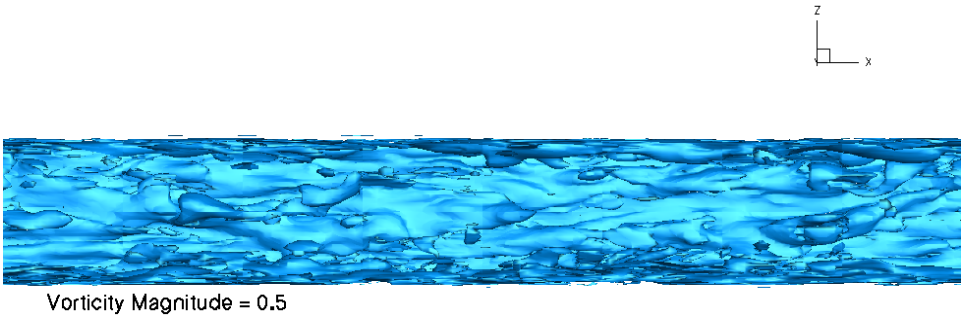

(a) MC

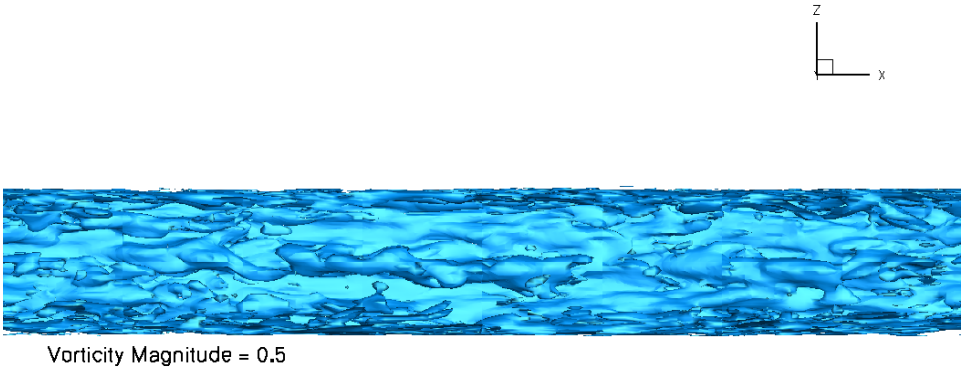

(b) MUSCL 5th

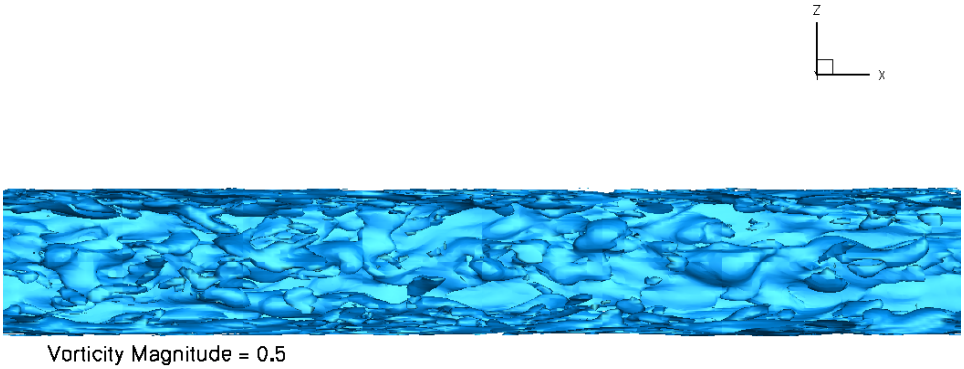

(c) WENO 9th

Figure 3.12: Vorticity Magnitude iso-surfaces at a value of 0.5 (t^*=969)

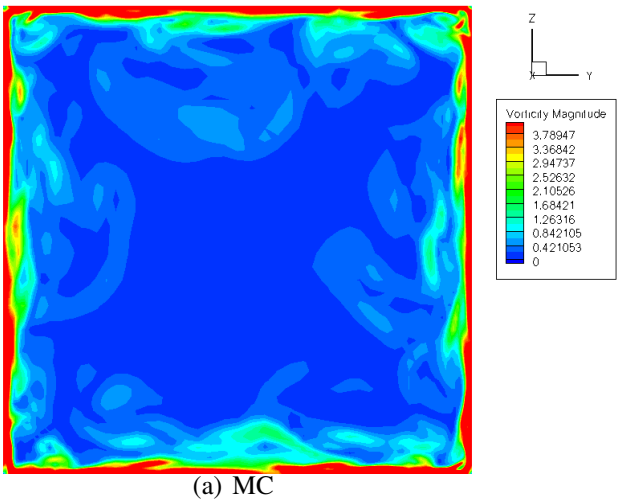

(a) MC

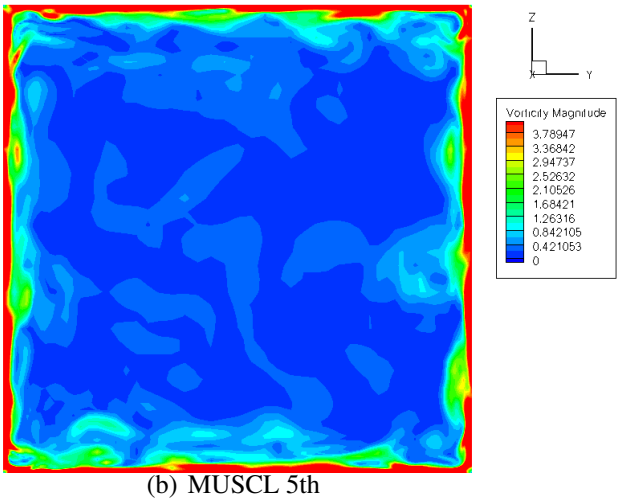

(b) MUSCL 5th

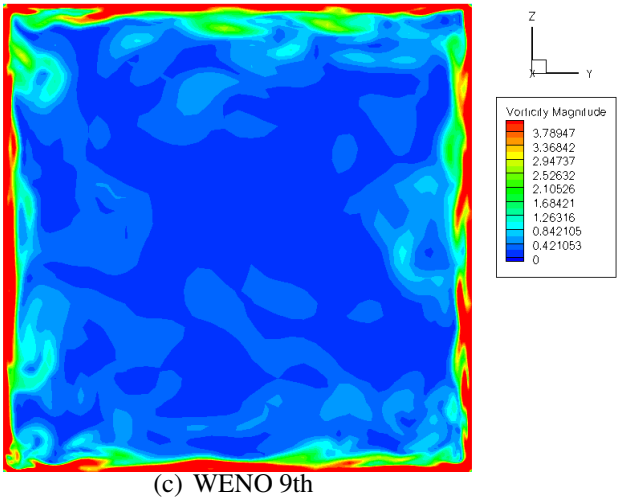

(c) WENO 9th

Figure 3.13: Vorticity Magnitude at the centre of the duct (t^*=969)

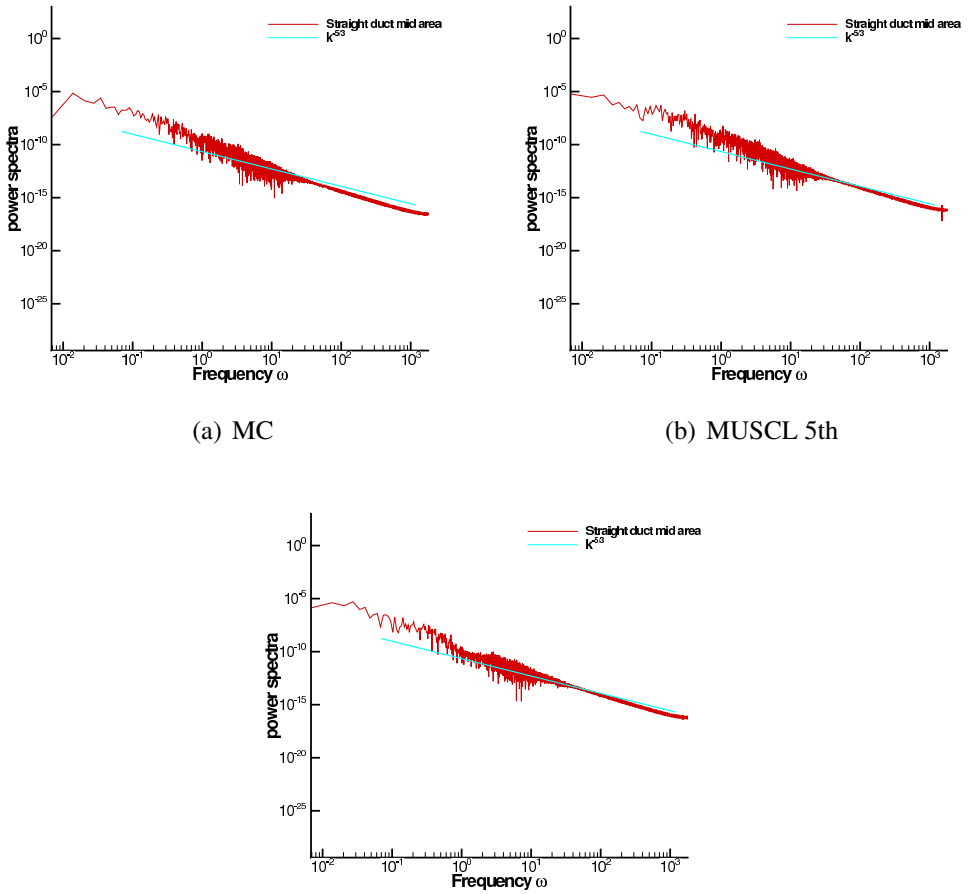

(a) MC

(b) MUSCL 5th

(c) WENO 9th

Figure 3.14: Power spectra for all schemes

wall, the mesh in the middle of the duct is quite coarse and therefore the dissipation of the scheme, which is linked to the grid cell size in the middle of the duct, is higher. This higher dissipation would also lead to the decrease of energy content in high frequencies, which would result in the increase of the slope.

Finally Figure 3.15 and 3.16 show the skewness and flatness at the same marker over time for WENO 9th. Based again on Kolmogov's theory about homogeneous turbulent flows [104] skewness is expected to fluctuate around zero and flatness around three over time since the marker is located in the middle of the duct. The first observation is that the fluctuations are insignificant after around 110 time units. This is an additional proof of the statistical convergence of the solution. It is also made clear that skewness and flatness fluctuate close and around the prementioned numbers thus providing further confirmation of the turbulence nature of the flow. If the linear fit of the results after 110 time units is taken the actual value of skewness and flatness can be calculated. These values are presented in Table 3.3 for all schemes. Almost all cases are close to the numbers presented

	Slope
MC	-2
MUSCL 5th	-2
WENO 9th	-1.99
Kolmogorov	-1.667

Table 3.2: Power spectra slopes for all schemes

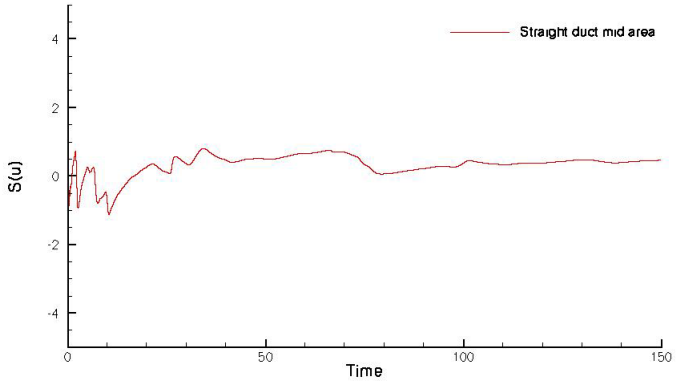

Figure 3.15: Skewness for WENO 9th

by Kolmogorov with WENO 9th though being closer to zero and three for skewness and flatness respectively. Similar results were also presented by experiments and DNS research, for the centre of duct flows but for lower Reynolds numbers as provided by Zhu et al. [106].

3.4 Conclusions

The flow inside a straight square sectioned duct was studied using ILES. The existence of four walls and corners in the flow, generated some interesting flow phenomena such as secondary motion. In the vicinity of the corners counter rotating vortices are formed leading to secondary motion that travels streamwise with the flow. The square shape of the

	$S(u)$	$F(u)$
MC	0.25	4.6
MUSCL 5th	0.68	2.3
WENO 9th	0.22	2.8

Table 3.3: Skewness and Flatness for all schemes

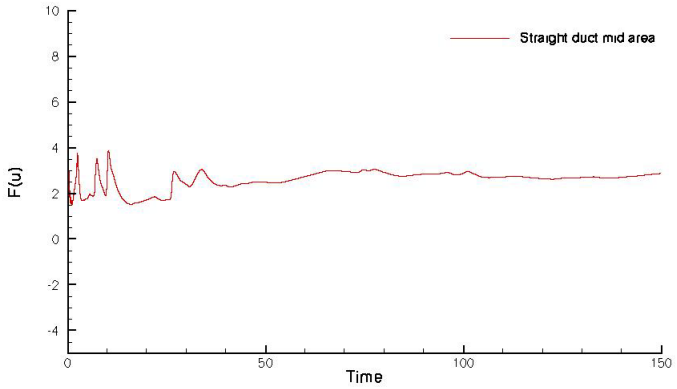

Figure 3.16: Flatness for WENO 9th

geometry makes the influence of this motion significant throughout the domain when in very wide ducts its influence outside the corner areas could even be neglected [27].

Comparisons with a channel flow showed that the middle part of the flow is very similar while the near wall region presents some differences based on the geometry effects. Streamwise velocity in the channel accelerates closer to the wall because of the lower friction and thinner boundary layer. The surrounding walls and generated secondary motion tend to affect the flow near the walls inside a duct compared to the channel. Streamwise turbulence intensity provided proof of that since the higher values for the channel were located closer to the wall compared to the duct where the magnitude rose further away. The duct's u_{rms} reached a much higher value that was also retained for a larger area while pulling away from the walls, showing the significant effect of the secondary motion to the flow characteristics. So, overall the value profiles in the duct and channel were almost identical with the near wall region being affected by the ducts geometrical uniqueness.

The different schemes employed were MC, MUSCL 5th and WENO 9th with the first two using LMNT as mentioned in the first parts of this chapter. The differences in the produced results between the schemes were small with all of them capturing the flow in almost the same way. LMNT proved to assist the capture of turbulence for the schemes that employed it significantly since MC and MUSCL produced almost the same turbulence intensities as WENO 9th that was expected to produce a lower numerical dissipation in comparison. All three schemes provided a turbulent flow of near homogeneous state capturing even small scales in the same way.

Since the comparisons were performed using channel flow experimental data, choosing the best performing scheme would not be well justified. The point achieved though, through this chapter, besides capturing flow phenomena and locating differences between a duct and a channel is the turbulent nature of the flow inside the domain. Since all three schemes provided a turbulent flow of almost the same magnitude they can be used in the next chapter for studying the flow in a more complicated geometry. The developed turbulent flow from

all three schemes will be used as the flow profile entering the L-bend geometry presented next. In that chapter the differences between the schemes are expected to be more obvious and along with the comparisons, towards experimental data, they are expected to indicate the best performing scheme for these cases and at the same time further assess the influence of LMNT.

CHAPTER 4

L-bend

As mentioned in the introduction there is great emphasis in the literature on geometries with strong curvatures. The existence of curves in pipes, ducts and channels presents an interesting case for study mostly because of the secondary flows developed and the flow separations existing in some cases. CFD studies in these cases can provide an insight that is not easily acquired through experiments.

4.1 Problem description

In the previous chapter the flow inside a square sectioned straight duct was studied. The developed turbulent flow provided by that case will be used in this chapter as the developed turbulent flow entering the domain. The geometry under study will be a square sectioned duct with a 90^o bend. The geometry was based on the one used in the experimental case by Taylor et al. [30, 107] and simulations on that by Raisee et al. [108].

All the geometry dimensions will be presented in relation to the Characteristic Length H which represents also the height of the duct. This length H is equal to 1 in this case thus making nondimentionalization a much easier task. The bend radius to duct height ratio (R_c/H) of the geometry was kept steady at 2.3 while the rest of the dimensions were adjusted to the simulation needs. Compared to the RANS simulations by Raisee et al. [108] where the area before the bend was equal to 9 H, in order to allow the flow to develop before it entered the bend, was replaced by 1.57 H in this case for the computational cost to be minimised. This change was possible since as already mentioned the flow provided from the previous case was fully developed so there was no need for extra space for the flow to develop until it reached the bend. The length after the bend leading to the outlet was set equal to $26H$. The length of the downstream part of the duct leading to the outflow was chosen on the basis of empirical correlations for entrance-length given by Munson et al. [109].

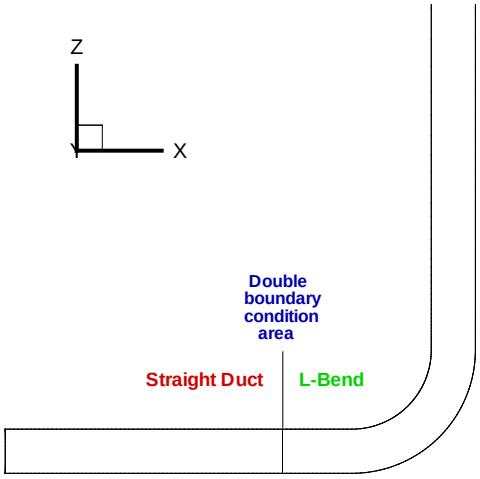

Figure 4.1: Coupled geometry with double boundary condition

The boundary conditions used were inflow, outflow and no-slip wall. The difference in this case is how the developed turbulent flow was supplied to the main geometry with the L-bend. The L-bend geometry and the straight duct one (presented in the previous chapter) were coupled and simulated simultaneously for most of the running time. In order to achieve this, a double boundary condition was implemented at the end of the straight duct and the entrance of the L-bend. There, except for the periodic boundary condition that kept recycling the flow in the straight duct, was the boundary condition that acted as the L-bend inlet, thus after a while providing the L-bend geometry with a fully developed turbulent flow. This can be made visibly clear in Figure 4.1. The simulations were conducted at a Reynolds number of 40,000 as in the straight duct case and the experiment.

The experiment used for validation and general comparison purposes was conducted by Taylor et al. [30, 97] using Laser-Doppler velocimetry. Their research was concerned with hydrodynamically developing flow at the entrance to square cross section, 90^o bends of 2.3 radius ratio for laminar and turbulent flow. They had two basic reasons for their research. The first was to provide the basis for understanding the influence of developing entry flow in bends under laminar and turbulent regimes [30] and the second to provide data for the purpose of validation in future CFD studies. The experimental geometry consisted of a 90^o bend of 92mm mean radius and of ratio equal to 2.3, with upstream and downstream tangent lengths of 0.3 and 2 meters respectively. The dimensions of the cross section (40x40 mm) conformed closely to those of the tangents. The experimental geometry is illustrated in Figure 4.2 [107].

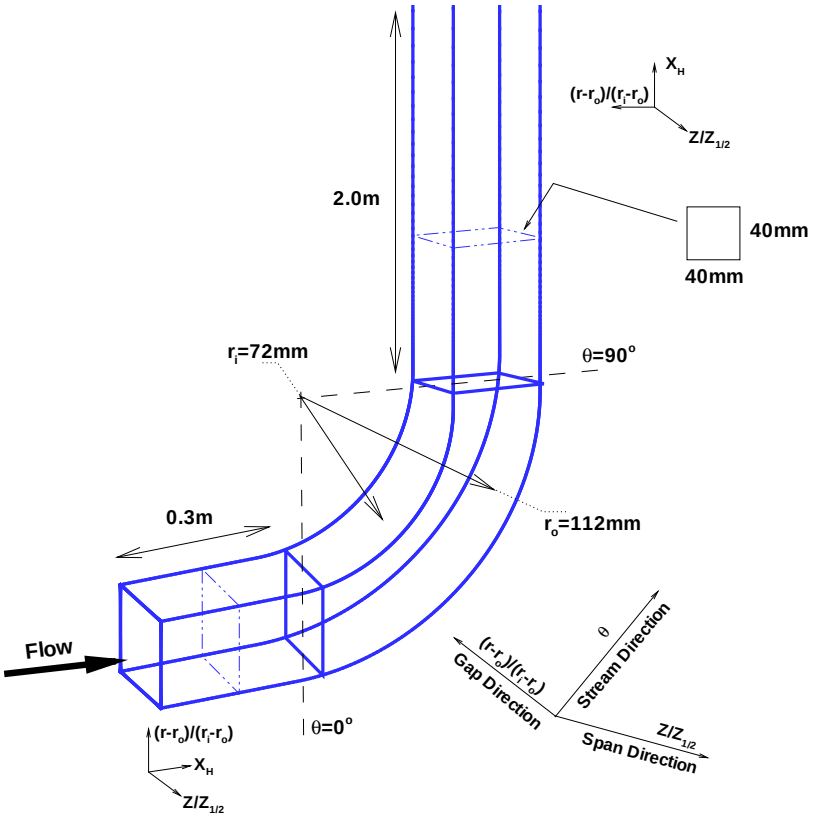

Figure 4.2: The experimental geometry

Grid	Grid Size	Δz	y^+
Coarse	49x49x129	0.001	2.4
Fine	97x97x257	0.0005	1.2

Table 4.1: Grid and first cell sizes

4.2 Computations

In this section the grid used along with the initial conditions and the methods for calculating the flow properties are presented.

4.2.1 Grid

Two grids based on the same geometry and with a different number of cells (coarse and fine for the lower and higher numbers respectively) were generated using Gridgen V15.11. The grid generation and clustering were based on the straight duct case for the coupling of the grids to work and the developed flow of the previous case to be easily used by entering this case. As before, most of the cells were located in the near wall region but also in the bend section of the geometry. The bend area is the main area of study since most of the flow characteristics are either present in there or it is the location of cause for their formulation.

The number of points in the z and y direction were the same and equal to 49 for the coarse and 97 for the fine grids respectively as in the previous case. In the x direction 129 and 257 points were used respectively resulting to the two grids of sizes 49x49x129 and 97x97x257. So in conjunction with the straight duct, that was coupled with the L-bend, the resulting grids were 49x49x195 and 97x97x386 for the coarse and fine grids respectively. The grid sizes and the distance of the first point from the wall are shown in Table 4.1. Figures 4.3 to 4.5 show the grids along with the high clustering areas.

4.2.2 Initial Conditions

As mentioned above the inflow configuration for this case is based on the need for a correctly defined developed turbulent flow. The flow enters the geometry already developed based on the parallel simulations on the straight periodic duct of the previous chapter. The two geometries are coupled and the periodic boundary condition at the end of the straight duct is at the same time the inflow for the L-bend grid. Some initial conditions though are used in the L-bend grid to make the development of the flow inside this geometry smoother and faster. The basic difference to the initialisation of the straight duct is that there is no use of perturbation here and values are multiplied by a number based on the turning of the stream while it enters and exits the bend. This way u and w velocities follow the i and k

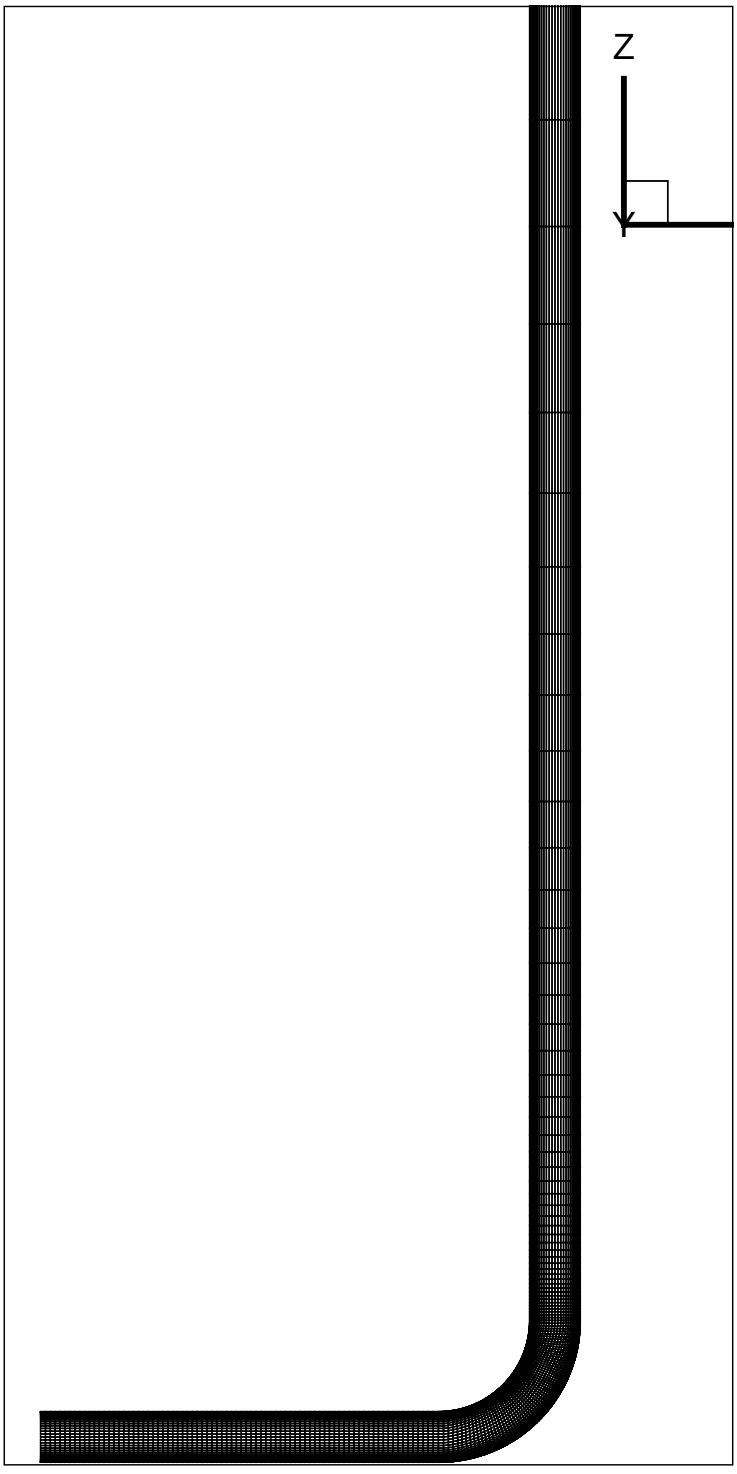

Figure 4.3: Coarse Grid coupled with the straight duct

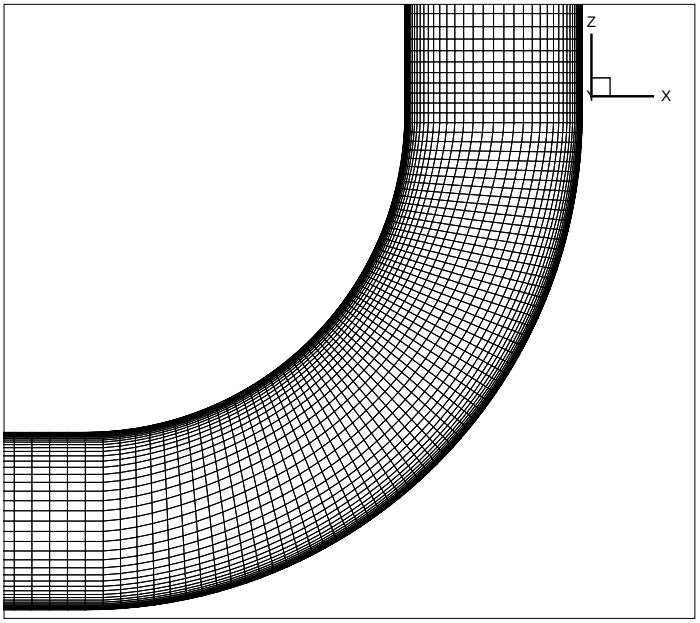

(a) Bend area

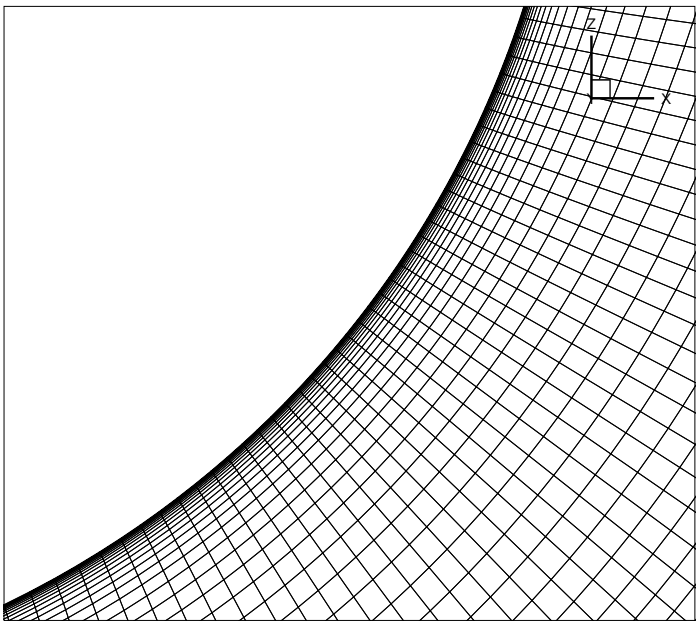

(b) Bend area - zoom in (internall wall)

Figure 4.4: Coarse Grid - Bend Area

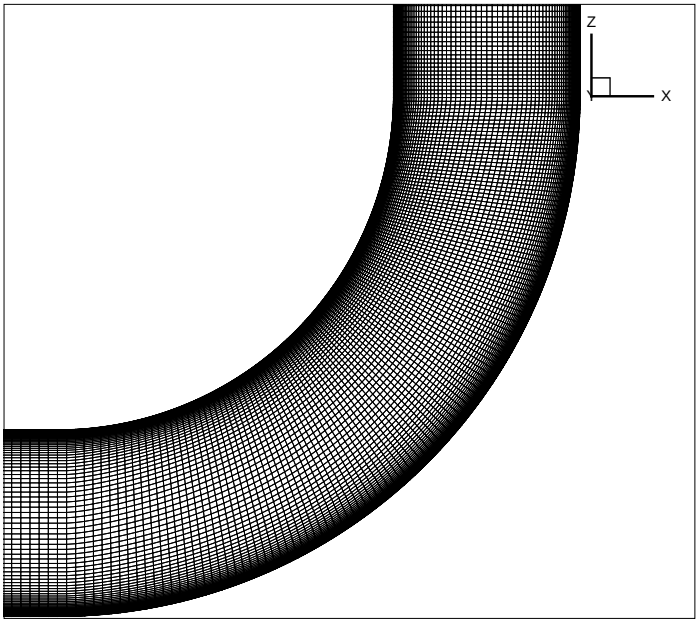

(a) Bend area

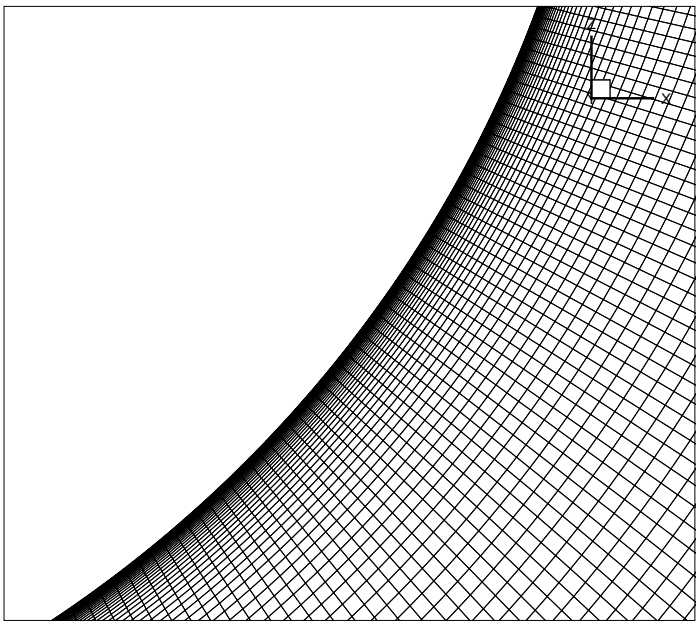

(b) Bend area - zoom in (internall wall)

Figure 4.5: Fine Grid - Bend Area

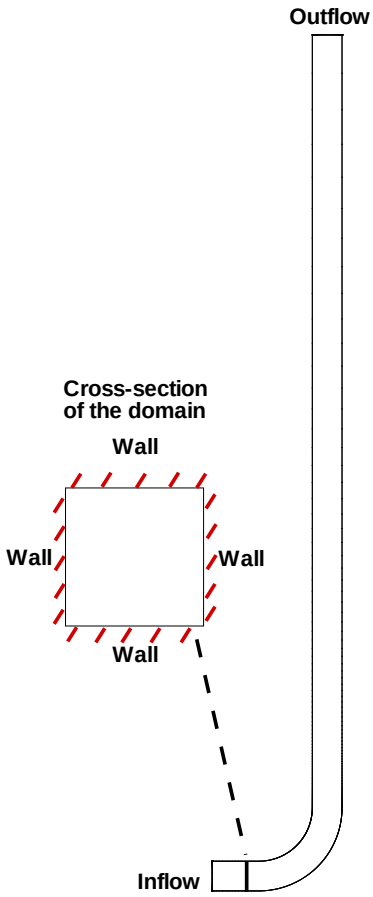

Figure 4.6: L-bend boundary conditions

directions respectively so that the first will be the streamwise and the second the gapwise velocity even when the flow turns inside the bend.

$$\begin{aligned} p(t=0) &= 1 \\ u(t=0,z) &= U_0 \times cos(\theta) \\ v(t=0,z) &= 0 \\ w(t=0,z) &= U_0 \times sin(\theta) \\ E(t=0,z) &= \frac{p}{\gamma-1} + \frac{\rho}{2}\left(u^2+v^2+w^2\right) \end{aligned} \tag{4.2.1}$$

where U_0 is the centreline velocity, p is the pressure and θ is the angle of turn because of the bend. The way θ is defined can be seen in Figure 4.7.

As mentioned before the boundary conditions used were inflow, outflow and wall, and are as shown in Figure 4.6. All the simulations are performed with a Reynolds number of 40,000 based on the bulk velocity. As in the straight duct case, a compressible solver was

used (CNS3D) with the same low Mach number of 0.2. The schemes employed were again (as in the straight duct case):

- MUSCL 2nd MC with Low Mach Number Treatment (referred to from now on as MC and plotted as MC_LMNT),
- MUSCL 5th with LMNT (referred to from now on as MUSCL 5th and plotted as Mus5th_LMNT) and finally
- WENO 9th with no LMNT (referred to from now on as WENO 9th and plotted as Weno9th_NLMNT).

The reason for not simulating using WENO 9th with LMNT is again the fact that the method becomes so under-dissipative, as also pointed out by Kokkinakis [1], that it was not possible to obtain a solution for any timestep chosen.

The procedure for the simulations can be considered complex but was designed in such a way as to reduce the computational cost. Initially the straight duct with MC was simulated until the flow developed. Then the straight duct was coupled with the L-bend and again simulations ran for some time until the flow reached an almost developed state for the new domain. The produced data up to that point were used to initiate simulations for the MUSCL 5th and WENO 9th schemes as well. Once a case reached a developed turbulent flow the averaging commenced for a period of time, enough to ensure the statistical convergence of the solution as shown in Figure 4.8 for the WENO 9th case. Through this procedure computational costs were reduced since only one case had to be initialised based on the equations mentioned above while the two others started with a profile much closer to the desired one.

4.2.3 Mean Flow Properties and High Order Statistics

The mean flow properties and the high order statistics used in this case are the same as in the straight duct and are shown in subsections 3.2.3 and 3.2.4.

4.3 Results and Discussion

In this section, the results obtained through the simulations are presented. The results used for the comparisons (especially with the experimental data) were extracted from specific areas in the domain where experimental data [107] was available. The comparisons were made along five slices and along five lines on those slices. The slices were extracted at the area right before the entrance of the bend ($x = -0.25$), three areas inside the bend ($\theta = 30^o$,

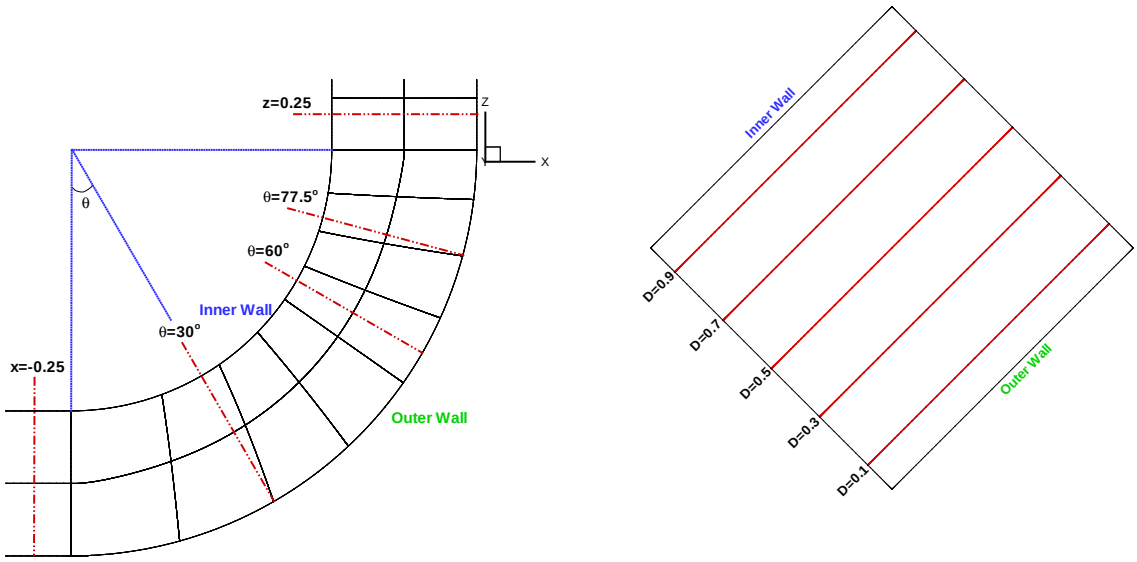

(a) Slices (b) Lines along slices

Figure 4.7: Data areas used for comparisons

$\theta = 60^o$ and $\theta = 77.5^o$) and finally the area right after the exit of the bend ($z = 0.25$). On these slices data along five lines were extracted based on the distance from the bottom (outer) wall at $D = 0.1, 0.3, 0.5, 0.7$ and 0.9. A full picture of the experimentation areas is given in Figure 4.7. Linear interpolation is used whenever arbitrary lines are sampled from the computed flow field and presented here. Linear interpolation is used whenever arbitrary lines are sampled from the computed flow field and presented here. Again here ,as in chapter 3, because the solver operates in dimensionless variables, when instantaneous results are presented - the dimensionless solution time t^* is given. The actual physical time can be recovered taking into account the non-dimensionalisation applied, which is described by Equations 2.1.15.

The time window used to average the results was the same as in the straight duct case and was enough to ensure the statistical convergence of all length scales, Figure 4.8.

4.3.1 Flow development

In this subsection, flow features obtained from the fine grid simulations are presented. The results obtained using WENO 9th on the fine grid will be used since this was the set-up presenting the best results compared to experimental data as will be shown in the following subsections. The capture of certain flow physics is studied by seeing the outputted results

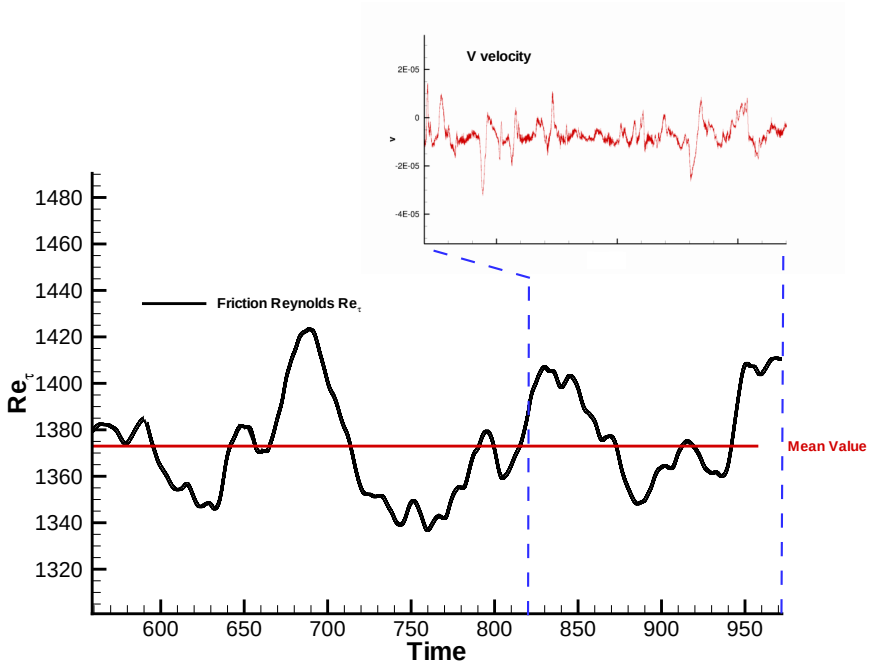

Figure 4.8: Averaging window

based on what is expected from this kind of flow and geometry as found on experimental and simulation results in the literature.

In the produced results flow characteristics that were expected, as in the straight duct case, are seen again. Figure 4.10 shows the incoming flow in the bend area moving closer to the upper wall due to the centrifugal forces and then moving away after a while transferring to the opposite side of the bend as physically expected. The angle of the bend is such that causes the flow to gradually move towards the outer wall without having a separated flow, a note made also in the experiment by Taylor et. al. [107] where no separation was observed.

Figure 4.11 shows the pressure distribution in the bend. The pressure along the outer wall of the bend starts rising while in the inner wall the opposite is observed. This change in the pressure can also justify the attachment of the higher velocities on the inner part of the bend. Pressure gradually tends towards a uniform state after the exit of the bend leading to a gradual uniformity of the streamwise velocity as well, Figure 4.9. The effects of the secondary motion present in the bend and the pressure difference between the entrance and the exit of the bend cause a gradual deceleration of the flow along the inner part of the bend and at the same time its acceleration at the outer part. After the exit of the bend, the velocity is gradually brought to a balance between the inner and outer parts of the duct (towards the outflow). These observations were made in the experiment as well [30, 107] where an adverse pressure gradient was noticed in the outer wall region while a favourable one existed on the inner wall causing deceleration and acceleration of the flow similar to

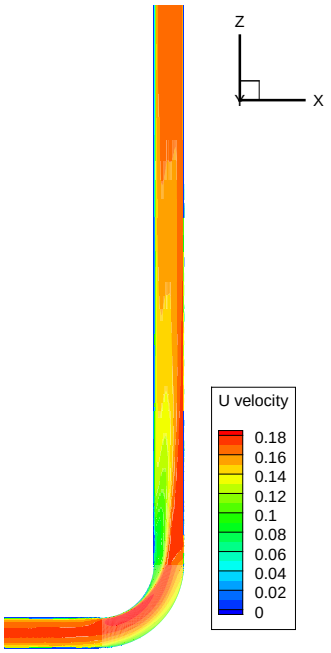

Figure 4.9: L-bend case Streamwise Velocity (averaged field)

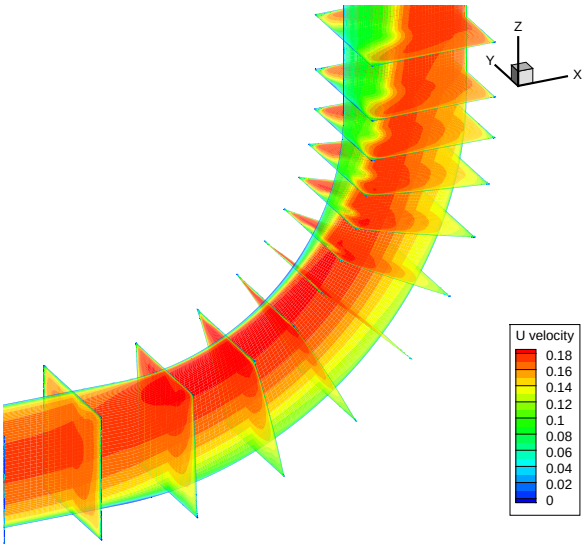

Figure 4.10: Bend area Streamwise Velocity (averaged field)

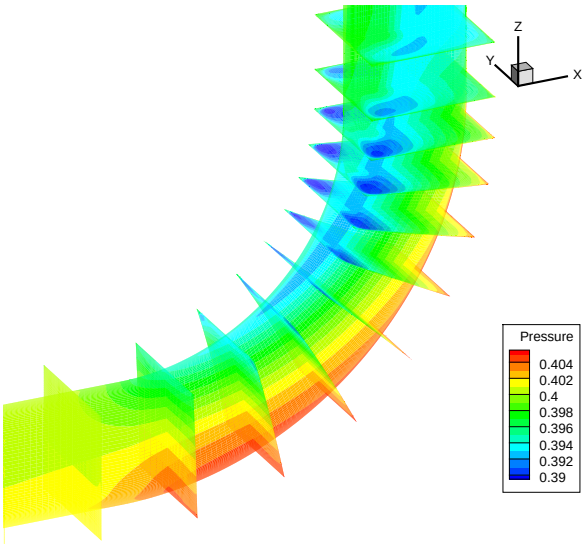

Figure 4.11: Bend area Pressure (averaged field)

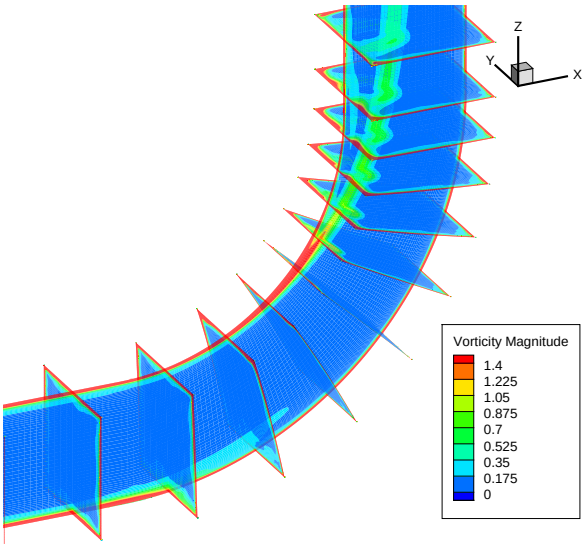

Figure 4.12: Bend area Vorticity Magnitude (averaged field)

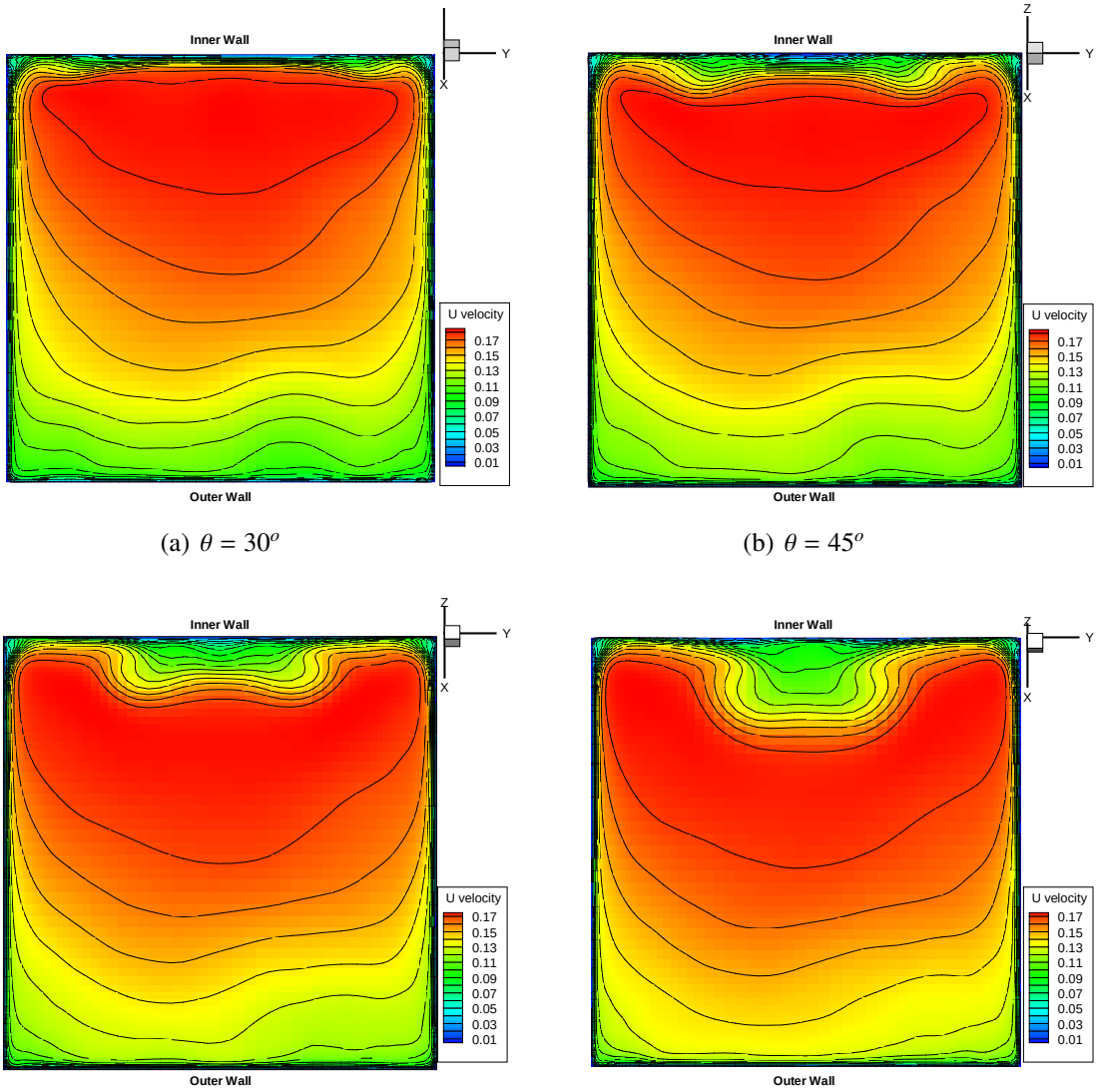

(a) $\theta = 30^o$ (b) $\theta = 45^o$

(c) $\theta = 60^o$ (d) $\theta = 75^o$

Figure 4.13: Streamwise Velocity on slices along the bend (averaged field)

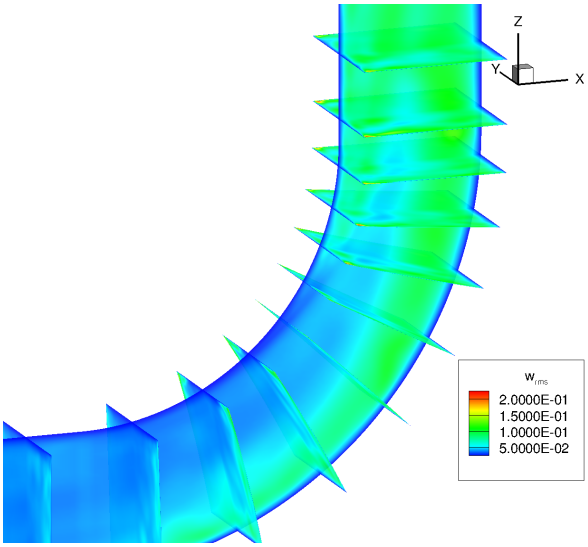

Figure 4.14: Bend area w_{rms} (averaged field)

that found in our simulations.

In Figure 4.12, the vorticity magnitude along the bend is illustrated. Further to the expected areas of intense vorticity like the near wall regions and the corners (secondary flows as presented in the straight duct case) there are two areas of interest. The first one is located at the entrance of the bend where vortices are observed close to the outer wall area and are the ones showing the movement of the flow towards the inner wall especially near the side wall areas. The second is a more intense phenomena and is located in the inner wall starting around 45^o. There are two counter rotating secondary vortices visible that show the movement of the flow from the inside of the duct closer to the outside wall and are induced by the curvature. The same vortices were pointed out in the experiment based on their numerical results as well and were located in the same areas [30, 107]. In the RANS simulations [108] the more intense vortices started forming again at around 45^o with approximately the same effect on the flow. The influence of these vortices in the streamwise velocity can be seen in Figure 4.13 where the lower velocities near the inner wall and close to the symmetry plane are caused by the vortices moving the flow towards the outer wall at that area. The gradual effect of the bend is made clear in this figure since at 30^o, where the phenomena has not appeared yet, the higher velocities are near the outer wall but as the effect appears it becomes more and more intense as the flow progresses towards the exit.

A study of the turbulence intensity can provide further detail and proof of the existence and influence of the two counter rotating vortices and the generation of the secondary motion. The influence of the secondary motion is more obvious at around 60^o and at the exit of the bend the turbulence is anisotropic with high w_{rms} near the outer wall (Figure 4.14) and high u_{rms} near the inner wall (Figure 4.15). The data in both figures are averaged.

Based on the existing experimental data and flow patterns available in the literature,

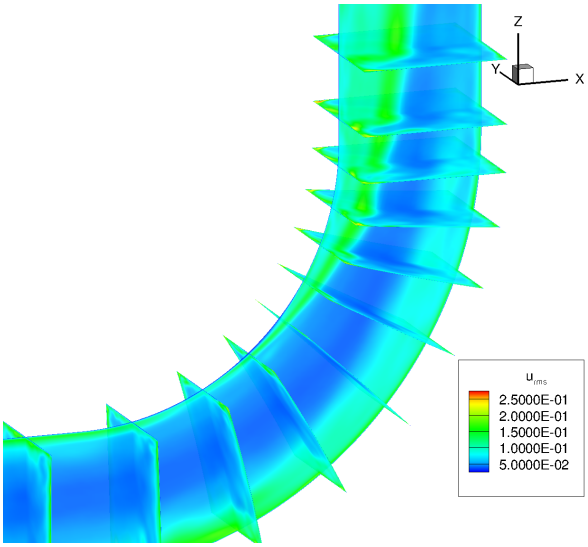

Figure 4.15: Bend area u_{rms} (averaged field)

as described above, it can be concluded that the simulations provide consistent physical insights to the flow characteristics.

The basic advantage of this CFD approach to the problem at hand will be utilised in order to provide a closer look and analysis of the important characteristics of a turbulent flow in square sectioned duct with a 90^o bend. The experiments provide data in some specific areas and only a few (if any) visualisations of the flow. At the same time most of the simulations in the literature provide either methods for producing yet more numerical data in specific areas as well as limited 2D visualisations of the flow. An important target of this research is to provide initially an accurate CFD tool for correctly capturing the flow while at the same time provide averaged data for the whole domain. The ability to provide complete 3D images for the whole domain for a number of variables provides a significant advantage towards better analysing and locating the characteristics of this kind of flow. So the initial observations made above can be further justified and analysed on more data.

Starting from the entrance of the bend and studying Figure 4.10 the flow accelerating towards the inner part of the bend is shown. This movement of the flow can also be seen in Figure 4.16 where some streamlines along the side wall of the bend are plotted. Even before entering the bend the flow starts moving towards the inner wall, a movement that is more intense closer to the side walls, an interesting observation made also by Taylor et al [30, 107] in their experiments. The same figure shows the influence of the pressure that leads the streamtraces closer to inner wall. The traces also show a swirling motion of the flow. The first reason for this disposition is the rapid rise in pressure at the outer wall right before the entrance of the bend and its gradual drop at the inner wall as seen in Figure 4.11. The second reason is that the vortices forming in the outer wall of the bend force the flow to move towards the inner area of the bend. This is made clear in Figure 4.17 where the vortex forming in a corner close to the outer wall forms the streamlines leading inwards

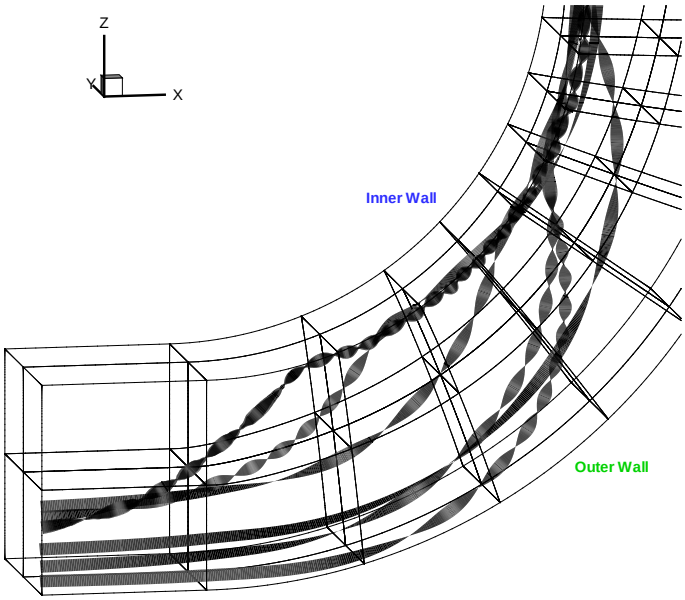

Figure 4.16: Streamtraces near the side wall of the bend

and closer to the convex (inner) wall. The figure shows a 2D projection of the streamlines so the lines that look as if they are going through the bottom wall are actually following the stream and go inwards. All data for the figures presented were based on averaged data.

As the flow moves further into the bend there is a second great influence to the flow because of secondary motion effects. The flow starts accelerating at the outer and side walls while decelerating in the middle (symmetry area) and closer to the inner wall. This is seen by some strong counter rotating vortices as plotted in Figure 4.12. A slice at 60^o inside the bend shows the counter rotating vortices more closely (Figure 4.18). As seen in the vectors along that area the flow from the outer wall is transferred towards the inner following a path very close to the side walls and is then transferred back to the outer wall through the symmetry area of the domain. This secondary motion affects the flow even after exiting the bend as obvious from the prementioned figures mentioned before but gradually, as the flow moves farther away from the bend, its intensity and effect diminishes leading to an evenly distributed velocity flow away from the bend as was seen in Figure 4.9. In the experiment the same effects at 60^o can be seen with the streamwise velocity at the symmetry area near the inner wall being significantly smaller than the rest of the domain [107]. In the RANS simulations [108] the counter rotating vortices located show the same effect in the flow as pointed out in this work. Figure 4.19 shows how the counter rotating vortices progress inside the bend as the flow moves towards the exit. A first pair of counter rotating vortices appears at around 45^o. Remarkably, this pair was not observed in either experiments or RANS simulations reported to date. However, the magnitude of these secondary vortices as well as the corresponding values of gapwise velocity inducing this flow are quite small. One might put forward a proposition that these were not observed experimentally because of lack of resolution (experimental error in velocity measurement was ~3% [107]) and not

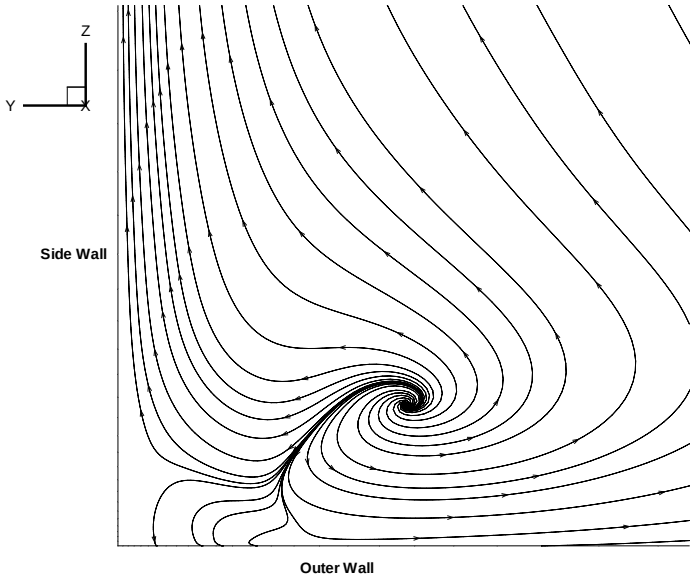

Figure 4.17: Vortex in the lower corner of the bend entrance (averaged field)

observed in RANS because of excessive dissipation. On the other hand it is possible that these vortices are an artefact in the ILES simulations because of the fine grid and insufficient dissipation. It is not possible to assert one or the other conclusion at present stage without a detailed experimental study designed to either prove or disprove the existence of these structures. Later on, each vortex bifurcates into two forming the large counter rotating vortices described in the experiment. As the flow moves closer to the exit the main pair of vortices moves closer to the middle of the duct. At around 60^o, two smaller vortices are formed that are moving gradually closer to the inner wall, a feature again not presented in the experiment but observed in the RANS simulations.

Finally more detailed observations can be made by studying the numerical changes along the bend. In Figure 4.20 the changes in the streamwise velocity u and the turbulence intensity u_{rms} along the bend from entrance to exit are presented. The areas shown are at the centre of the flow and closer to the inner and outer walls. The data used are again from the fine grid with WENO 9th.

Starting from the outer wall the streamwise velocity (a) is influenced by the vortices located in the area thus having a magnitude drop near the symmetry area of the domain. At 60^o the flow is decelerated compared to the entrance but at the point it reaches the exit it has been significantly accelerated. The vortices at the entrance near the outer wall cause a rise of the turbulent intensity near the symmetry area (b) while when moving inside the bend and towards the exit the intensity keeps dropping in the area as expected from the experiment descriptions. At the same time near the inner wall the flow enters in an almost uniform way (e) but is significantly accelerated in the near wall region inside the bend. The two counter rotating vortices in the area cause the lower velocities seen in the symmetry

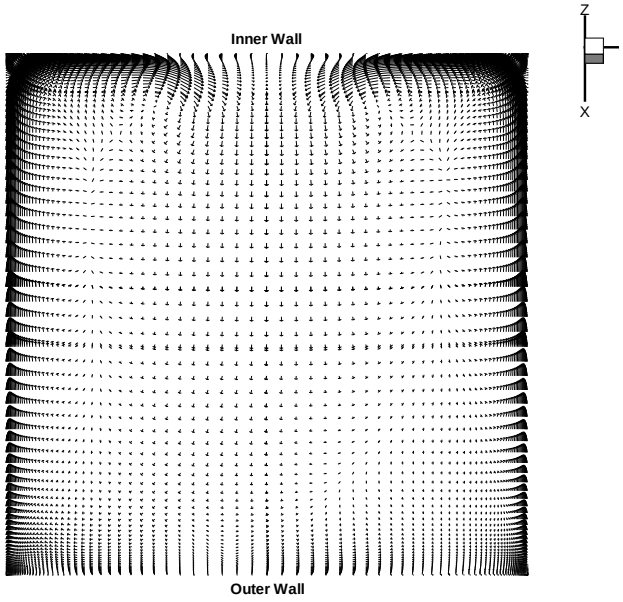

Figure 4.18: Velocity vectors at a 60 degree angle slice (averaged field)

area as described both in the experiment and RANS simulations [107, 108]. The turbulent intensity for the inner wall is higher after the influence of the counter rotating vortices with it significantly rising close to the symmetry plane because of their existence (f). When the flow reaches the exit it has been decelerated since the flow in the outer wall is the one accelerating at this point. The flow at the centre of the flow (c) remains almost the same in the symmetry area with the differences located near the side walls where the flow is higher as the flow moves into the bend and towards the exit. The turbulent intensity in this area remains almost steady throughout with a drop in the near side wall region compared to the entrance of the bend (d) mostly due to the transfer of the disturbance closer to the inner wall.

The amount of data available through this study presented an important advantage since a number of variables could be extracted at any area of the domain and 3D graphics were made available as well. This way, locating the flow characteristics and the influence of the bend was made easier and their visualisation much clearer through 1D, 2D and 3D data analysis.

4.3.2 Grid effect

The next step will be comparison of the different grids used based on the experimental results provided (and mentioned in the introduction of this chapter) which will justify the use of the fine grid results for the analysis above. The areas of importance for comparisons are many, so only a few will be presented here, while more can be found in Appendix A.

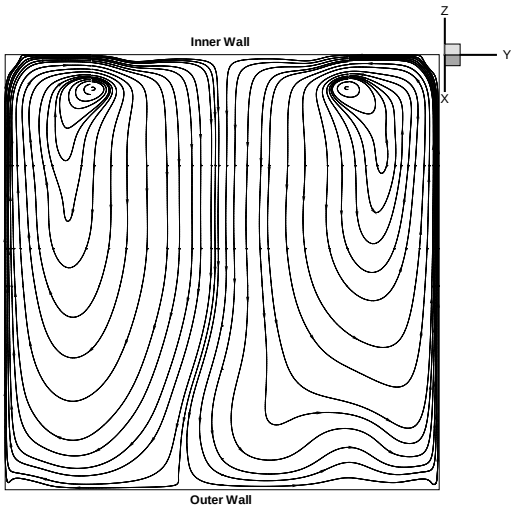

(a) $\theta = 45^o$

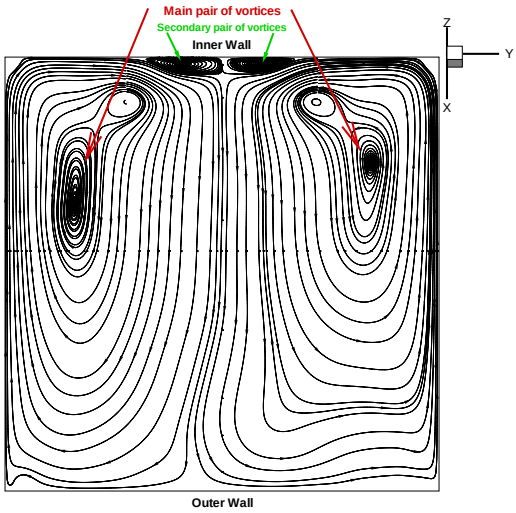

(b) $\theta = 60^o$

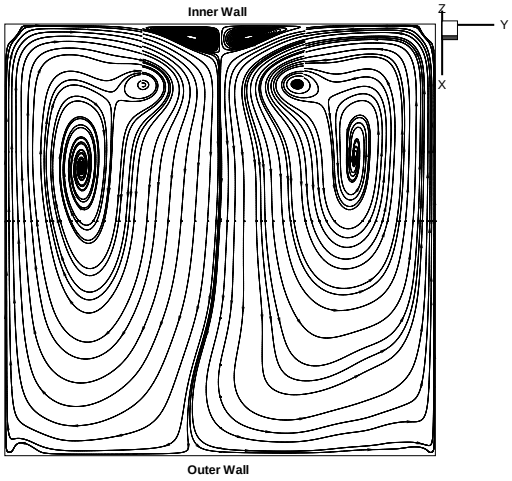

(c) $\theta = 75^o$

Figure 4.19: Streamlines along bend slices showing the counter rotating vortices (averaged field)

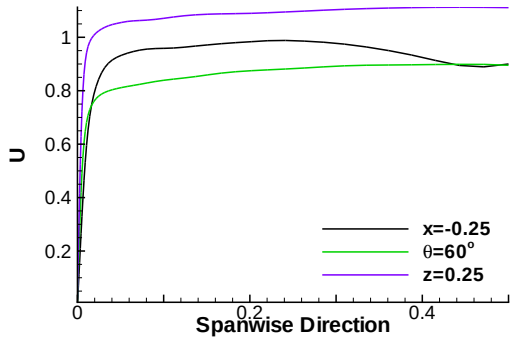

(a) D=0.1

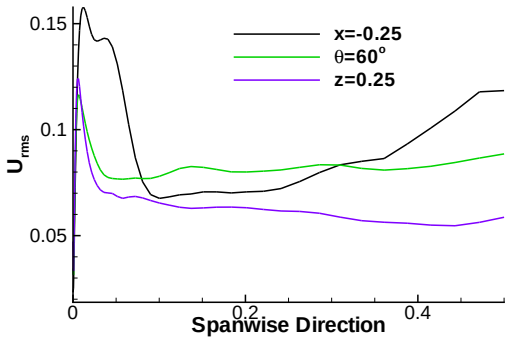

(b) D=0.1

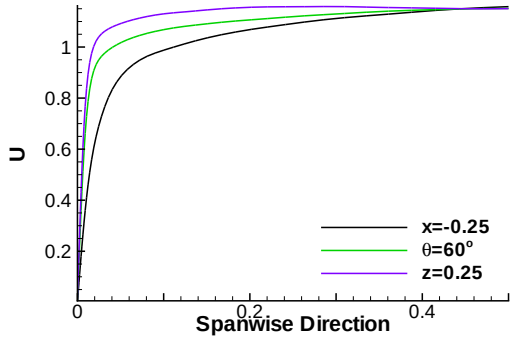

(c) D=0.5

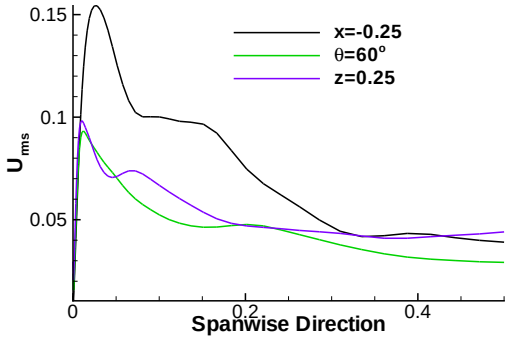

(d) D=0.5

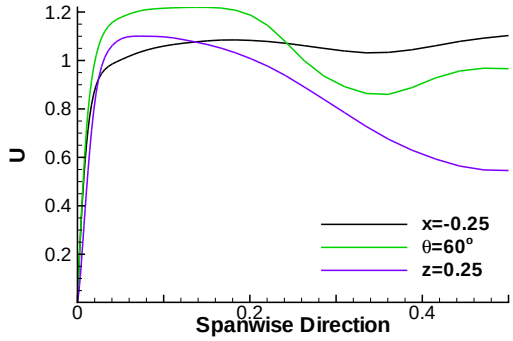

(e) D=0.9

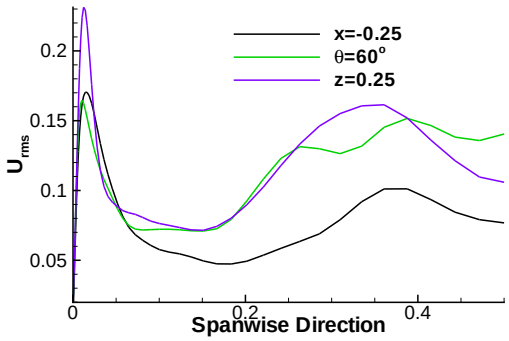

(f) D=0.9

Figure 4.20: Streamwise velocity and u_{rms} along the bend

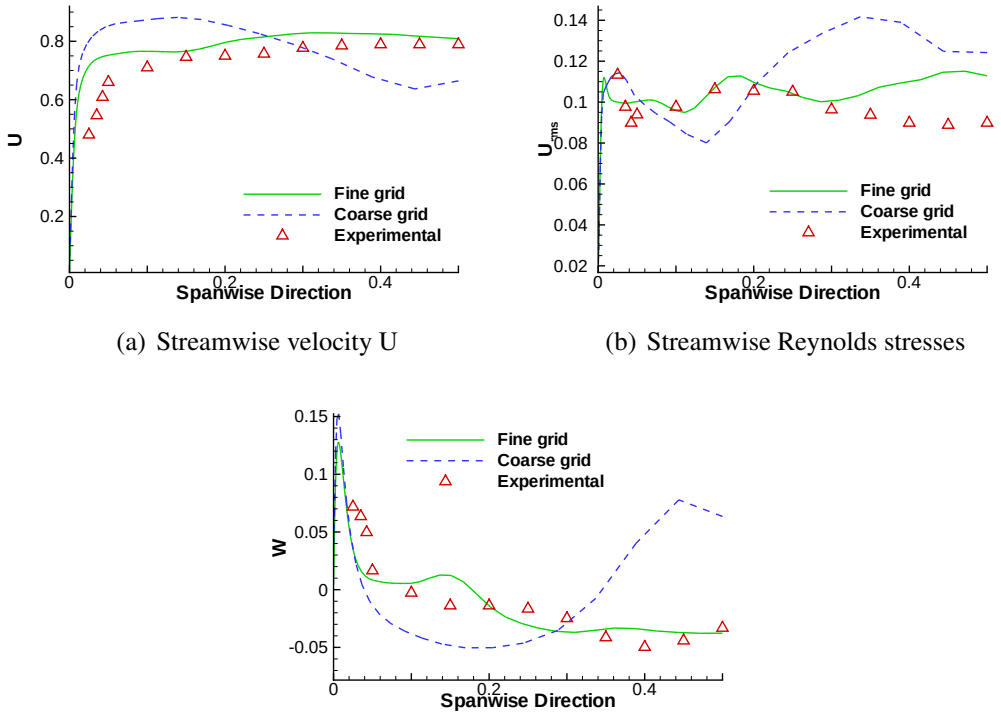

(a) Streamwise velocity U

(b) Streamwise Reynolds stresses

(c) Gapwise velocity W

Figure 4.21: Comparisons at $\theta = 30$ and $D = 0.1$

The WENO 9th scheme results will be used to represent the simulation data since that was the scheme presenting the best accuracy (as will be shown in the next subsection).

From the figures presented below along with all those presented in Appendix A and the the grid convergence study in the previous chapter many conclusions can be drawn as to the grid that provides the best results. In order to save computational resources only a coarse and fine grid were used for the simulations based on the grid comparisons of the previous chapter.

The first area of investigation (Figure 4.21) is at the start of the bend at an angle of 30^o where the streamwise and gapwise velocity, along with the streamwise turbulence intensity are being compared against experimental data. The sampling area is near the outer wall of the bend at a distance of 0.1 from it. In the streamwise velocity both grids overestimate the increase of its value near the wall since the value increases much faster than in the experiment. The same happens in the gapwise velocity and streamwise turbulence intensity mostly because of the possible error in the experiment to correctly capture the boundary layer. Besides the discrepancy in the near wall region though, the rest of the values pattern is covered correctly by the fine grid. Taking into account the error percentage provided by the experiment (around 3-4%) the agreement of the experimental and the simulation

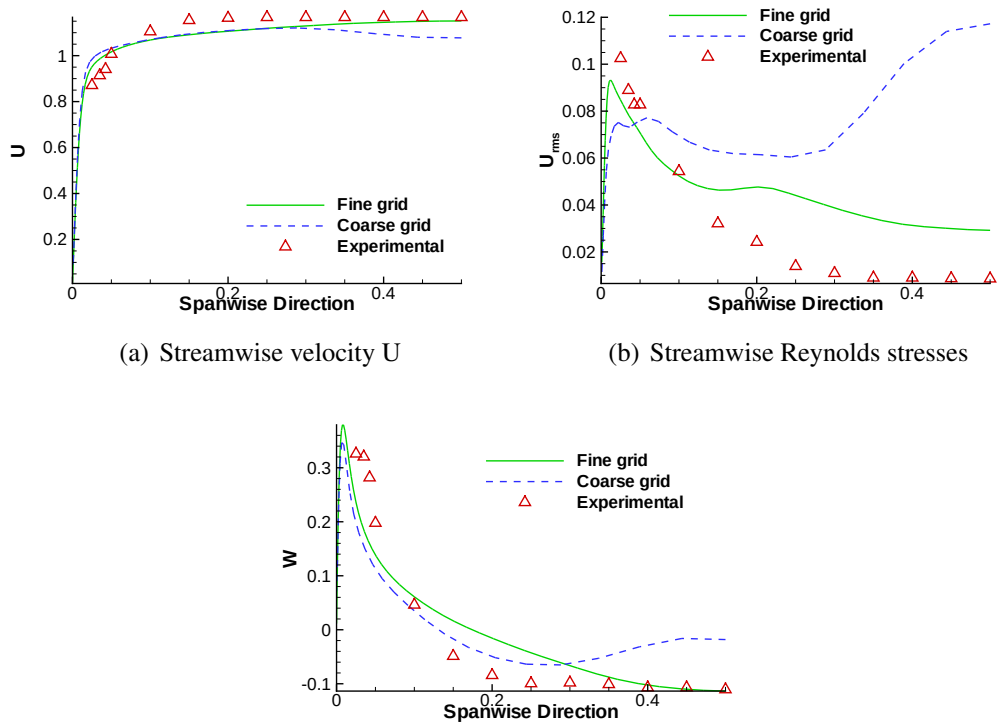

(a) Streamwise velocity U

(b) Streamwise Reynolds stresses

(c) Gapwise velocity W

Figure 4.22: Comparisons at $\theta = 60$ and $D = 0.5$

results for the fine grid is very good. The absence of detailed data near the wall for the experimental case makes the comparison closer to the wall difficult.

The next comparisons are presented in Figure 4.22, at $\theta = 60^o$, closer to the exit of the bend. The effects of the bend are really intense in this area and the correct capture of the flow is very important. The measurements are taken in the middle between the inner and outer walls of the bend. The fine grid results have a great agreement with the experimental data for the streamwise velocity while the coarse grid has great discrepancies as the measurements move closer to the middle of the geometry. There is an overestimation of the fine grid results for the turbulence intensity but the pattern is captured correctly along with the near wall region results. Here, it is made more obvious that the lack of good clustering in the coarse grid (especially away from the walls) is significantly influencing the accuracy of the simulations. Closer to the middle of the geometry, where the number of cells is small (especially for the coarse grid), the accuracy drops and even the results pattern has no agreement to the experimental data in the coarse grid. The gapwise velocity again confirms the overestimation of the top velocity near the wall region for both grids, the accuracy of the fine grid results and the discrepancies in the coarse grid near the middle of the geometry due to the small number of computational cells. Again though, the lack of experimental data closer to the wall makes comparisons in that region difficult.

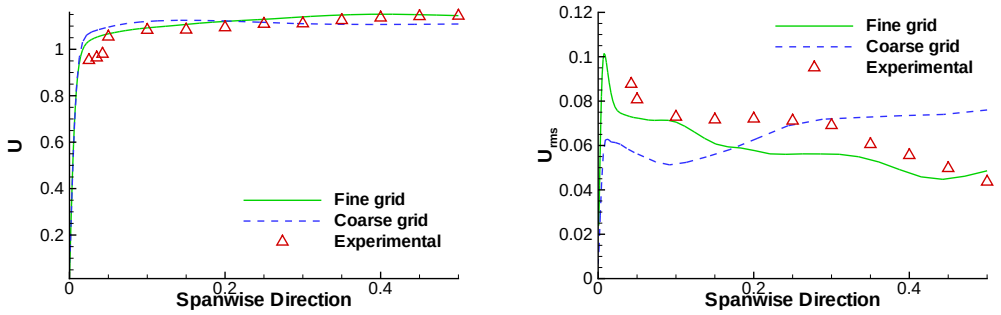

(a) Streamwise velocity U

(b) Streamwise Reynolds stresses

(c) Gapwise velocity W

Figure 4.23: Comparisons at $z = 0.25$ and $D = 0.3$

The final area for discussion is after the exit of the bend at $z = 0.25$. The influence of the bend area in the flow should be better obvious right after its exit and the accuracy of the results in this area is very important. In Figure 4.23 the results are extracted closer to the outer wall of the geometry. The observations made are again the same as the previous comparison areas. The fine grid still overestimates the values closer to the wall but is more accurate than the coarse grid and follows the profile very closely. The lack of sufficient grid points in the middle of the bend in the coarse grid is again obvious through the comparisons.

From the comparison of the simulation results with the data from the experiment in all areas, conclusions on the grid of choice can be made. The results presented in this section along with those in Appendix A show that in some areas the coarse and fine grid results are very close and in a few the coarse results can even be considered better. Taking all the results into account though and especially in the areas of great flow physics phenomena, for this case, the fine grid results present a high accuracy while the coarse grid ones have significant discrepancies in most of the comparisons. The lack of a sufficient number of points in the middle of the coarse grid lowers the accuracy of the method significantly and the results produced can not , under any circumstance, be used for further analysis and study. So this, along with the grid comparisons of the previous chapter, is why the fine grid results are the ones used for any flow analysis and scheme comparisons.

4.3.3 Numerical scheme effect

The next step in the evaluation of the simulations conducted is the comparison of the different schemes employed. Choosing the best scheme is imperative in understanding the flow physics and evaluating the effectiveness of the different schemes used (for this and similar cases) and for any future research on the same or similar geometries. Although the differences are smaller than expected between the different grid sizes the finer grid provides the best results especially in areas of intense importance like the near wall regions, thus all the comparisons are performed using the results obtained from the fine grid.

The comparison areas include the area before the entrance of the bend, three areas in the bend at different angles and the area right at the exit of the bend. The amount of data again is such that can not be presented on its whole so it will be presented for all areas in Appendix B and only enough here to provide the basis for the analysis and discussion. The data comparison areas can again be seen in Figure 4.7.

In Figure 4.24 the streamwise velocity and turbulence intensity are shown for the area near the outer wall, from the entrance to the exit of the bend. All three schemes capture u velocity the same way with MUSCL 5th presenting some discrepancies inside the bend compared to the other two methods. In the entrance and inside the bend the flow in the simulations accelerated closer to the wall compared to the experiment. The turbulence intensity u_{rms} though presents the differences between the schemes. In the entrance of the bend MUSCL 5th and WENO 9th capture the near wall region but present discrepancies

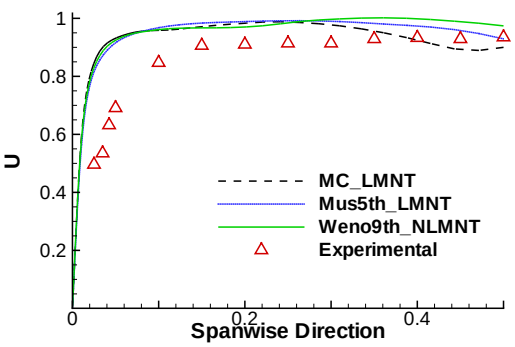

(a) x=-0.25 and D=0.1

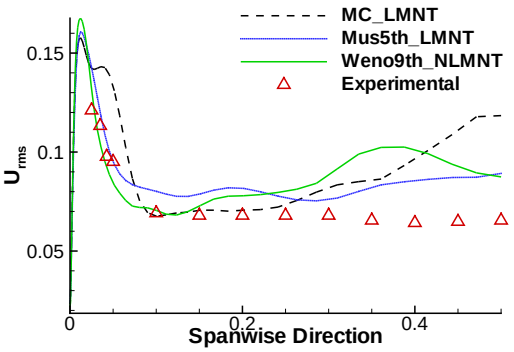

(b) x=-0.25 and D=0.1

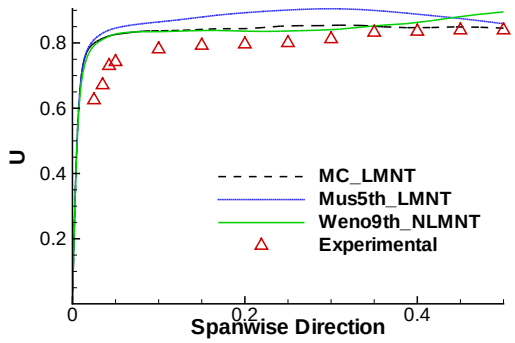

(c) $\theta = 60^o$ and D=0.1

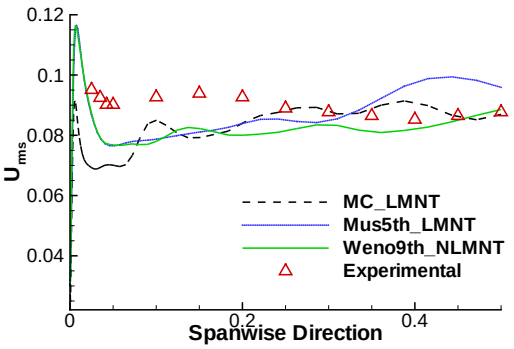

(d) $\theta = 60^o$ and D=0.1

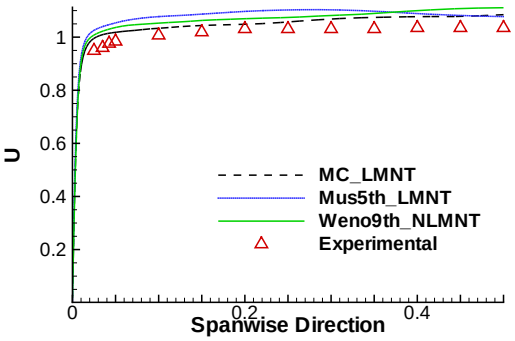

(e) z=0.25 and D=0.1

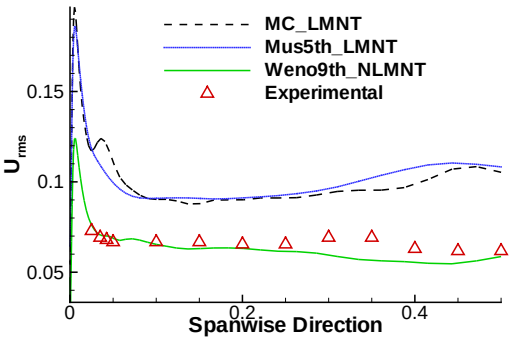

(f) z=0.25 and D=0.1

Figure 4.24: Streamwise velocity and u_{rms} scheme comparisons close to the outer wall

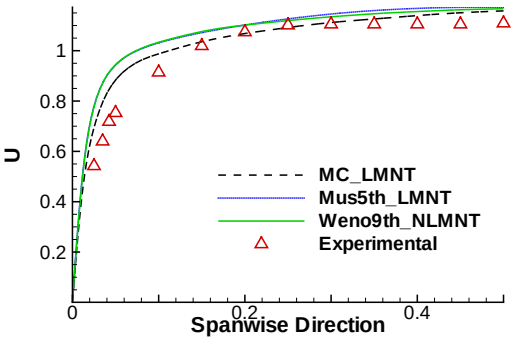

(a) x=-0.25 and D=0.5

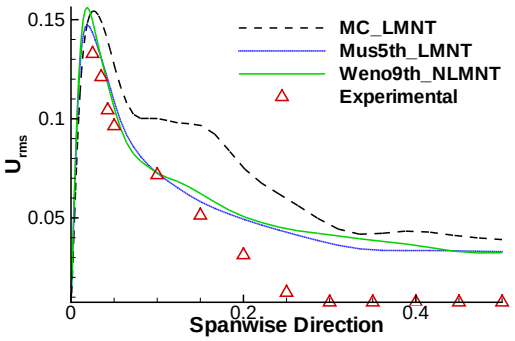

(b) x=-0.25 and D=0.5

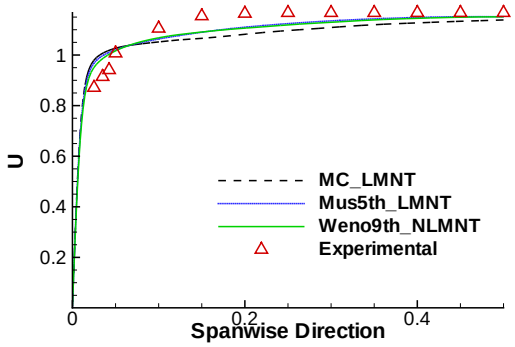

(c) $\theta = 60^o$ and D=0.5

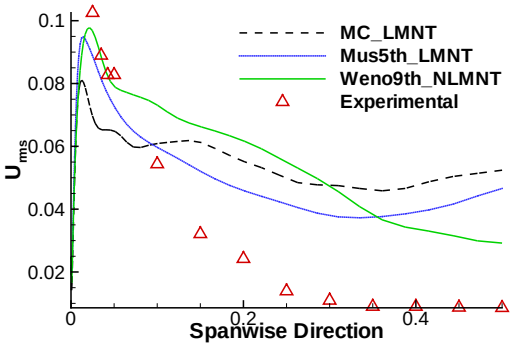

(d) $\theta = 60^o$ and D=0.5

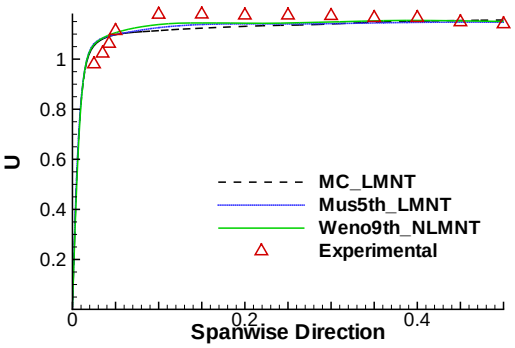

(e) z=0.25 and D=0.5

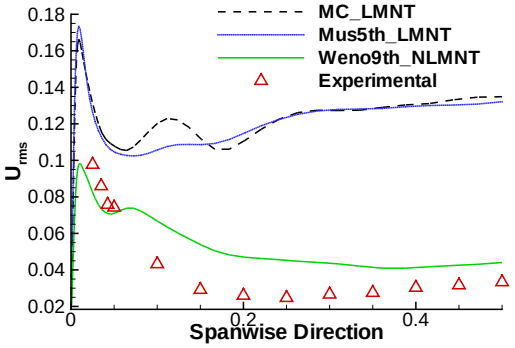

(f) z=0.25 and D=0.5

Figure 4.25: Streamwise velocity and u_{rms} scheme comparisons in middle of the flow

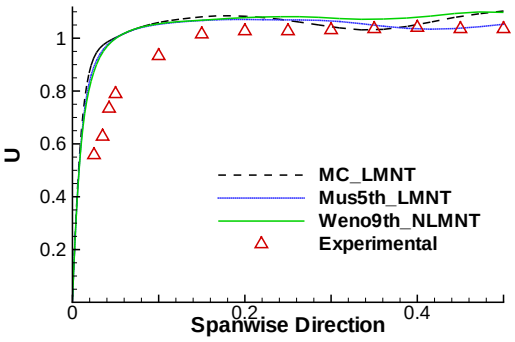

(a) x=-0.25 and D=0.9

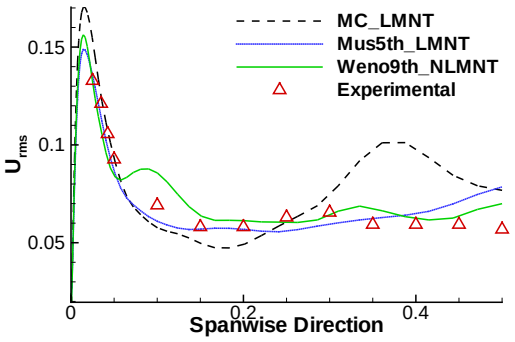

(b) x=-0.25 and D=0.9

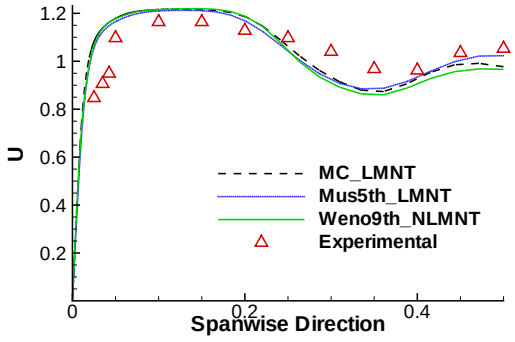

(c) $\theta = 60^o$ and D=0.9

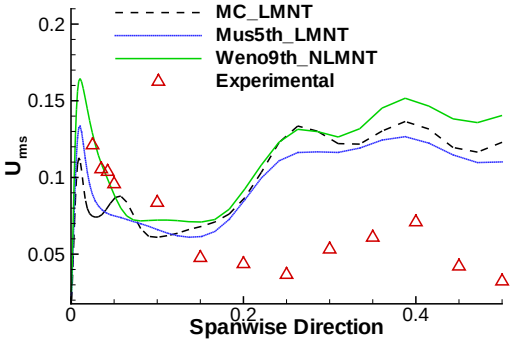

(d) $\theta = 60^o$ and D=0.9

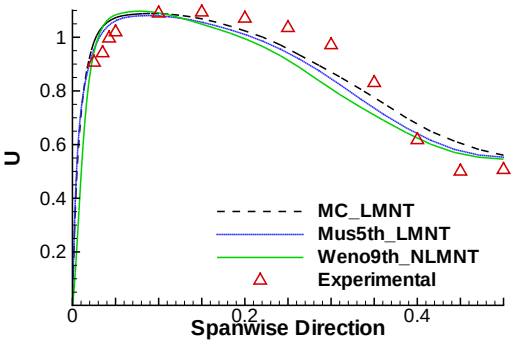

(e) z=0.25 and D=0.9

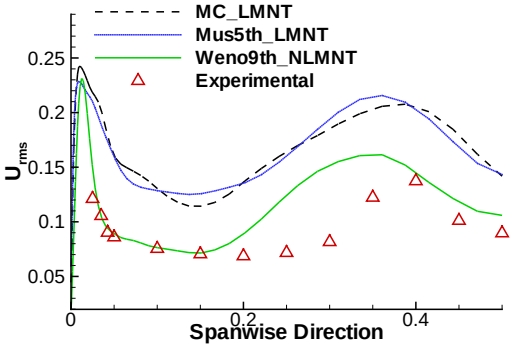

(f) z=0.25 and D=0.9

Figure 4.26: Streamwise velocity and u_{rms} scheme comparisons close to the inner wall

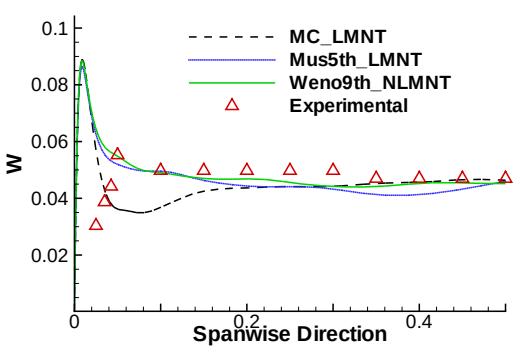

(a) x=-0.25 and D=0.5

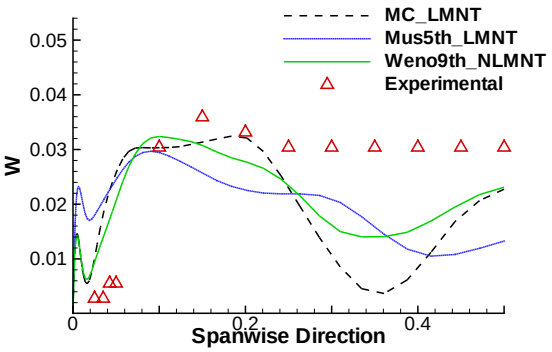

(b) x=-0.25 and D=0.9

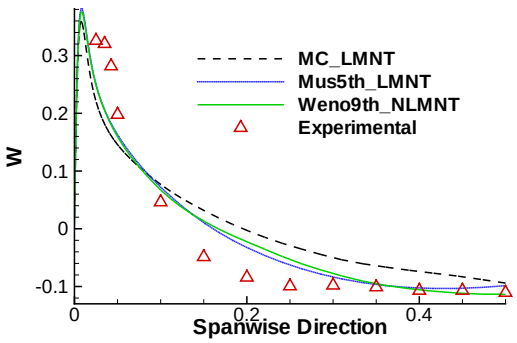

(c) θ = 60^o and D=0.5

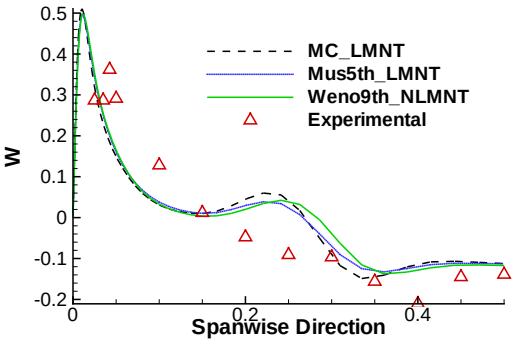

(d) θ = 60^o and D=0.9

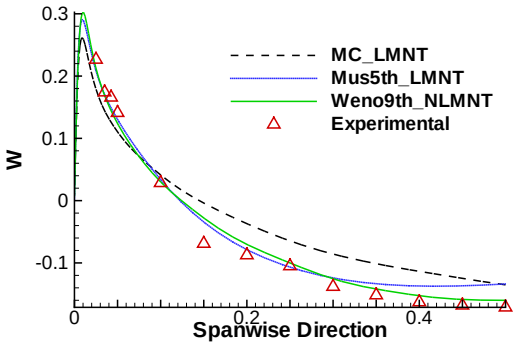

(e) z=0.25 and D=0.5

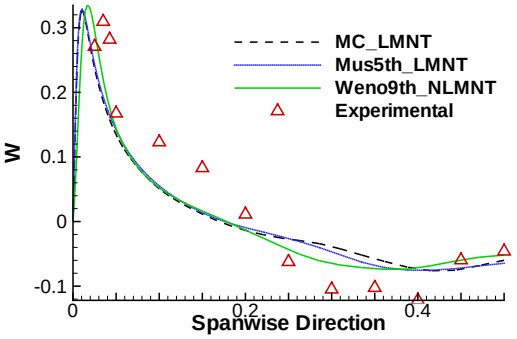

(f) z=0.25 and D=0.9

Figure 4.27: Gapwise Velocity at the middle of the flow and close to the inner wall

closer to the symmetry area of the domain. This could be attributed to an earlier formation of the outer wall vortices in the simulations compared to the experiment. Inside the bend, MC is the only scheme presenting significant differences to the experimental data but once the exit is reached it is made obvious that the capture of turbulence intencity by MUSCL 5th and MC is overestimated when WENO 9th captures it accurately.

Moving towards the centre of the flow in Figure 4.25 the same remarks can be made about the streamwise velocity where all schemes present almost identical results and the near side wall region is better captured by all schemes, compared to the outer wall region. For the turbulence intensity there are some discrepancies at the entrance and inside the bend with MUSCL 5th and WENO 9th capturing the near wall values more accurately than MC with an overestimation though closer to the symmetry area. Again after the influence of the bend on the flow and by looking at the results at the exit only WENO 9th manages to capture the correct magnitude while the other methods widely overestimate the intensity.

The area with the most intense phenomena is that of the inner wall where the counter rotating vortices are formed. The data comparisons for that area are shown in Figure 4.26. The streamwise velocity is captured accurately by all schemes with MUSCL 5th probably presenting slightly better results. At the entrance and inside the bend the same discrepancies at the near wall region are seen as in the outer wall comparisons. Since these are seen both in the inner and outer wall regions they can be attributed to a possible experimental error. In their experiments Taylor et. al. [107] claimed that the secondary motion (from the straight part of the duct) influencing the boundary until the mid of the bend was not accurately captured. Considering that the secondary flow is located near the corners the influence in the values near the inner and outer walls and close to the side walls can be significant. This is probably why the observed discrepancies are higher at the entrance, lower inside the bend and disappear at the exit. Finally looking into the results for the turbulence intensity u_{rms} the same observations as before are made with WENO 9th capturing the profile better especially at the exit of the bend and with some discrepancies for all methods at the locations influenced by the counter rotating vortices.

The final comparisons are made at the areas in the middle of the flow and near the inner wall for the gapwise velocity w, Figure 4.27. At $D = 0.5$ with the exception of the near side wall region at the entrance of the bend all schemes produce almost the same results with WENO 9th having a slightly better accuracy with almost no discrepancies towards the experimental data. Inside the bend though where the flow phenomena are intense there are discrepancies from all the methods especially at the entrance of the bend. Inside the bend and at the exit WENO 9th again presents the best capture of the flow based on that of the experiment.

As a result, from the analysis of the comparison plots above including those in Appendix B, some conclusions and remarks can be drawn. In some of the areas inside the domain all three schemes present almost the same results with small differences but with MUSCL 5th and WENO 9th presenting the highest accuracy compared to the experimental data available. In some cases it is even difficult to choose between the two schemes. While

the comparisons reached the end of the bend and its exit though, the choice of the best simulation set-up was made obvious. WENO 9th presented a high accuracy in the majority of the comparisons performed. The areas sampled and compared towards experimental data were more than enough to allow a safe and fair conclusion as to the accuracy of the scheme. Besides some discrepancies that were expected because of the complexity of the flow and the pre-existing error in the experimental measurements WENO 9th presented a well resolved case. It is safe to say that the fine grid, with WENO 9th as the scheme employed, provided an accurate validation of the simulations performed so a flow analysis on this case would provide important information on such a complex turbulent flow that would not be possible in detail from the experiments alone.

For the turbulence intensity, although there were some oscillations in the solution, causing slight discrepancies towards the experimental data, the results for WENO 9th were still within an acceptable margin of error. WENO 9th introduces a lower numerical dissipation itself, compared to the other schemes, thus capturing the turbulent flow better even without the assistance of a technique like LMNT.

The influence of LMNT in the schemes employing it is also very interesting. It can be observed that LMNT significantly assists the MC and MUSCL 5th schemes to better perform and keep the accuracy very close to that of the WENO 9th in many areas of the domain. The problem though is that in many areas it overestimates the turbulence, compared to the experimental data. This can be made more obvious in the turbulence intensity where the two methods that use LMNT overestimate the values widely. So although WENO 9th was expected to produce the lowest numerical dissipation than the other two methods the opposite happened because of the influence LMNT introduced. The most interesting observation though is that LMNT assisted MUSCL 5th and MC in providing an accurate capture of the turbulent flow for the straight duct (that was presented in the previous chapter) and until the mid area of the bend. After the flow started becoming more complex though, because of the effects of the bend, the schemes employing LMNT started producing overturbulent results. Overall from what was expected concerning the performance of the schemes both MUSCL schemes performed very well with the help of LMNT but still could not outperform WENO 9th.

The above observations can be further justified and analysed by looking into some iso-surfaces, contour comparisons, the energy spectra and the high order statistics that follow. Vorticity magnitude iso-surfaces of a low value can provide important information on the development of turbulence inside the bend as well as the capture of the small scales by the scheme. Figures 4.28 to 4.30 show the vorticity magnitude iso-surface at a low value of 0.5 in the bend area, including part of the entrance and outflow (instantaneous results were used to capture small scales). From these figures the schemes are proved capable of resolving 3D turbulent structures. MUSCL 5th and MC provide a more turbulent solution since smaller scales are captured compared to WENO 9th. Although the differences between MUSCL 5th and MC are hardly visible in the figures, the maximum and minimum values of vorticity were of higher magnitude for the MUSCL 5th scheme. The biggest differences are seen at the exit area of the bend where these two methods show a more turbulent flow

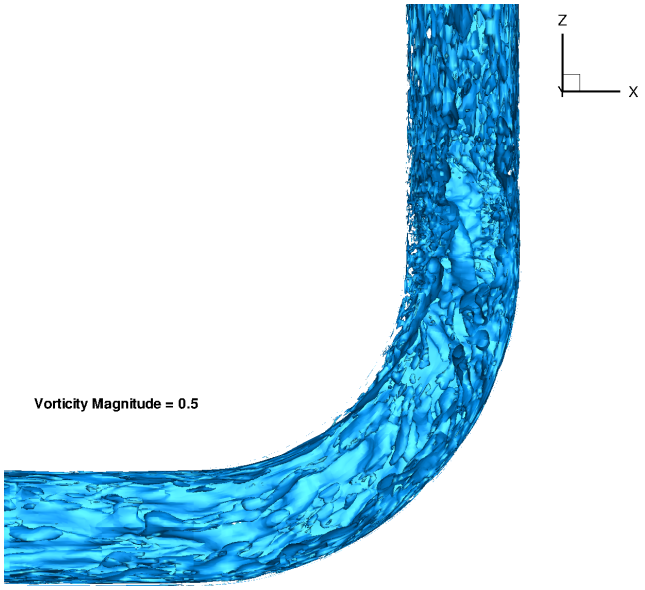

Figure 4.28: Vorticity Magnitude iso-surfaces for MUSCL 2nd order MC with LMNT (t^*=969)

compared to the WENO 9th scheme. Based on the comparisons with the experimental data, the bigger discrepancies of MUSCL 5th and MC schemes are noticed in that area while WENO 9th is capturing the flow correctly proving it to be the method providing the correct turbulence magnitude in that area. It is made clear here that LMNT affected the solution significantly after the bend, leading to an overestimation of turbulence from the two methods that employed it.

Looking at the vorticity magnitude contours for small scales at the entrance, inside the bend and at the exit for all three schemes presented in Figures 4.31 to 4.33 further observations can be made. At the entrance of the bend all three schemes capture the small scales of vorticity almost in the same areas and at the same intensity something that comes in direct agreement to the numerical comparisons presented before. While moving inside the bend, although the area near the inner wall where the vortices have formed is captured in almost the same way by all three schemes, MC and MUSCL 5th schemes present some intense vorticity areas near the outer wall that are not as present in the WENO 9th case. Finally at the exit of the bend the observations about an overestimation of the turbulence by MC and MUSCL 5th is made clear especially in the near wall regions both inner and outer. Both the iso-surfaces and the vorticity magnitude vortices are derived from instantaneous results so that small scales are better visible.

Similar conclusions can be derived by studying the power spectra for all schemes at different areas. Point-wise data along time were collected in many areas of the domain. Here, the changes of u velocity over time were used to calculate the power spectra as well as the skewness and flatness that will be presented later. The areas of data collection (markers) were at the entrance of the bend, at 60^o inside the bend and at the exit. In all cases the data were extracted from the middle of the domain as shown in Figure 4.34. The

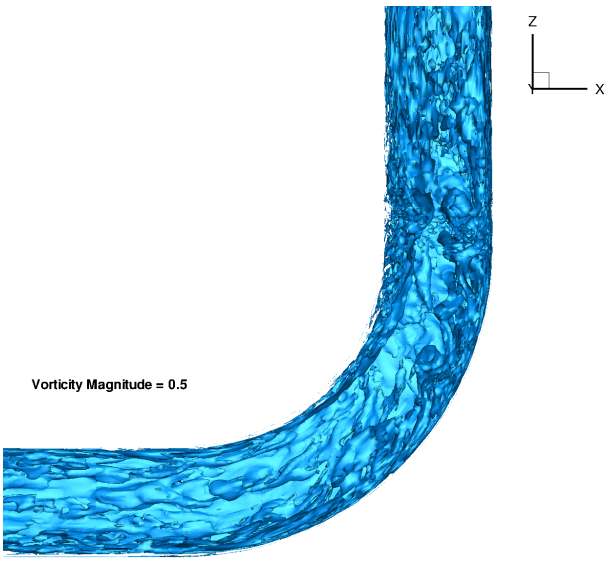

Figure 4.29: Vorticity Magnitude iso-surfaces for MUSCL 5th order with LMNT (t^*=969)

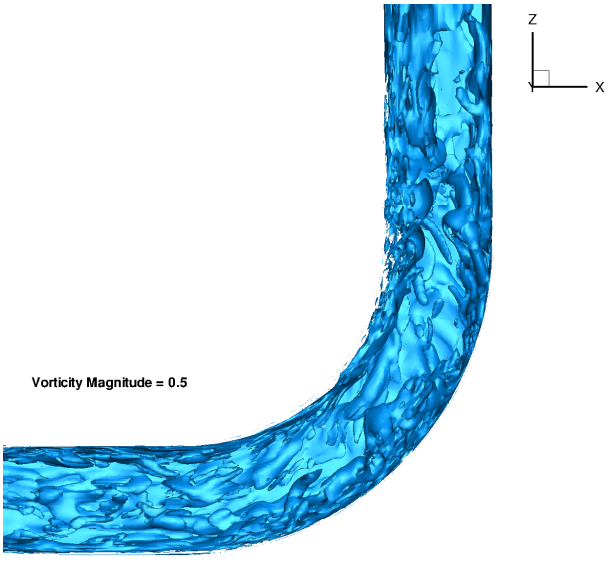

Figure 4.30: Vorticity Magnitude iso-surfaces for WENO 9th order without LMNT (t^*=969)

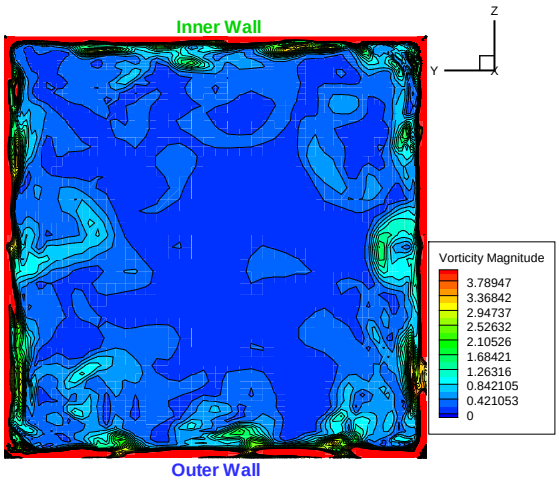

(a) MC

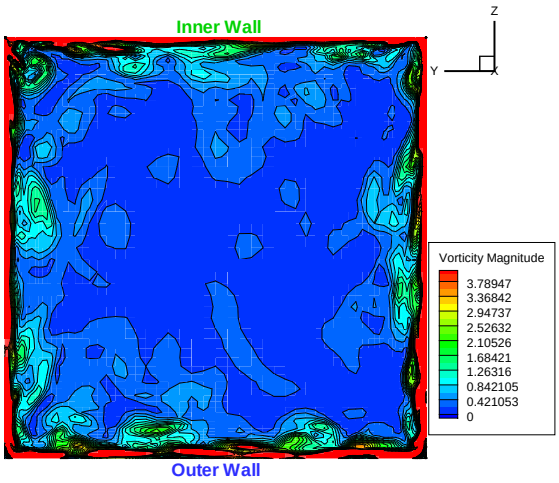

(b) MUSCL 5th

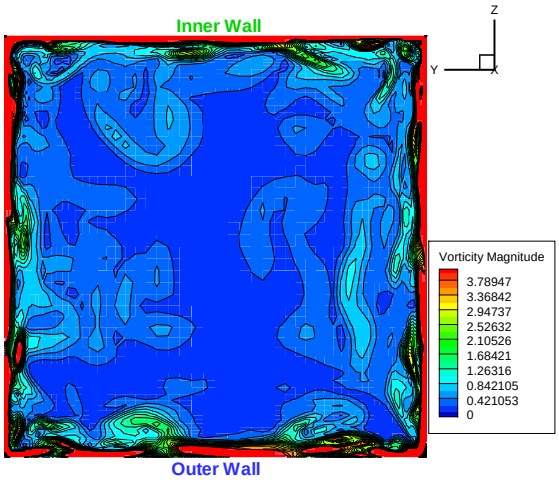

(c) WENO 9th

Figure 4.31: Vorticity magnitude at $x = -0.25$ (t^*=969)

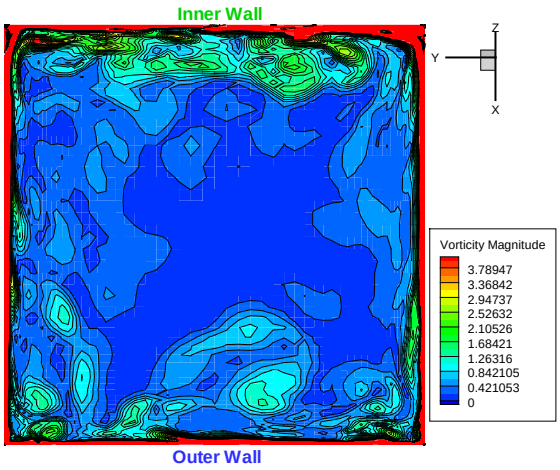

(a) MC

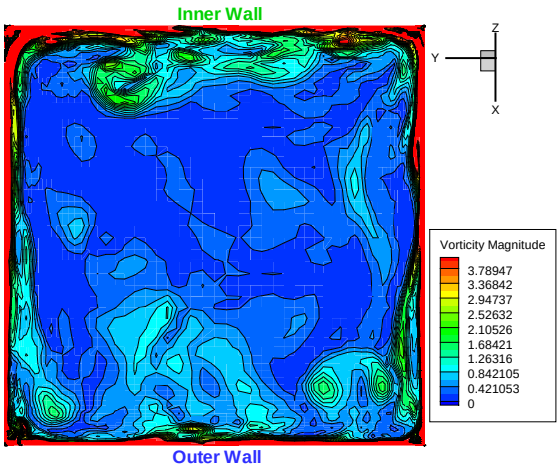

(b) MUSCL 5th

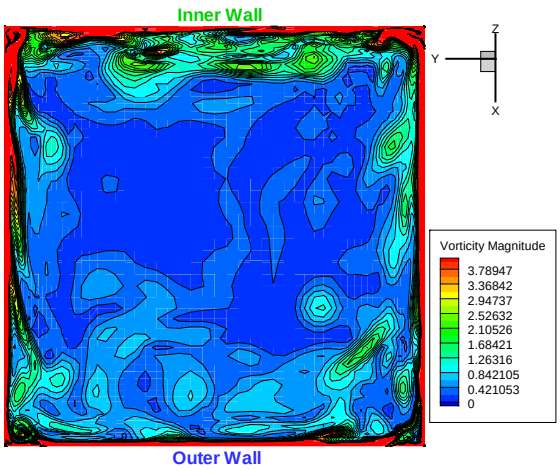

(c) WENO 9th

Figure 4.32: Vorticity magnitude at $\theta = 60^o$ (t^*=969)

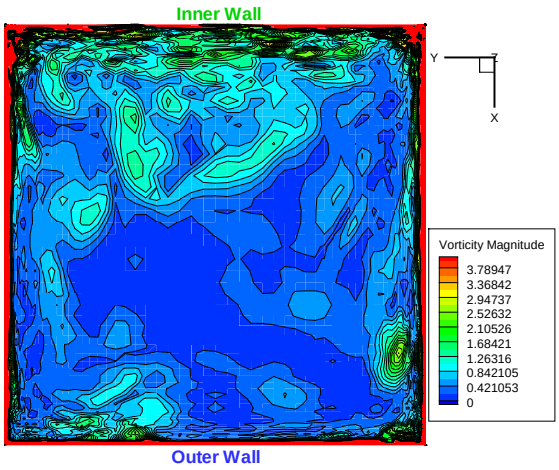

(a) MC

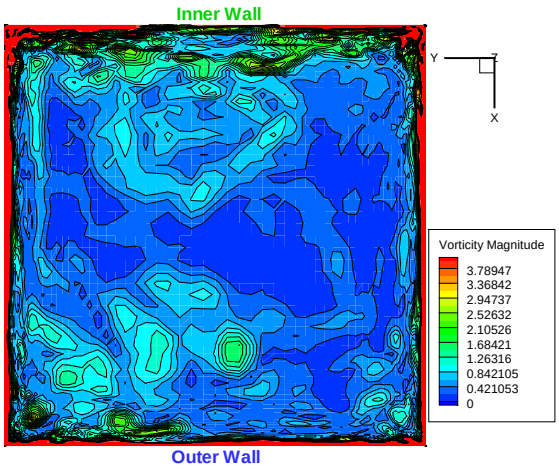

(b) MUSCL 5th

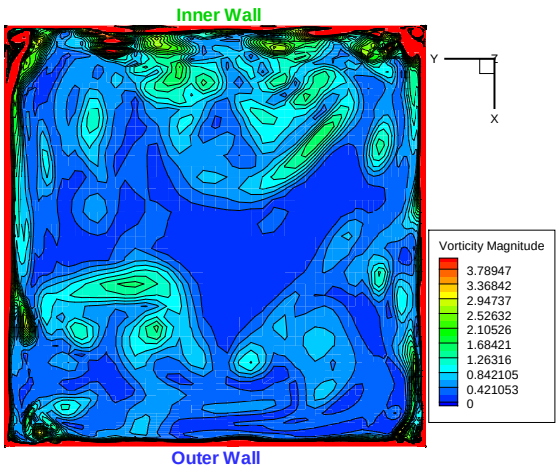

(c) WENO 9th

Figure 4.33: Vorticity magnitude at z = 0.25 (t*=969)

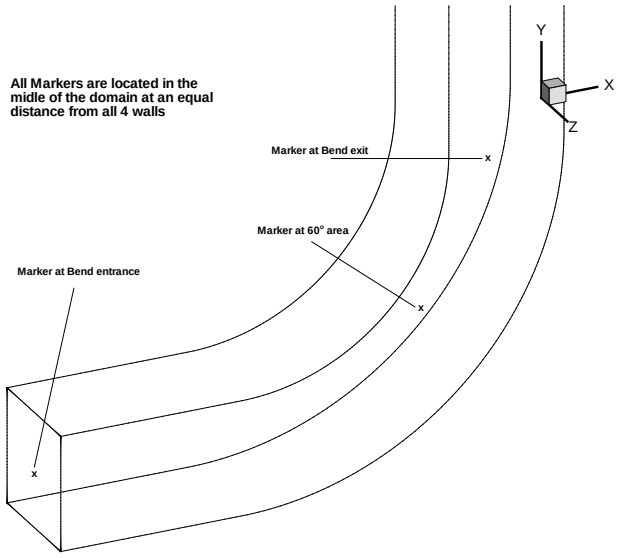

Figure 4.34: Data collection marker's location

results obtained from the centre of the straight duct, presented in the previous chapter, will be shown in the comparisons here as well, since it will provide a better view on how the developed turbulent flow reaching the bend is influenced by its effect.

Although the flow inside the L-bend duct is not a periodic one, spectra, skewness and flatness can still provide important information. Similar measurements were used in other studies as well, like the one by Prasad et al. [110] for a lid-driven cavity. Table 4.2 presents the slopes derived from the power spectra for all markers at all schemes compared to that of Kolmogorov [104]. Based on the numbers presented in the table, the very turbulent nature of the solution provided by MUSCL 5th and MC is shown again. In all three schemes the flow is developed into a turbulent state in the straight duct at almost the same magnitude. The flow enters the L-bend and reaches the bend entrance almost at the same state but once it enters, the differences between the schemes start appearing. While there is a gradual decrease in the turbulence intensity, based on the experimental results, the slope for MC and MUSCL 5th remain almost the same inside the bend and at its exit (as was also shown in Figures 4.28 and 4.29), while the slope for WENO 9th gradually increases (in absolute value) compared to the Kolmogorov one. The reasons for the discrepancies between the simulation acquired slopes and that of Kolmogorov can again be attributed to the same reasons analysed in chapter 3. In total, the results here show (as expected because of the geometry and the nature of the flow) that this is not a homogeneous turbulent flow but although the slopes are not equal to Kolmogorov's $-\frac{5}{3}$ they are close enough for the areas where the flow presents a near homogeneous state.

Finally through Figures 4.35 and 4.36, where the skewness and flatness for the WENO 9th scheme in all three L-bend marker areas is presented, the statistical convergence in all

	straight duct	bend entrance	bend at 60^o	bend exit
MC	-2	-2.22	-2.1	-2.1
MUSCL 5th	-2	-1.99	-2.1	-2
WENO 9th	-1.99	-2.37	-3.4	-4.3
Kolmogorov	-1.667			

Table 4.2: Power spectra slopes for all schemes

areas is shown. The skewness and flatness are shown over time inside the averaging window and are point-wise quantities. After some time the fluctuations of the value are insignificant proving that the statistical convergence of the averaged data used in the previous sections. The high order statistics for the MC and MUSCL 5th schemes presented similar results.

4.3.4 Conclusions

The turbulent flow inside a 90^o bend was studied using ILES. Two different grids and three different schemes were studied and tested for the accuracy of the produced results. Finally all the produced data was processed and analysed.

The data obtained and presented in this chapter around the study of the flow in a 90^o bend finally provided us with many and interesting observations and conclusions. Initially the computational method used and the set-up of the problem were successfully validated towards experimental data. This procedure made the validity of the comments that followed the study of the flow possible. The results of the analysis can be divided in two categories. The first one concerns observations of certain flow characteristics of a turbulent flow inside a duct with a bend. The second one is the analysis of the different schemes employed along with the influence of the Low Mach Number Treatment technique.

In the L-bend the flow enters the bend in a uniform way but flow accelerates along the inner part of the bend up to an angle of 50^o when it starts to decelerate. This phenomena, based on the centrifugal force, causes an opposite effect on the pressure where the pressure drops in the inner part while it rises in the outer. The flow regains its uniformity gradually after exiting the bend. Inside the bend there are two counter rotating secondary vortices, that lead the flow from the inside of the duct closer to the outside wall, induced by the curvature. Another interesting point is the possible confirmation of an observation made by Taylor et al. [30, 107]. In their research they were worried that the streamwise secondary flows that influence the flow significantly until around 40^o inside the bend were not correctly captured by the boundary layer they used. The slight discrepancies in this area could be possibly justified by a better capture of the secondary motion in the streamwise direction at the entrance of the bend in the computational set-up used. In the simulations conducted here, two extra pairs of counter rotating vortices appeared inside the bend and close to the inner wall that where not presented in the experiment. One might assume that these were

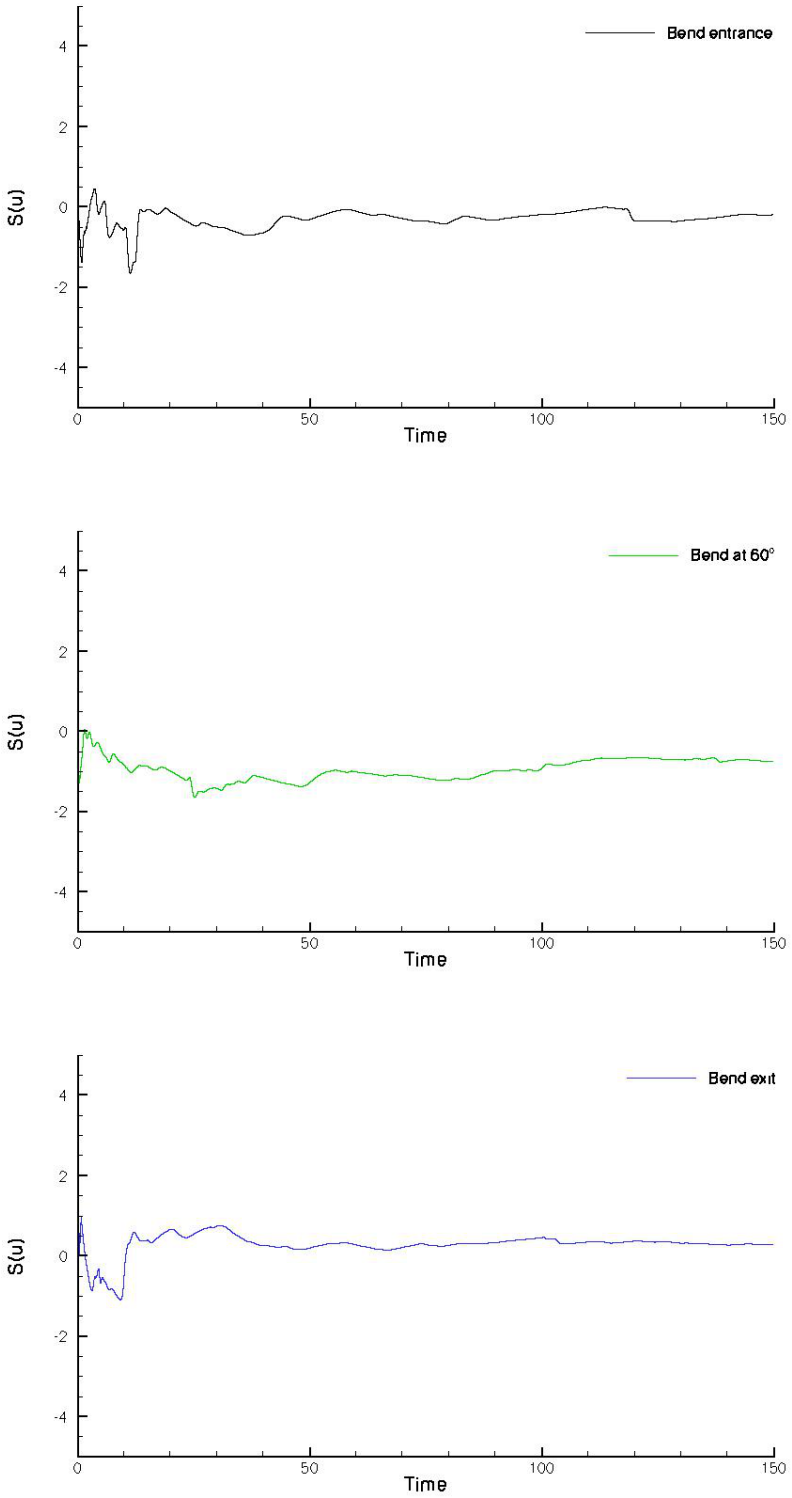

Figure 4.35: Skewness for WENO 9th scheme

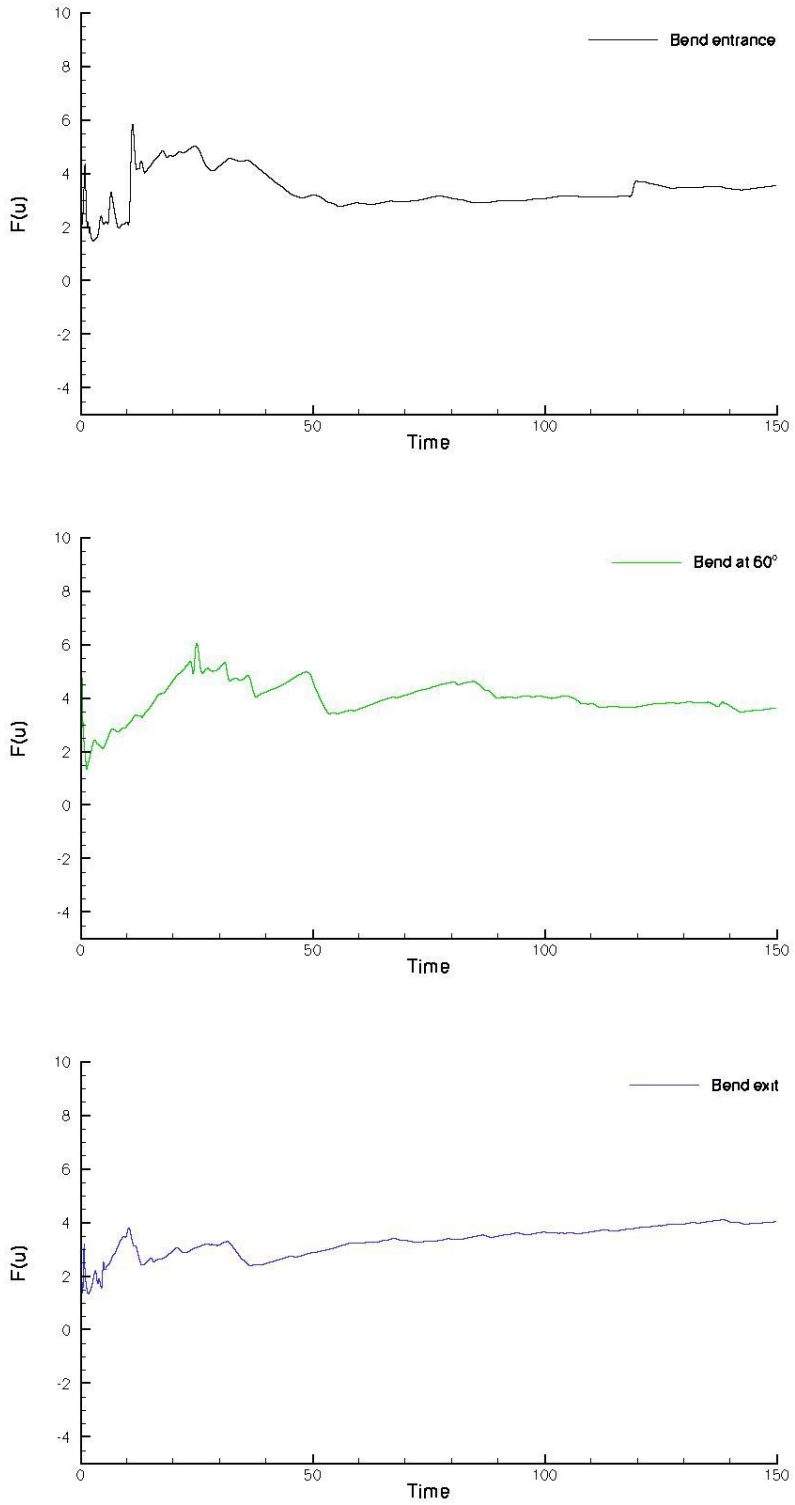

Figure 4.36: Flatness for WENO 9th scheme

not observed experimentally because of lack of resolution and not observed in RANS because of excessive dissipation. On the other hand it is possible that these vortices are an artefact in the ILES simulations. It is not possible to assert one or the other conclusion at present stage without a detailed experimental study designed to either prove or disprove the existence of these structures.

Finally the comparison of the different schemes used resulted in the WENO 9th outperforming MC and MUSCL 5th providing more accurate results. As the comparisons moved to areas of more intense turbulent flow, where secondary flows were in motion, WENO 9th seemed to function much better than the other schemes. The Low Mach Number Treatment function employed for two of the schemes seemed to help in the development of a turbulent flow in all grids but a negative side was that it lead to the overprediction of turbulence in most of the areas. As a result WENO 9th without LMNT in a fine grid seems to be the set-up that performs better, producing accurate results and capturing the flow characteristics in geometries of this kind.

CHAPTER 5

Conclusions and Future Work

The turbulent flow inside a straight duct and a duct with a 90^o bend were studied using Implicit Large Eddy Simulation. Several high order schemes were used with the assistance of LMNT for some of the cases. The first case studied was that of the straight duct. The existence of four walls and corners in the geometry caused the generation of stress induced secondary motion. Counter rotating vortices were generated near the corners showing the existence of secondary flows that travelled in the streamwise direction in a swirling motion. The presence of the corners presented the flow with its differences to a channel one. The boundary layer in the duct was thicker than that of the channel causing lower velocities near the wall but higher turbulence intensity values on the streamwise direction. MUSCL 2nd MC with LMNT, MUSCL 5th with LMNT and WENO 9th without LMNT presented an almost similar turbulent flow that could be used as the incoming flow for the L-bend case.

The next case, which was the L-bend duct, was coupled with the straight duct and was using the produced turbulent flow as an inflow. The same schemes were used and their results were compared towards experimental data. The flow entered the bend in a uniform way but then accelerated along the inner part of the bend up to an angle of 50^o before it started decelerating. The pressure dropped in the inner part while it rose in the outer. The flow regained its uniformity gradually after exiting the bend. Inside the bend there were two main counter rotating secondary vortices transferring the flow from the inside of the duct closer to the outside wall, a phenomenon induced by the curvature. Two more counter rotating vortices were also observed very close to the inner wall and the symmetry area of the bend.

An extra pair of vortices was observed in the simulation results at around 45^o while this was remarkably not observed or mentioned in either the experiment of the RANS simulations available. Although in the experiment it is mentioned that they were worried that the streamwise secondary flows that influence the flow up to that point may not be correctly captured (that could explain the extra pair of vortices in the simulations) the extra vortices can not be considered a "confirmed" flow characteristic. The magnitude of these secondary

vortices as well as the corresponding values of gapwise velocity inducing this flow are quite small. One might put forward a proposition that these were not observed experimentally because of lack of resolution and not observed in RANS because of excessive dissipation. On the other hand it is possible that these vortices are an artefact in the ILES simulations because of the fine grid and insufficient dissipation. It is not possible to assert one or the other conclusion at present stage without a detailed experimental study designed to either prove or disprove the existence of these structures. So this find can trigger a future, more detailed, study and analysis of this phenomena not only in an ILES context.

The comparison of the different schemes showed that WENO 9th outperformed MC and MUSCL 5th providing more accurate results. As the comparisons moved to areas of more intense phenomena, where secondary flows were in motion, WENO 9th seemed to function much better than the other schemes. The Low Mach Number Treatment function, employed for two of the schemes, seemed to assist in the development of a turbulent flow in all grids but ended up leading to an overprediction of turbulence in most of the areas. As a result WENO 9th without LMNT in a fine grid outperformed the rest, producing accurate results and capturing the flow characteristics of the case. So overall LMNT was a very helpful tool in providing lower dissipation for the two schemes employing it in the straight part of the duct. As the flow went through the bend, where the flow became more complex, the schemes using it ended up overestimating the turbulence compared to the experimental data.

The results and their validation showed the accuracy for the state of the art methods used. Although no turbulence models where used and less computational resources than in LES where utilised the turbulence was captured and satisfactory results were provided. This is one more case proving the importance and future of high-order, high-resolution methods in ILES but there is still a lot of future work needed in the area.

The study of the LMNT effect on the schemes employing it provided us with some very important and interesting results. The overestimation of turbulence is mostly noticed in the area after the middle of the bend and while progressing towards the outflow. Finding the reason for this is a hugely challenging task since too many state of the art methods are being used together and locating an exact reason would be close to impossible. There is an important assumption that can be made though and would offer for future studies in this area and LMNT. The flow after the middle of the bend starts dropping in velocity forming larger areas of uniformly low speed. This has as an effect low Mach numbers in the area that with its turn leads to a more active use of LMNT in the simulation. The higher weights in the LMNT technique could lead to a significant amount of dissipation being removed that in the end produce the highly turbulent results observed. Further study in the reasons for these discrepancies and on the way LMNT works, in the future, can provide a very helpful tool for ILES. This further illustrates observations made previously by Kokkinakis [1] for the turbulence resolution in a plane channel case. The main challenge so far in ILES schemes was associated with the dissipative error being too high and turbulence being under-predicted. However as demonstrated in this study, combining high resolution schemes with additional dissipation control provided by LMNT may in some cases lead

to insufficient dissipation with the over-predicted rather than under-predicted turbulence levels, while maintaining the overall stability and convergence of the numerical solution. These observations lead to the question of what is "adequate" in terms of dissipative error for ILES, which opens multiple opportunities for future research.

As this set-up successfully captured the flow inside a duct with a 90^o bend more complicated geometries can be studied in the future for the method to be further evaluated. Geometries like U-bends, S-bends or even L-bends with a steeper turn could be studied. The effect of different Reynolds numbers could also offer important information on duct flows.

On the numerical aspect, the acquired data and observations could be used to further improve some aspects of the methods employed. A more detailed study of the Low Mach Number Treatment technique could lead to its improvement and deal with the issues of overpredicting turbulence in cases like the one studied here. More data for this improvement could be provided by studying the same case using MC and MUSCL without LMNT so that the differences between employing LMNT and simulating without it can be located. The computational cost of the simulations was too high for this study to be included here.

Bibliography

[1] I. W. Kokkinakis. *Investigation of High-Resolution Methods in Large Eddy Simulations of Subsonic and Supersonic Wall Turbulent Flows*. PhD Thesis, University of Cranfield, 2009.

[2] A. Mosedale and D. Drikakis. Assessment of very high-order of accuracy in LES models. *Journal of Fluids Engineering*, 129:1497–1503, 2007.

[3] J. Jeong and F. Hussain. On the identification of a vortex. *Journal of Fluid Mechanics*, 285:69–94, 1995.

[4] A. N. Kolmogorov. The local structure of turbulence in incompressible viscous fluid for very large Reynolds number. *Doklady Akademii Nauka SSSR*, 30:299–303, 1941.

[5] K. Sudo, M. Sumida, and H. Hibara. Experimental investigation on turbulent flow in a square-sectioned 90-degree bend. *Experiments in Fluids*, 30(3):246–252, 2001.

[6] M. Raisee, A. Noursadeghi, and H. Iacovides. Application of a non-linear k-e model in prediction of convective heat transfer through ribbed passages. *International Journal of Numerical Methods for Heat and Fluid Flow*, 14(3):285–304, 2004.

[7] K. Sudo, M. Sumida, and H. Hibara. Experimental investigation on turbulent flow through a circular-sectioned 180°bend. *Experiments in Fluids*, 28(1):51–57, 2001.

[8] S. Yanase, R. N. Mondal, and Y. Kaga. Numerical study of non-isothermal flow with convective heat transfer in a curved rectangular duct. *International Journal of Thermal Sciences*, 44(11):1047–1060, 2005.

[9] K. A. Papakonstantinou, C. T. Kiranoudis, and N. C. Markatos. Computational analysis of thermal comfort: The case of the archaeological museum of Athens. *Applied Mathematical Modelling*, 24(7):477–494, 2000.

[10] C. J. Koinakis. The effect of the use of openings on interzonal air flows in buildings: An experimental and simulation approach. *Energy and Buildings*, 37(8):813–823, 2005.

[11] Y. Li, X. Huang, I. T. S. Yu, T. W. Wong, and H. Qian. Role of air distribution in sars transmission during the largest nosocomial outbreak in hong kong. *Indoor Air*, 15(2):83–95, 2005.

[12] L. R. Coke, J. G. Sanchez, and A. J. Policastro. A model for the dispersion of contaminants in the subway environment. *Report for OSTI, USA*, 2000.

[13] J. S. M. Li and W. K. Chow. Numerical studies on performance evaluation of tunnel ventilation safety systems. *Tunnelling and Underground Space Technology*, 18(5): 435–452, 2003.

[14] J. Bosbach, J. Pennecot, C. Wagner, M. Raffel, T. Lerche, and S. Repp. Experimental and numerical simulations of turbulent ventilation in aircraft cabins. *Energy*, 31(5): 694–705, 2006.

[15] J. Bosbach, J. Pennecot, C. Wagner, I. Gores, and T. Lerche. Particle image velocity and hot wire anemometry for investigation of premature flow separation in a generic aircraft cabin mock-up. *www.dlr.de*, 2005.

[16] P. M. Ligrani and C. R. Hedlund. Experimental surface heat transfer and flow structure in a curved channel with laminar, transitional, and turbulent flows. *Journal of Turbomachinery*, 126(3):414–423, 2004.

[17] K. Suga. Predicting turbulence and heat transfer in 3-d curved ducts by near-wall second moment closures. *International Journal of Heat and Mass Transfer*, 46(1): 161–173, 2003.

[18] N. R. Rosaguti, D. F. Fletcher, and B. S. Haynes. Laminar flow and heat transfer in a periodic serpentine channel with semi-circular cross-section. *International Journal of Heat and Mass Transfer*, 49(17-18):2912–2923, 2006.

[19] H. Schlichting. *Boundary-Layer Theory*. McGraw-Hill, New York, 1979.

[20] S. Gavrilakis. Numerical simulation of low-Reynolds-number turbulent flow through a straight square duct. *Journal of Fluid Mechanics*, 244:101–129, 1992.

[21] M. Anwer, R. M. C. So, and Y. G. Lai. Perturbation by and recovery from bend curvature of a fully developed turbulent pipe flow. *Physics of Fluids A*, 1(8):1387–1397, 1989.

[22] T. H Ko. A numerical study on entropy generation and optimization for laminar forced convection in a rectangular curved duct with longitudinal ribs. *International Journal of Thermal Sciences*, 45(11):1113–1125, 2006.

[23] J. Laufer. Investigation of turbulent flow in a two-dimensional channel. *National Advisory Committee for Aeronautics*, Technical Note 2123.

[24] T. Wei and W. W. Willmarth. Reynolds-number effects on the structure of a turbulent channel flow. *Journal of Fluid Mechanics*, 204:57–59, 1989.

[25] A. Melling and J. H. Whitelaw. Turbulent flow in a rectangular duct. *Journal of Fluid Mechanics*, 78:289–315, 1976.

[26] F. B. Gessner and A. F. Emery. The numerical prediction of developing turbulent flow in rectangular ducts. *Journal of Fluid Engineering*, 103:445–455, 1981.

[27] E. Brundrett and W. D. Baines. The production and diffusion of vorticity in duct flow. *Journal of Fluid Mechanics*, 19:375–394, 1964.

[28] M. M. Enayet, M. M. Gibson, A. M. K. P. Taylor, and M. Yianneskis. Laser-doppler measurements of laminar and turbulent flow in a pipe bend. *International Journal of Heat and Fluid Flow*, 3:213–219, 1982.

[29] J. A. C. Humphrey and J. H. Whitelaw. Measurements in curved flows. *Proceedings of SQUID Conference, Interanl Flows, Airlie House*, 1976.

[30] A. M. K. P. Taylor, J. H. Whitelaw, and M. Yianneskis. Curved ducts with strong secondary motion: velocity measurements of developing laminar and turbulent flow. *Journal of Fluids Engineering*, 104:350–359, 1982.

[31] W. J. Kim and V. C. Patel. Origin and decay of longitudinal vortices in developing flow in a curved rectangular duct. *Journal of Fluids Engineering*, 116:45–52, 1994.

[32] J. P. Kreskovsky, W. R. Briley, and H. McDonald. Prediction of laminar and turbulent primary and secondary flows in strongly curved ducts. *NASA Report*, No. CR.3388, 1981.

[33] H. Iacovides, B. E. Launder, and P. A. Loizou. Numerical computation of turbulent flow through a square-sectioned 90 degree bend. *International Journal of Heat and Fluid Flow*, 8(4):320–325, 1987.

[34] M. Hidayat and A. Rasmuson. A computational investigation of non-isothermal gas-solid flow in a U-bend. *Powder Technology*, 175(2):104–114, 2007.

[35] K. S P. Nikas and H. Iacovides. The computation of flow and heat transfer through square-ended U-bends, using low-Reynolds-number models. *International Journal of Numerical Methods for Heat and Fluid Flow*, 14(3):305–324, 2004.

[36] J. Pruvost, J. Legrand, and P. Legentilhomme. Numerical investigation of bend and torus flows, part I : Effect of swirl motion on flow structure in U-bend. *Chemical Engineering Science*, 59(16):3345–3357, 2004.

[37] H. Iacovides, B. E. Launder, and H. Y Li. Application of a reflection-free dsm to turbulent flow and heat transfer in a square-sectioned U-bend. *Experimental Thermal and Fluid Science*, 13(4):419–429, 1996.

[38] H. Iacovides. The computation of turbulent flow through stationary and rotating U-bends with rib-roughened surfaces. *International Journal for Numerical Methods in Fluids*, 29(7):865–876, 1999.

[39] B. Kuan, W. Yang, and M. P. Schwarz. Dilute gas-solid two-phase flows in a curved 90°duct bend: CFD simulation with experimental validation. *Chemical Engineering Science*, 62(7):2068–2088, 2007.

[40] B. T. Kuan and M. P. Schwarz. CFD simulation of single-phase and dilute particulate turbulent flows in 90°duct bends. volume 2 C, pages 1901–1908, 2003.

[41] W. Yang and B. Kuan. Experimental investigation of dilute turbulent particulate flow inside a curved 90°bend. *Chemical Engineering Science*, 61(11):3593–3601, 2006.

[42] M. R. Mokhtarzadeh-Dehghan and Y. M. Yuan. Measurements of turbulence quantities and bursting period in developing turbulent boundary layers on the concave and convex walls of a 90°square bend. *Experimental Thermal and Fluid Science*, 27(1): 59–75, 2003.

[43] N. M. Crawford, G. Cunningham, and P. L. Spedding. Prediction of pressure drop for turbulent fluid flow in 90°bends. *Proceedings of the Institution of Mechanical Engineers, Part E: Journal of Process Mechanical Engineering*, 217(3):153–156, 2003.

[44] Y. D. Choi, D. C. Kim, and K. H. Lee. Measurement of developing turbulent flows in a 90-degree square bend with spanwise rotation. *Journal of Mechanical Science and Technology*, 19(7):1503–1516, 2005.

[45] S. P. Vanka, G. Luo, and C. M. Winkler. Numerical study of scalar mixing in curved channels at low Reynolds numbers. *AIChE Journal*, 50(10):2359–2368, 2004.

[46] P. K. Papadopoulos and P. M. Hatzikonstantinou. Numerical analysis of fully developed flow in curved square ducts with internal fins. *Journal of Fluids Engineering*, 126(5):752–757, 2004.

[47] A. Mangili and M. A. Gendreau. Transmission of infectious diseases during commercial air travel. *Lancet*, 365(9463):989–996, 2005.

[48] P. Moin and K. Mahesh. Direct Numerical Simulation: A tool in turbulence research. *Annual Review of Fluid Mechanics*, 30:539–578, 1998.

[49] F. S. Lien, G. Kalitzin, and P. A. Durbin. RANS modeling for compressible and transitional flows. *Center for Turbulence Research, Proceedings of the Summer Program*, 1998.

[50] J. A. Ramirez and C. Cortes. Comparison of different URANS schemes for the simulation of complex swirling flows. *Numerical Heat Transfer, Part B*, 58:98–120, 2010.

[51] M. Lesieur and O. Metais. New trends in large-eddy simulations of turbulence. *Annual Review of Fluid Mechanics*, 28:45–82, 1996.

[52] E. Garnier, N. Adams, and P. Sagaut. *Large Eddy Simulation for Compressible Flows*. Springer Science, 2009.

[53] D. Drikakis and W. Rider. *High-Resolution Methods for Incompressible and Low-Speed Flows*. Springer, Berlin Heidelberg, 2005.

[54] J. Hebrard, O. Metais, and M. Salinas-Vasquez. Large-eddy simulation of turbulent duct flow: Heating and curvature effects. *International Journal of Heat and Fluid Flow*, 25(4):569–580, 2004.

[55] K. M. Guleren and A. Turan. Validation of large-eddy simulation of strongly curved stationary and rotating u-duct flows. *International Journal of Heat and Fluid Flow*, 2007.

[56] Z. Qin and R. H. Pletcher. Large eddy simulation of turbulent heat transfer in a rotating square duct. *International Journal of Heat and Fluid Flow*, 27(3):371–390, 2006.

[57] J. A. C. Humphrey, J. H. Whitelaw, and G. Yee. Turbulent flow in a square duct with strong curvature. *Journal of Fluid Mechanics*, 103:443–463, 1981.

[58] F. F. Grinstein and C. Fureby. From canonical to complex flows: Recent progress on monotonically integrated LES. *Computing in Science and Engineering*, 6(2):36–49, 2004.

[59] F. F. Grinstein, C. Fureby, and C. R. DeVore. On miles based on flux-limiting algorithms. *International Journal for Numerical Methods in Fluids*, 47(10-11):1043–1051, 2005.

[60] J. P. Boris, F. F. Grinstein, E. S. Oran, and R. L. Kolbe. New insights into large eddy simulation. *Fluid Dynamics Research*, 10(4-6):199–228, 1992.

[61] L. G. Margolin and W. J. Rider. The design and construction of implicit LES models. *International Journal for Numerical Methods in Fluids*, 47(10-11):1173–1179, 2005.

[62] S. Hickel, N. A. Adams, and J. A. Domaradzki. On the evolution of dissipation rate and resolved kinetic energy in ALDM simulations of the Taylor-Green flow. *Journal of Computational Physics*, 229:2422–2423, 2010.

[63] M. Hahn and D. Drikakis. Large eddy simulation of compressible turbulence using high-resolution methods. *International Journal for Numerical Methods in Fluids*, 47(8-9):971–977, 2005.

[64] D. L. Youngs. Numerical simulation of mixing by Rayleigh-Taylor and Richtmyer-Meshkov instabilities. *Laser and Particle Beams*, 12(4):725–750, 1994.

[65] D. L. Youngs. Three-dimensional numerical simulation of turbulent mixing by Rayleigh-Taylor instability. *Physics of Fluids*, 3(5):1312, 1991.

[66] M. Hahn and D. Drikakis. Implicit Large-Eddy Simulation of Swept-Wing Flow Using High-Resolution Methods. *AIAA*, 47(3):618–630, March 2009.

[67] G. Patnaik, J. P. Boris, and T. R. Young. Large scale urban contaminant transport simulations with Miles. *Journal of Fluids Engineering*, 129:1524–1532, 2007.

[68] B. Thornber, M. Starr, and D. Drikakis. Large eddy simulation of ship airwakes. *accepted Aeronautical Journal*, 2010.

[69] C. Fureby. Large eddy simulation of ship hydrodynamics. *In proceedings of the 27th Symposium on Naval Hydrodynamics, Seoul, Korea*, 2008.

[70] D. Drikakis, M. Hahn, A. Mosedale, and B. Thornber. Large eddy simulation using high-resolution and high-order methods. *Philosophical Transactions of the Royal Society A*, 367(1899):2985–2997, 2009.

[71] F. F. Grinstein and C. Fureby. Recent progress on miles for high Reynolds number flows. *Journal of Fluids Engineering*, 124(4):848–861, 2002.

[72] L. Margolin. Modelling turbulent flow with implicit LES. *Journal of Turbulence*, 7: 1–27, 2006.

[73] D. Drikakis and S. Tsangaris. An implicit characteristic-flux-averaging method for the Euler equations for real gases. *International Journal of Numerical Methods in Fluids*, 12:711–726, 1991.

[74] D. Drikakis and S. Tsangaris. On the solution of the compressible Navier-Stokes equations using improved flux vector splitting methods. *Applied Mathematical Modelling*, 17:282–297, 1993.

[75] D. Drikakis and S. Tsangaris. Local Solution Acceleration Method for the Compressible Euler and Navier-Stokes Equations. *AIAA*, 30:340–348, 1992.

[76] D. Drikakis and F. Durst. Investigation of flux formulae in shock wave turbulent boundary layer interaction. *International Journal for Numerical Methods in Fluids*, 18:385–413, 1994.

[77] D. Drikakis. Advances in turbulent flow computations using high-resolution methods. *Progress in Aerospace Sciences*, 39:405–424, 2003.

[78] D. Drikakis and S. Tsangaris. Zonal-local solution method for the accelerated solution of the turbulent Navier-Stokes equations. *AIAA*, 31:1759–1760, 1993.

[79] D. Drikakis, E. Shapiro, I. Kokkinakis, and C. Papachristou. Implicit large eddy simulation of fluid flow. *HEFAT2010, 7th International Conference on Heat Transfer, Fluid Mechanics and Thermodynamics 19-21 July 2010, Antalya, Turkey*.

[80] D. Drikakis. Godunov methods: Theory and applications, chap. uniformaly highorder methods for unsteady incompressible flows. *Kluwer Academic Publishers*, 2008.

[81] B. Thornber, A. Mosedale, D. Drikakis, D. Youngs, and R. J. R. Williams. An improved reconstruction method for compressible flows with low mach number features. *Journal of Computational Phyics*, 227(10):4873, 2008.

[82] B. Thornber, D. Drikakis, R. J. R.Williams, , and D. Youngs. On entropy generation and dissipation of kinetic energy in high-resolution shock-capturing schemes. *Journal of Computational Phyics*, 227(10):4853, 2008.

[83] C. A. Lowe. Two-phase shock-tube problems and numerical methods of solution. *Journal of Computational Physics*, 204(2):598 – 632, 2005.

[84] S. K. Godunov. Finite diference method for numerical computation of discontinuous solutions of the equations of fluid dynamics. *Matematicheski Sbornik*, 47:271, 1959.

[85] P. L. Roe. Approximate riemann solvers, parameter vectors and difference schemes. *Journal of Computational Physics*, 43:357–372, 1981.

[86] E. F. Toro, M. Spruce, and W. Speares. Restoration of the contact surface in the HLL-Riemann solver. *Shock Waves*, 4:25–34, 1994.

[87] H. Ishikawa and K. Kitamura. Very simple, carbuncle-free, boundary-layer-resolving, rotated-hybrid riemann solvers. *Journal of Computational Physics*, 227: 2560–2581, 2008.

[88] E. F. Toro. *Riemann Solvers and Numerical Methods for Fluid Dynamics*. Springer, New York, 1997.

[89] B. Thornber and D. Drikakis. Implicit large eddy simulation of a deep cavity using high resolution methods. *AIAA*, 46:2634–2645, 2008.

[90] M. Hahn and D. Drikakis. Implicit large-eddy simulation of swept-wing flow using high resolution methods. *AIAA*, 47:618–630, 2008.

[91] B. Thornber, B. Mosedale, and D. Drikakis. On the implicit large eddy simulation of homogeneous decaying turbulence. *Journal of Computational Physics*, 226:1902–1929, 2007.

[92] E. Garnier, M. Mossi, P. Sagaut, P. Comte, and M. Deville. On the use of shock-capturing schemes for large-eddy simulaton. *Journal of Computational Physics*, 153:273–311, 1999.

[93] B. van Leer. Towards the ultimate conservative difference scheme. part II: Monotonicity and conservation combined in a second order scheme. *Journal of Computational Physics*, 14:361–370, 1974.

[94] X. D. Liu, S. Osher, and T. Chan. Weighted essentially non-oscillatory schemes. *Journal of Computational Phyics*, 115:200–212, 1994.

[95] K. H. Kim and C. Kim. Accurate, efficient and monotonic numerical methods for multi-dimensional compressible flows. part II: Multi-dimensional limiting process. *Journal of Computational Physics*, 208:570–615, 2005.

[96] A. Harten, B. Engquist, S. Osher, and J. Chakravarthy. Uniformly high order accurate essentially non-oscillatory schemes III. *Journal of Computational Physics*, 71: 231–303, 1987.

[97] D. S. Balsara and C. W. Shu. Monotonicity preserving weighted essentially non-oscillatory schemes with increasingly high order of accuracy. *Journal of Computational Physics*, 160:405–452, 2000.

[98] G. S. Jiang and C. W. Shu. Efficient implementation of weighted ENO schemes. *Journal of Computational Physics*, 126:202–228, 1996.

[99] P. S. Pacheco. *Parallel Programming with MPI*. Morgan Kaufmann Publishers, San Francisco, 1997.

[100] N. MacDonald, E. Minty, J. Malard, T. Harding, S. Brown, and M. Antonioletti. Wrinting message passing parallel programs with mpi. Edinburgh Parallel Computing Centre, University of Edinburgh.

[101] E. Lenormand, P. Sagaut, L. T. Phuoc, and P. Comte. Subgrid-scale models for large-eddy simulation of compressible wall bounded flows. *AIAA*, 38(8):1340, 2000.

[102] V. Deschamps. Simulation numerique de la turbulence inhomogene incompressible dans un ecoulement de canal plan. *Tech. Rep. 1988/5, Onera, 29, Avenue de la Division Leclerc, 92320 Chatillon, France*, 1988.

[103] N. Mansour and A. Wray. Decay of isotropic turbulence at low Reynolds number. *Physics of Fluids*, 6(8):808–814, 1994.

[104] S. B. Pope. *Turbulent Flows*. Cambridge University Press, 2000.

[105] K. Noto. Direct Numerical Simulation of isothermal wake: DNS noise, strong anisotropy turbulence and vortex dislocation generation mechanism. *Numerical Heat Transfer, Part B*, 56:167 – 189, 2009.

[106] Z. Zhu, H. Yang, and T. Chen. Direct numerical simulation of turbulent flow in a straight square duct at Reynolds number 600. *Journal of Hydrodynamics*, 21(5): 600–607, 2009.

[107] A. M. K. P. Taylor, J. H. Whitelaw, and M. Yianneskis. Measurements of laminar and turbulent flow in a curved duct with thin inlet boundary layers. *NASA Contractor Report 3367*, 1981.

[108] M. Raisee, H. Alemi, and H. Iacovides. Prediction of developing turbulent flow in 90°-curved ducts using linear and non-linear low-re k-e models. *International Journal for Numerical Methods in Fluids*, 51(12):1379–1405, 2006.

[109] B. R. Munson BR and D. F. Young. *Fundamentals of Fluid Mechanics (2nd edn)*. Morgan Kaufmann Publishers, New York, 1994.

[110] A. K. Prasad and J. R. Koseff. Reynolds number and end-wall effects on a lid-driven cavity flow. *Physics of Fluids A*, 1(2):208–218, 1989.

APPENDIX A

L-bend grid comparisons

Grid result comparisons for the L-bend case against experimental data. Streamwise velocity U:

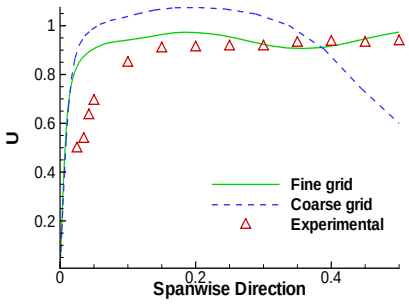

$x = -0.25$, $D = 0.1$

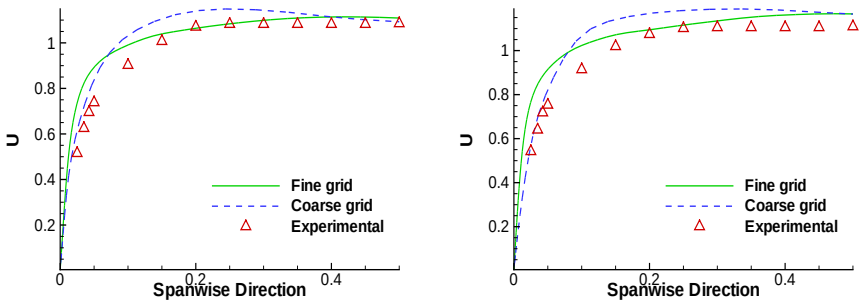

$x = -0.25$, $D = 0.3$ and $D = 0.5$

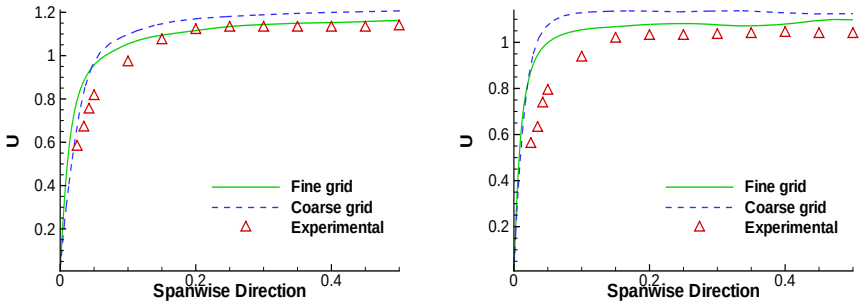

$x = -0.25$, $D = 0.7$ and $D = 0.9$

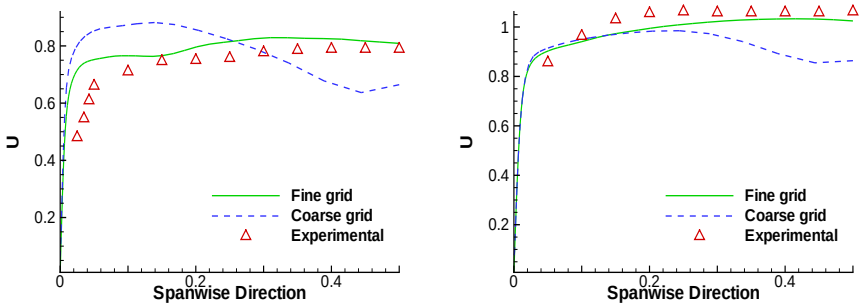

$\theta = 30^o$, $D = 0.1$ and $D = 0.3$

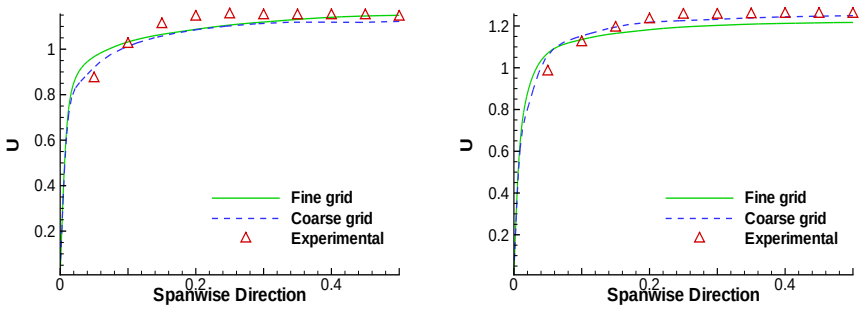

$\theta = 30^o$, $D = 0.5$ and $D = 0.7$

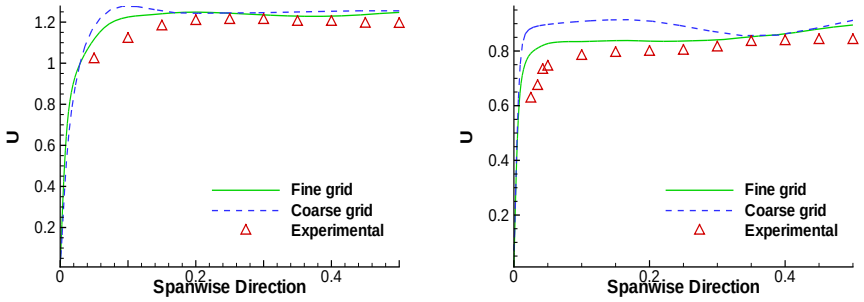

$\theta = 30^o$, $D = 0.9$ and $\theta = 60^o$, $D = 0.1$

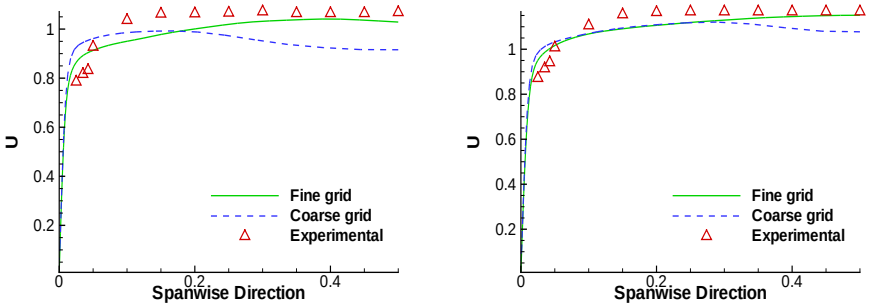

$\theta = 60^o$, $D = 0.3$ and $D = 0.5$

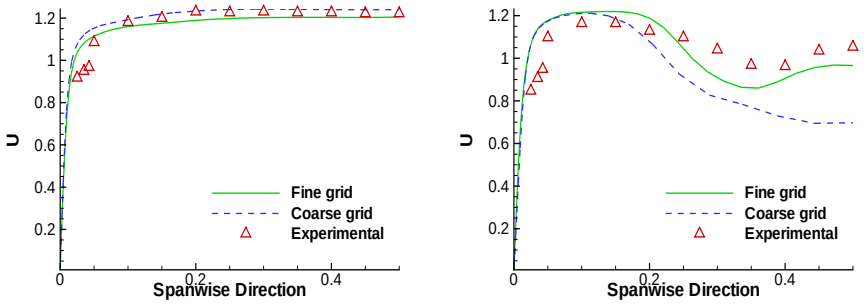

$\theta = 60^o$, $D = 0.7$ and $D = 0.9$

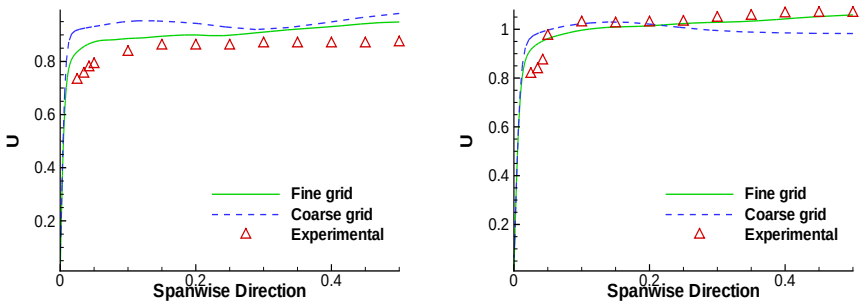

$\theta = 77.5^o$, $D = 0.1$ and $D = 0.3$

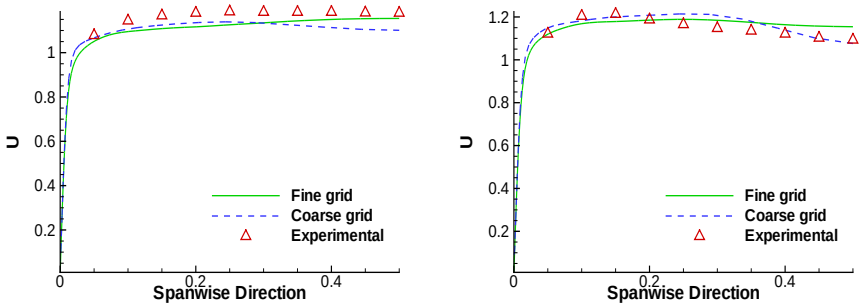

$\theta = 77.5^o$, $D = 0.5$ and $D = 0.7$

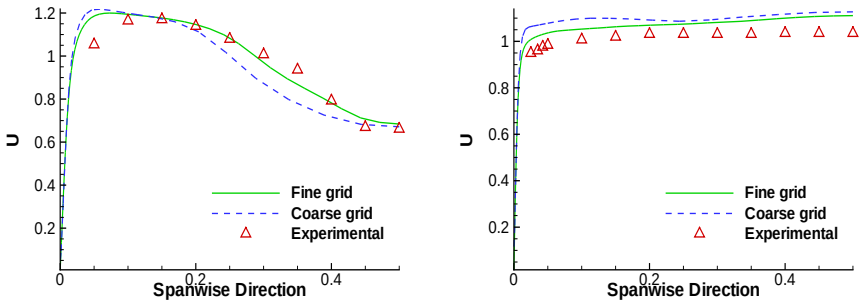

$\theta = 77.5^o$, $D = 0.9$ and $z = 0.25$, $D = 0.1$

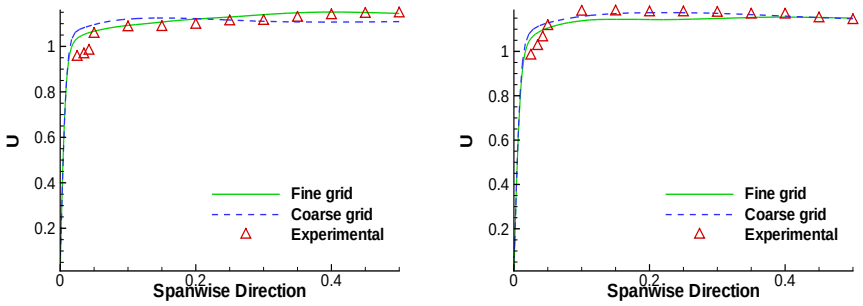

$z = 0.25$, $D = 0.3$ and $D = 0.5$

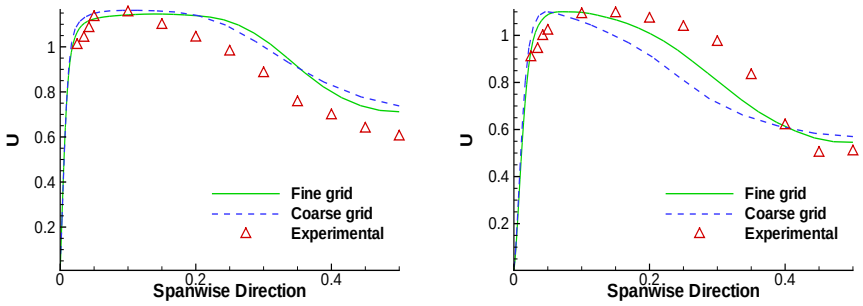

$z = 0.25$, $D = 0.7$ and $D = 0.9$

Gapwise velocity W:

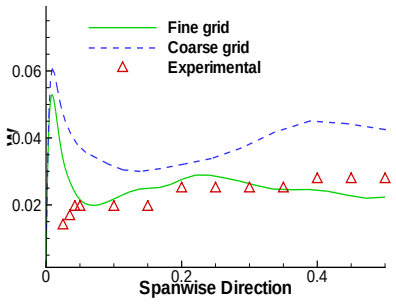

$x = -0.25$, $D = 0.1$

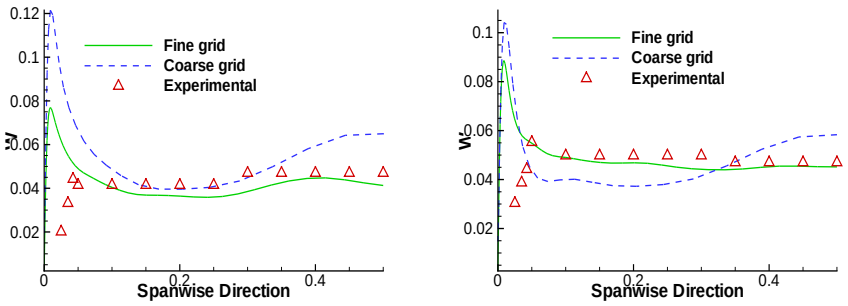

$x = -0.25$, $D = 0.3$ and $D = 0.5$

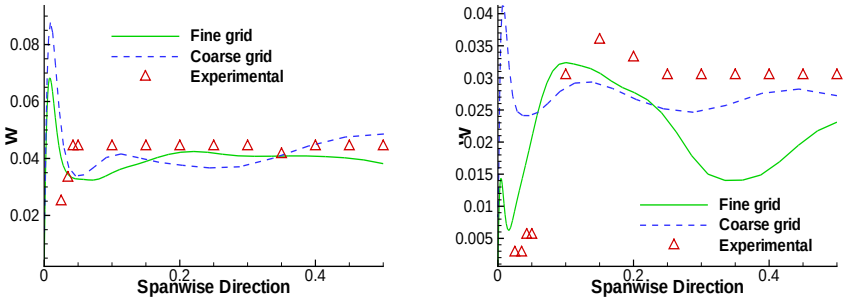

$x = -0.25$, $D = 0.7$ and $D = 0.9$

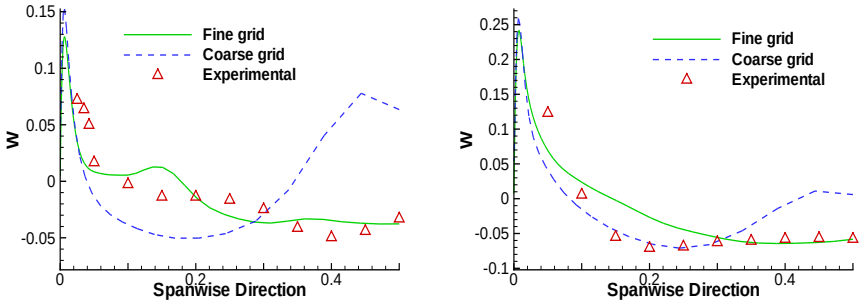

$\theta = 30^o$, $D = 0.1$ and $D = 0.3$

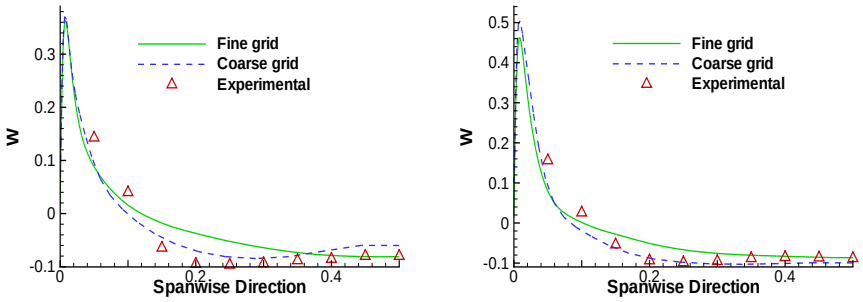

$\theta = 30^o$, $D = 0.5$ and $D = 0.7$

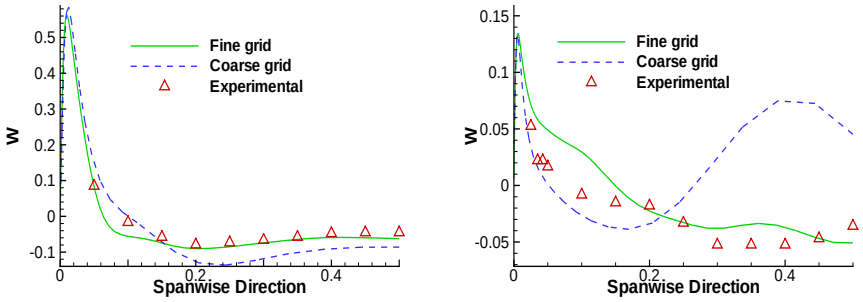

$\theta = 30^o$, $D = 0.9$ and $\theta = 60^o$, $D = 0.1$

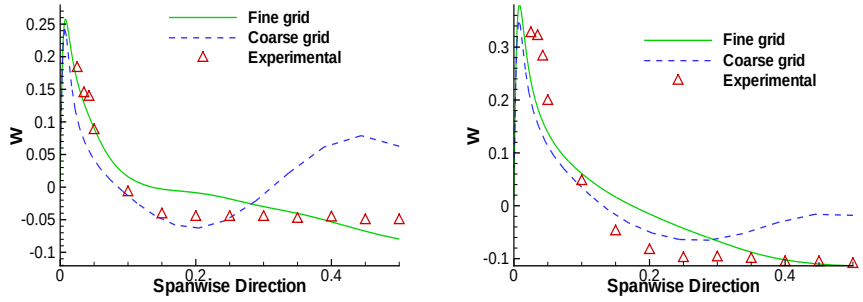

$\theta = 60^o$, $D = 0.3$ and $D = 0.5$

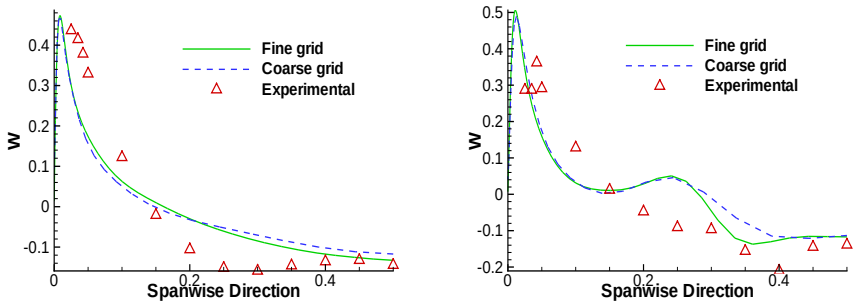

$\theta = 60^o$, $D = 0.7$ and $D = 0.9$

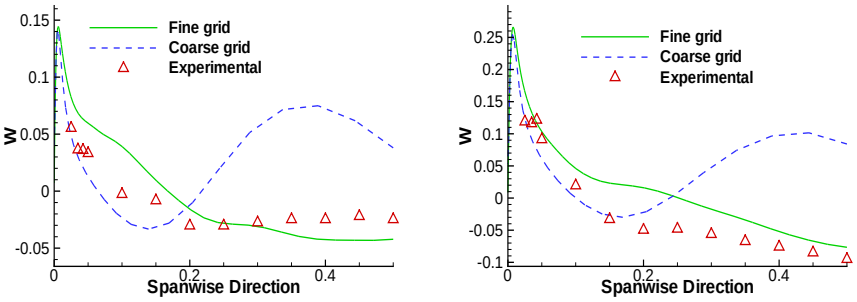

$\theta = 60^o$, $D = 0.7$ and $D = 0.9$

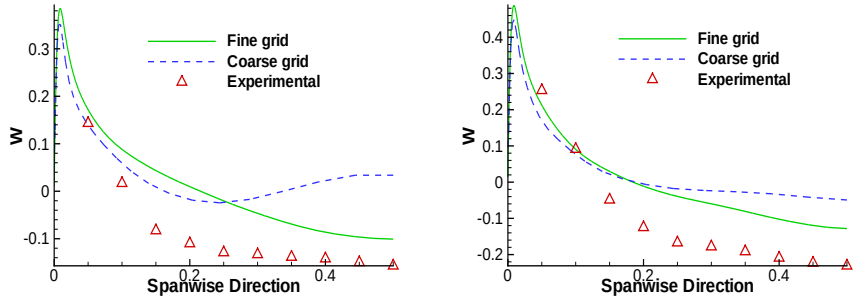

$\theta = 77.5^o$, $D = 0.5$ and $D = 0.7$

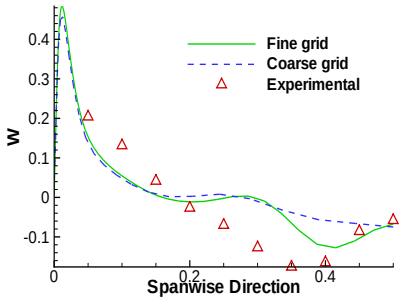

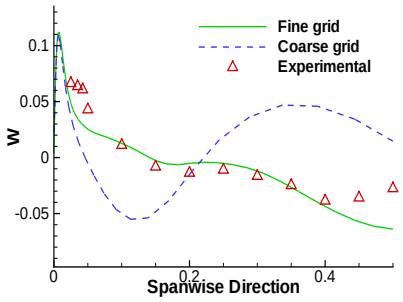

$\theta = 77.5^o$, $D = 0.9$ and $z = 0.25$, $D = 0.1$

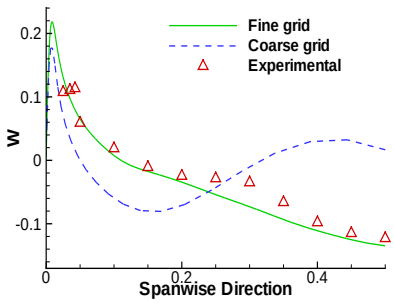

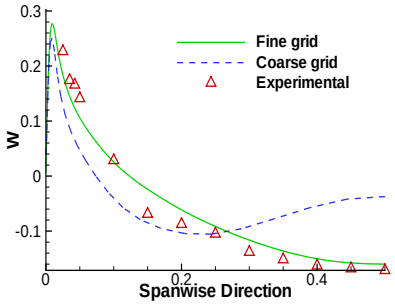

$z = 0.25$, $D = 0.3$ and $D = 0.5$

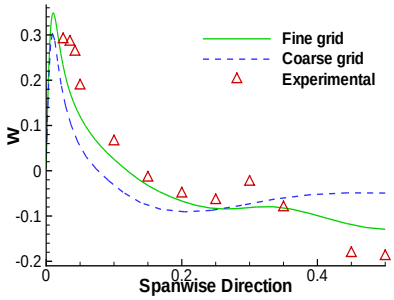

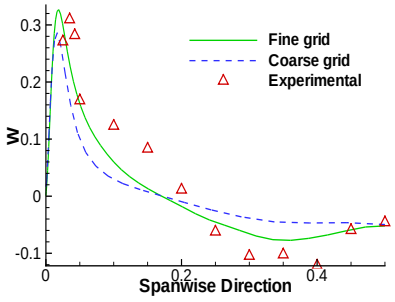

$z = 0.25$, $D = 0.7$ and $D = 0.9$

Streamwise Reynold stresses U_{rms}:

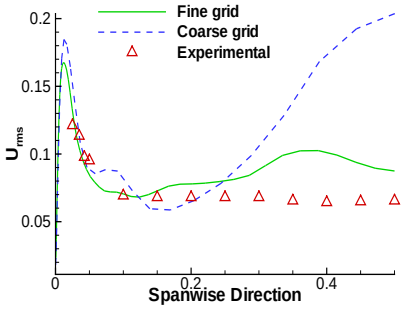

$x = -0.25$, $D = 0.1$

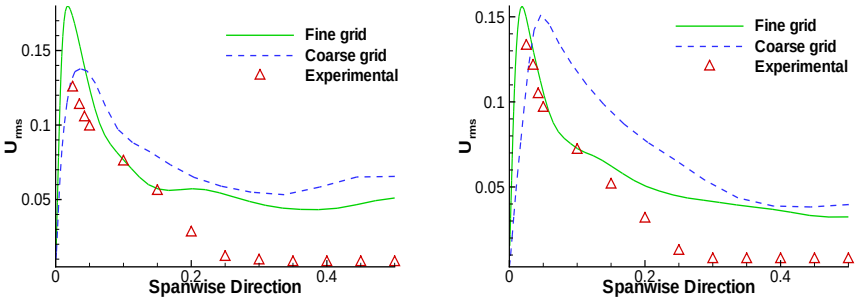

$x = -0.25$, $D = 0.3$ and $D = 0.5$

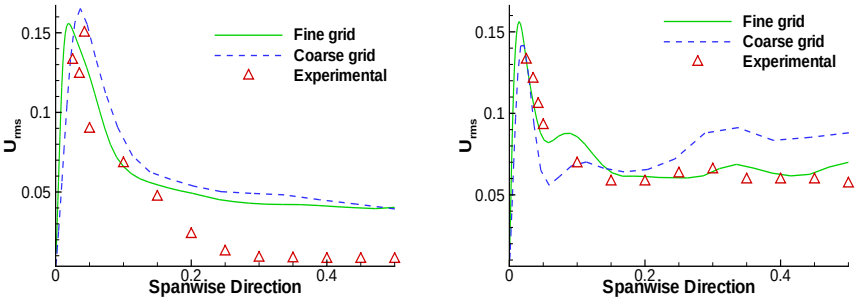

$x = -0.25$, $D = 0.7$ and $D = 0.9$

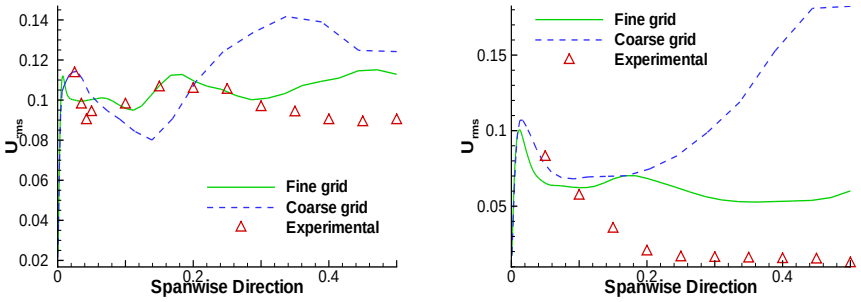

$\theta = 30^o$, $D = 0.1$ and $D = 0.3$

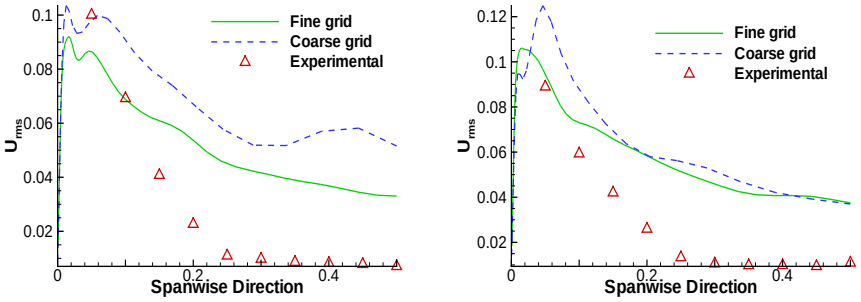

$\theta = 30^o$, $D = 0.5$ and $D = 0.7$

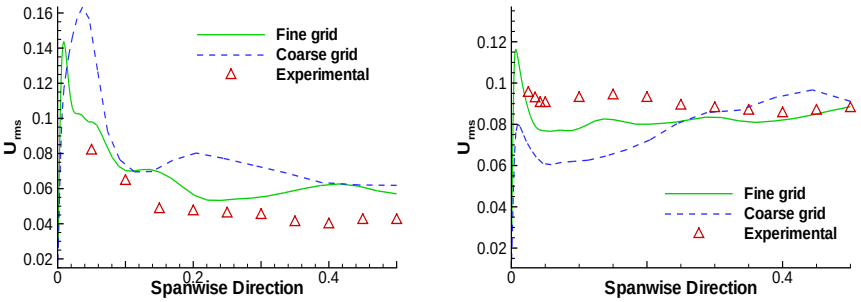

$\theta = 30^o$, $D = 0.9$ and $\theta = 60^o$, $D = 0.1$

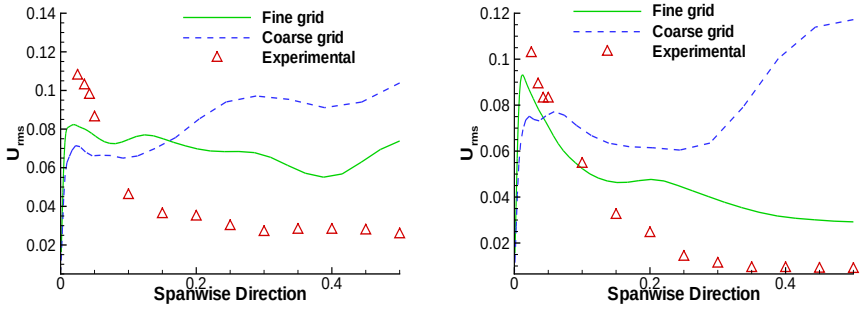

$\theta = 60^o$, $D = 0.3$ and $D = 0.5$

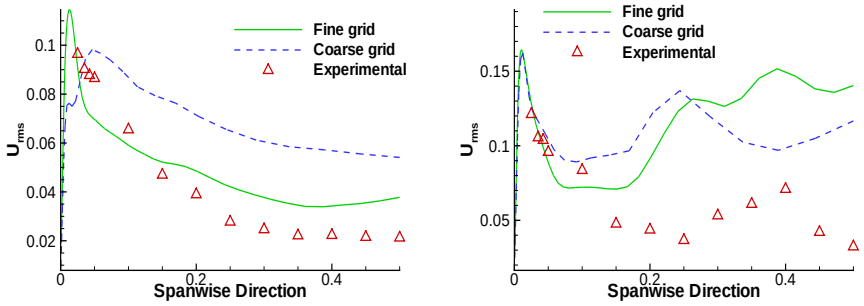

$\theta = 60^o$, $D = 0.7$ and $D = 0.9$

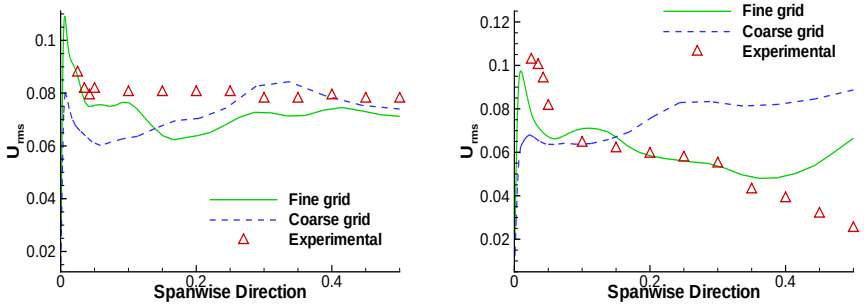

$\theta = 60^o$, $D = 0.7$ and $D = 0.9$

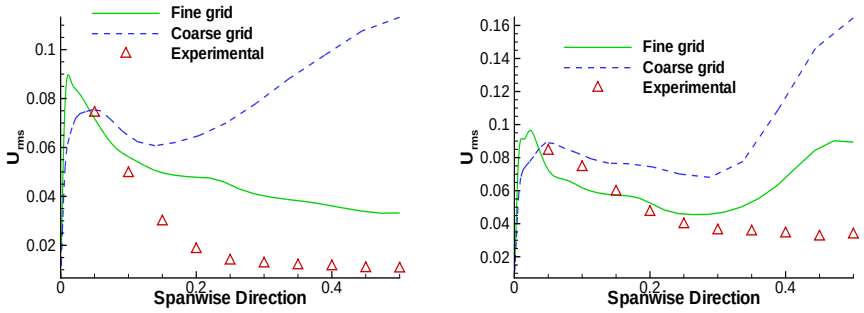

$\theta = 77.5^o$, $D = 0.5$ and $D = 0.7$

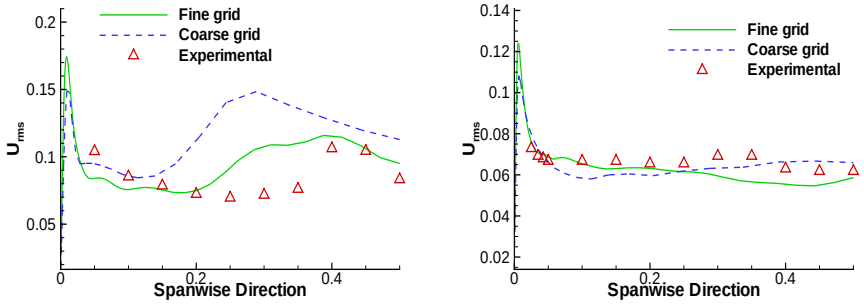

$\theta = 77.5^o$, $D = 0.9$ and $z = 0.25$, $D = 0.1$

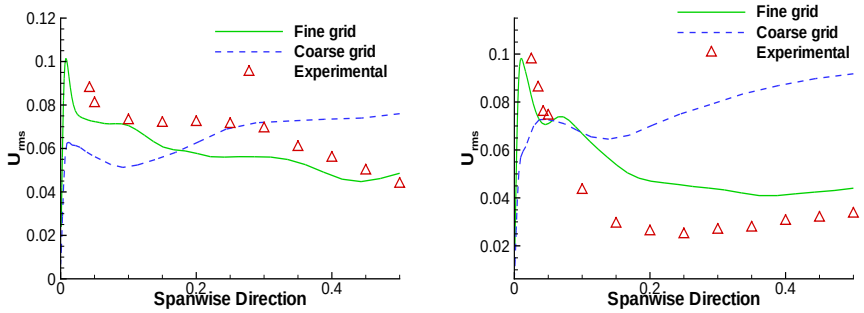

$z = 0.25$, $D = 0.3$ and $D = 0.5$

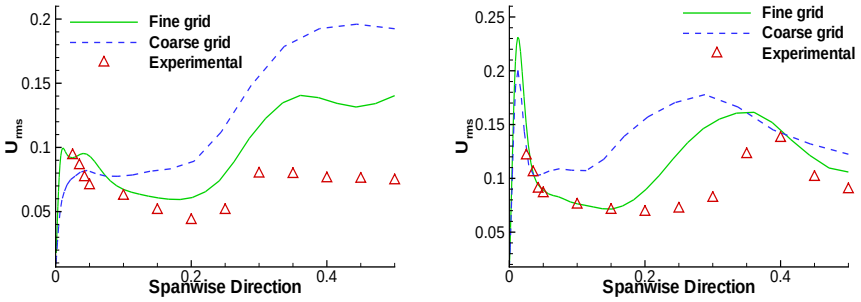

$z = 0.25$, $D = 0.7$ and $D = 0.9$

Streamwise Reynold stresses W_{rms}:

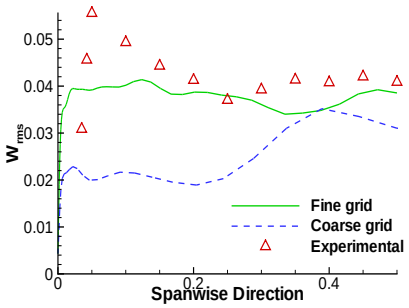

$x = -0.25$, $D = 0.1$

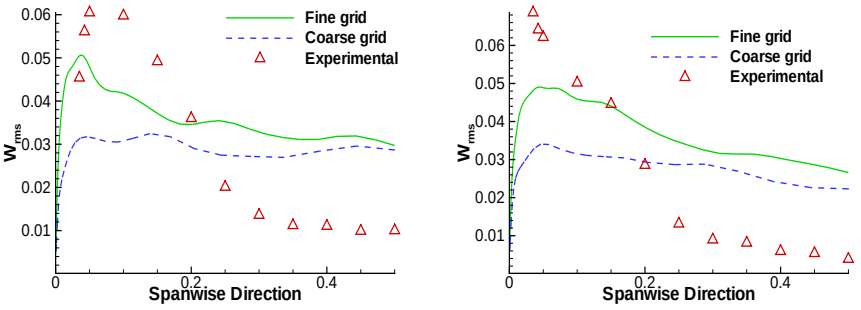

$x = -0.25$, $D = 0.3$ and $D = 0.5$

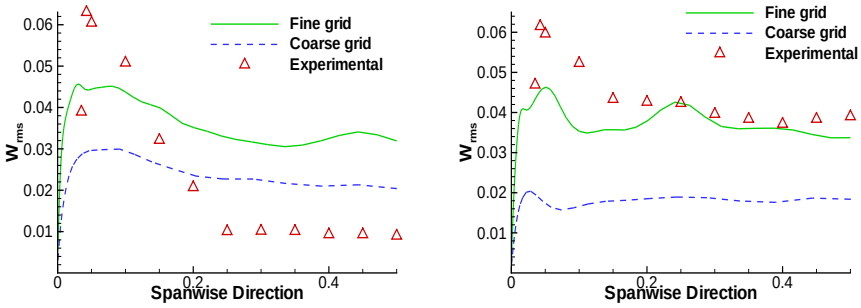

$x = -0.25$, $D = 0.7$ and $D = 0.9$

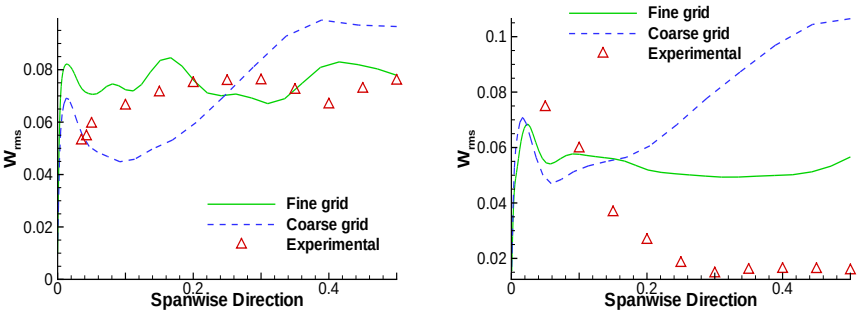

$\theta = 30^o$, $D = 0.1$ and $D = 0.3$

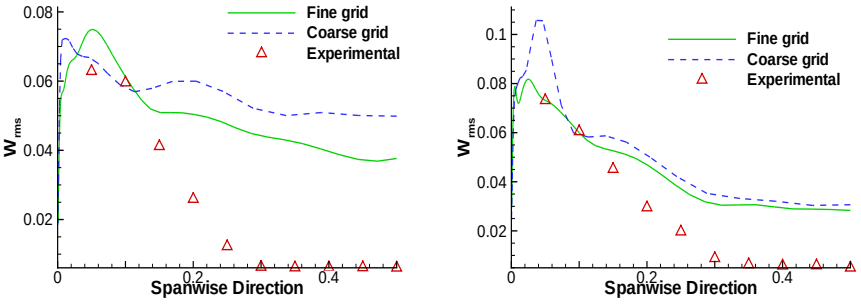

$\theta = 30^o$, $D = 0.5$ and $D = 0.7$

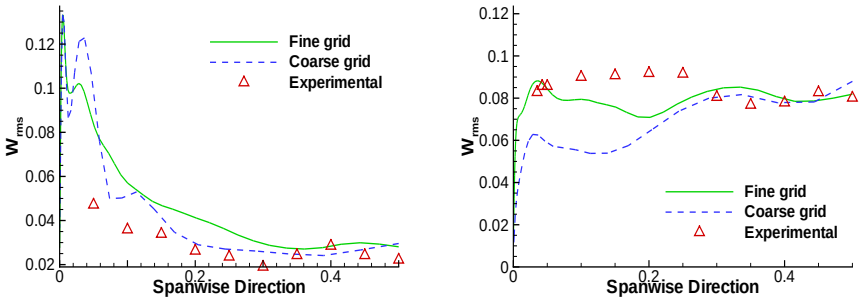

$\theta = 30^o$, $D = 0.9$ and $\theta = 60^o$, $D = 0.1$

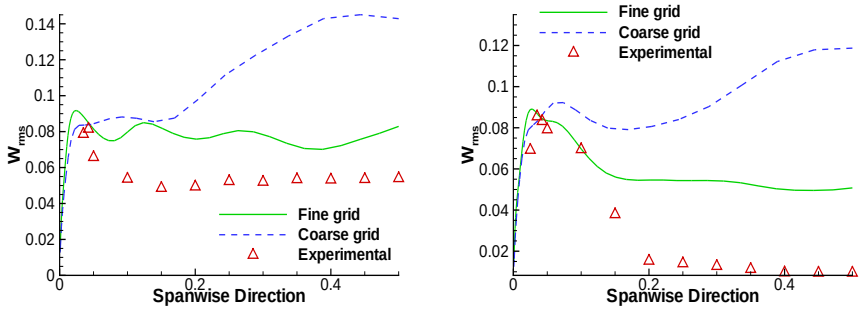

$\theta = 60^o$, $D = 0.3$ and $D = 0.5$

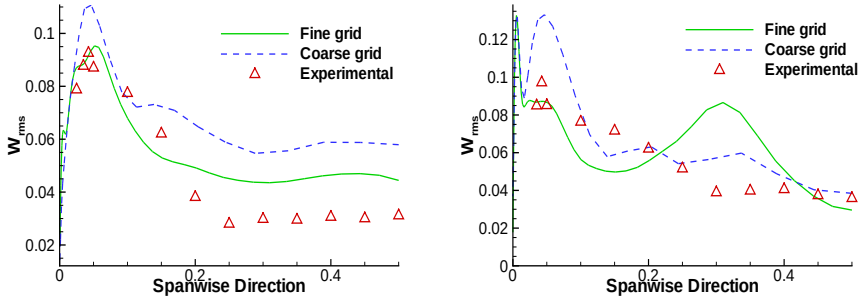

$\theta = 60^o$, $D = 0.7$ and $D = 0.9$

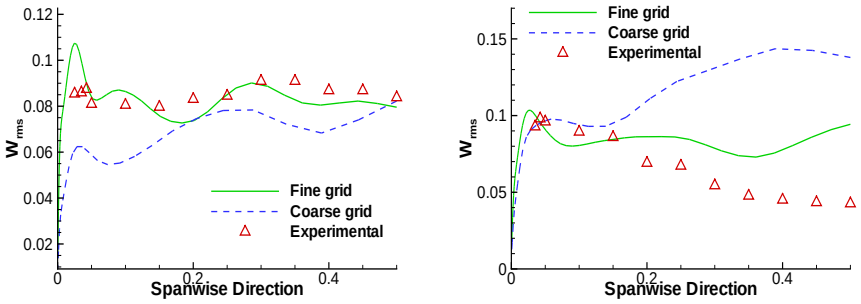

$\theta = 60^o$, $D = 0.7$ and $D = 0.9$

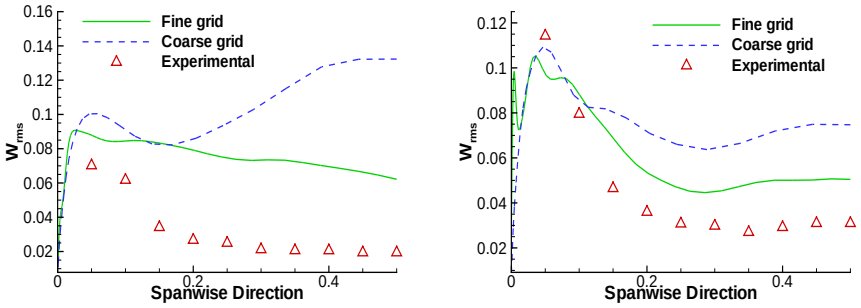

$\theta = 77.5^o$, $D = 0.5$ and $D = 0.7$

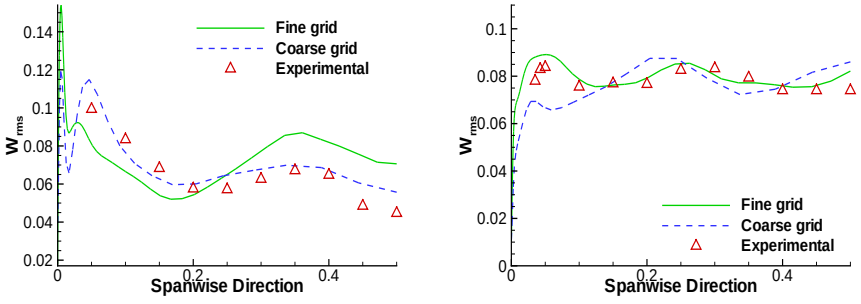

$\theta = 77.5^o$, $D = 0.9$ and $z = 0.25$, $D = 0.1$

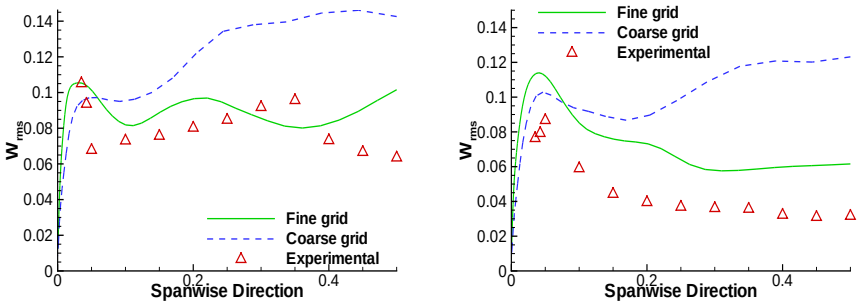

$z = 0.25$, $D = 0.3$ and $D = 0.5$

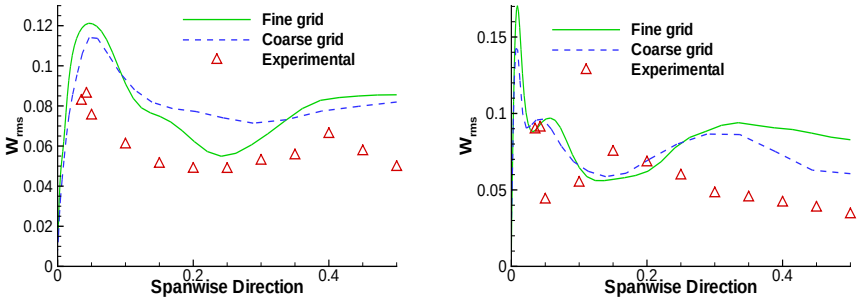

$z = 0.25$, $D = 0.7$ and $D = 0.9$

APPENDIX B

L-bend scheme comparisons

Different scheme results comparison against experimental data for the L-bend case. Streamwise velocity U:

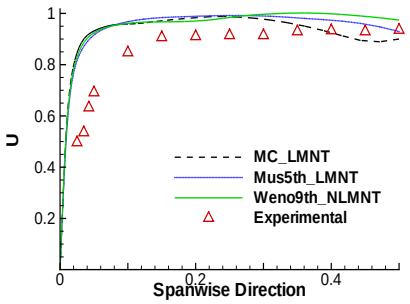

$x = -0.25$, $D = 0.1$

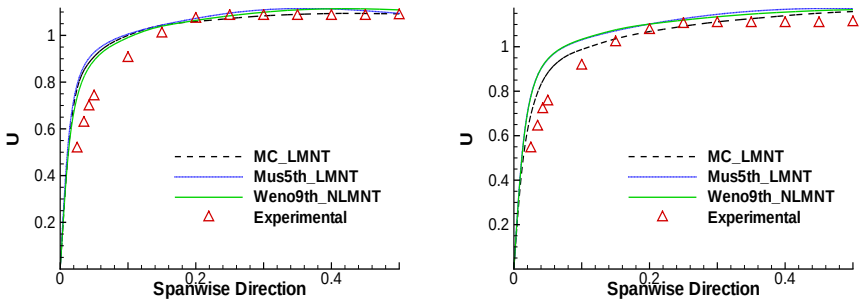

$x = -0.25$, $D = 0.3$ and $D = 0.5$

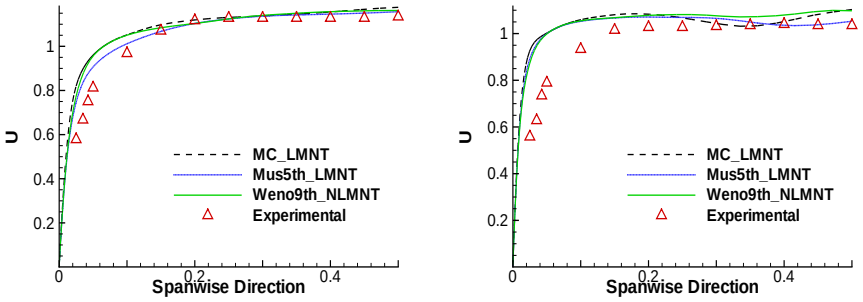

$x = -0.25$, $D = 0.7$ and $D = 0.9$

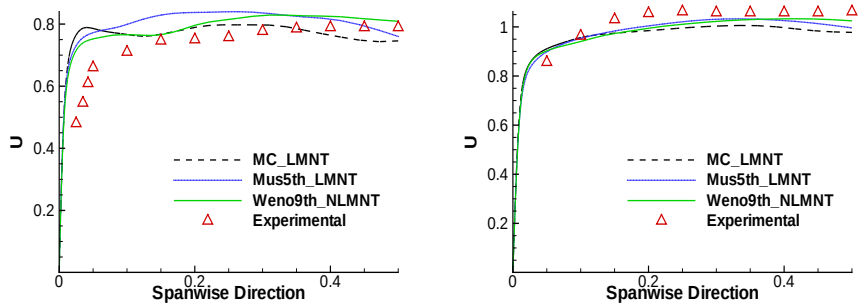

$\theta = 30^o$, $D = 0.1$ and $D = 0.3$

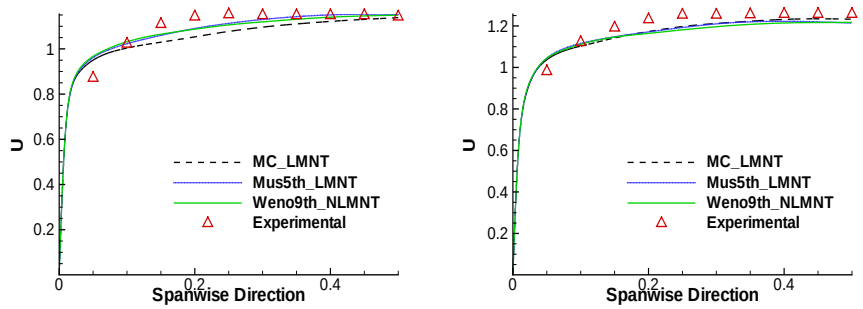

$\theta = 30^o$, $D = 0.5$ and $D = 0.7$

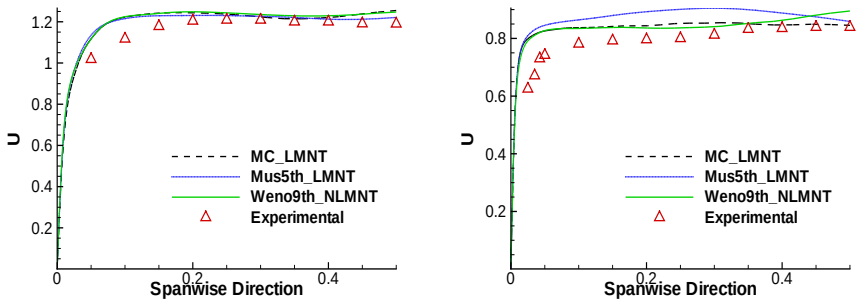

$\theta = 30^o$, $D = 0.9$ and $\theta = 60^o$, $D = 0.1$

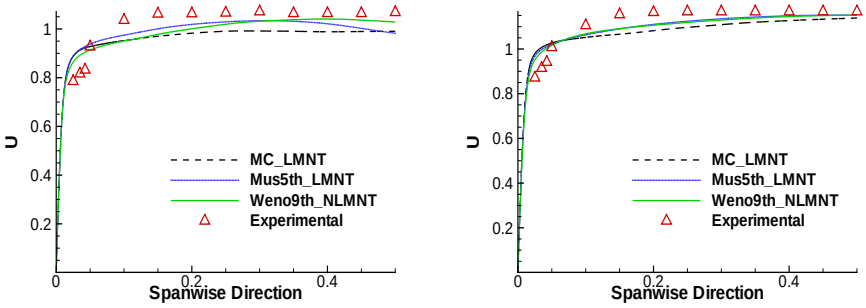

$\theta = 60^o$, $D = 0.3$ and $D = 0.5$

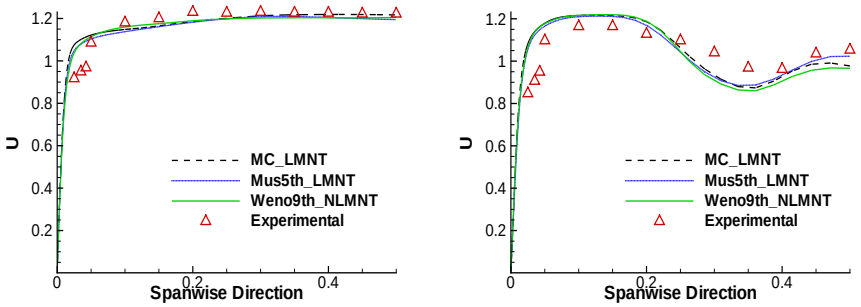

$\theta = 60^o$, $D = 0.7$ and $D = 0.9$

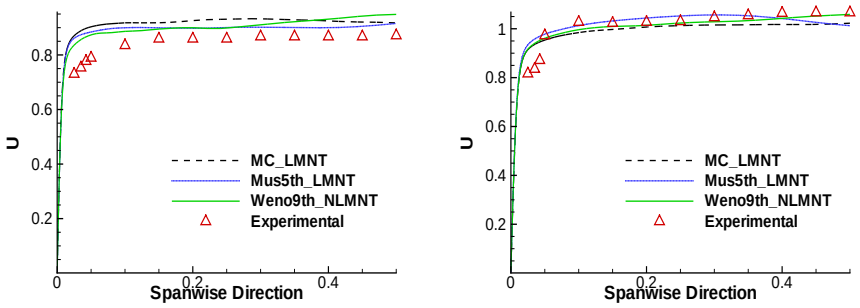

$\theta = 77.5^o$, $D = 0.1$ and $D = 0.3$

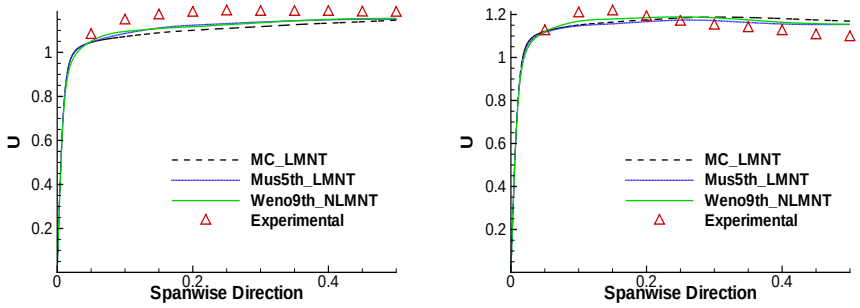

$\theta = 77.5^o$, $D = 0.5$ and $D = 0.7$

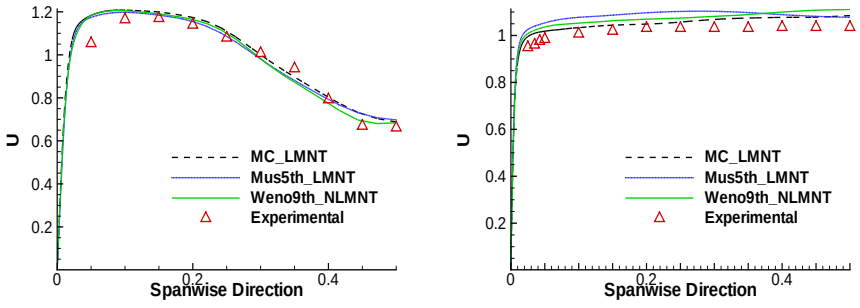

$\theta = 77.5^o$, $D = 0.9$ and $z = 0.25$, $D = 0.1$

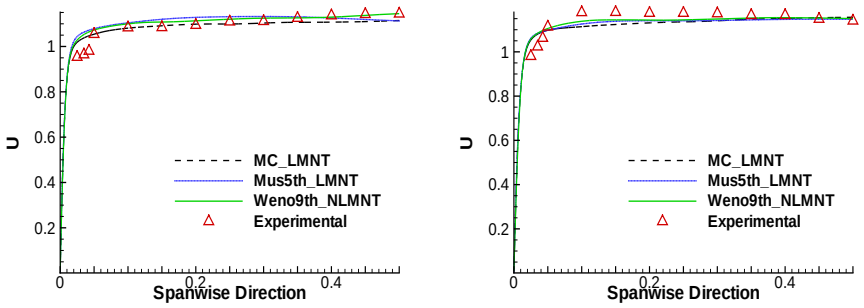

$z = 0.25$, $D = 0.3$ and $D = 0.5$

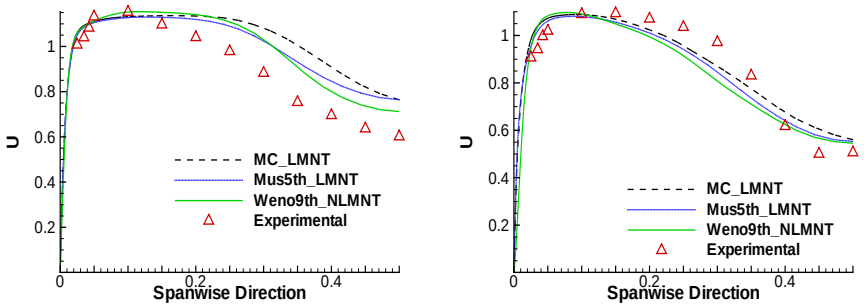

$z = 0.25$, $D = 0.7$ and $D = 0.9$

Gapwise velocity W:

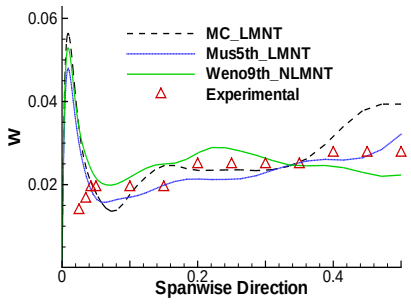

$x = -0.25$, $D = 0.1$

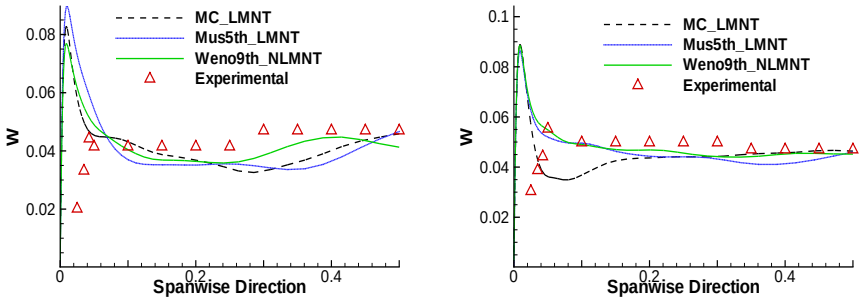

$x = -0.25$, $D = 0.3$ and $D = 0.5$

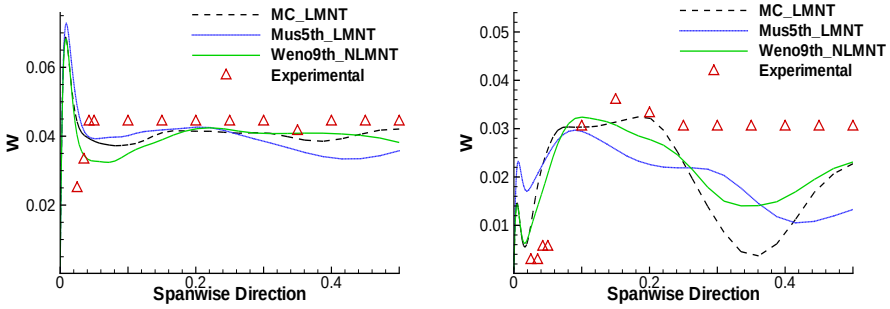

$x = -0.25$, $D = 0.7$ and $D = 0.9$

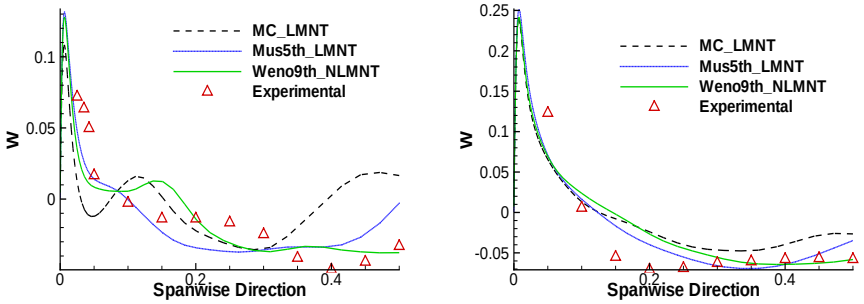

$\theta = 30^o$, $D = 0.1$ and $D = 0.3$

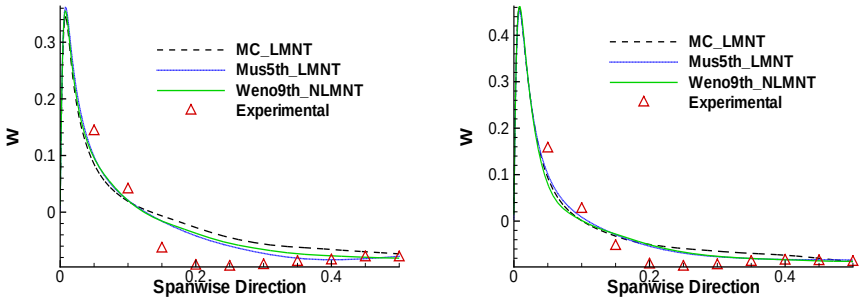

$\theta = 30^o$, $D = 0.5$ and $D = 0.7$

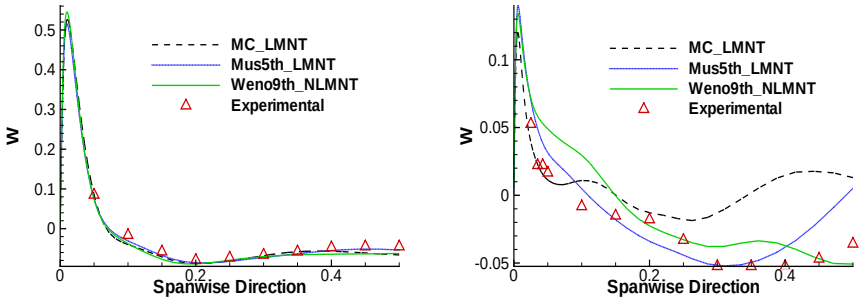

$\theta = 30^o$, $D = 0.9$ and $\theta = 60^o$, $D = 0.1$

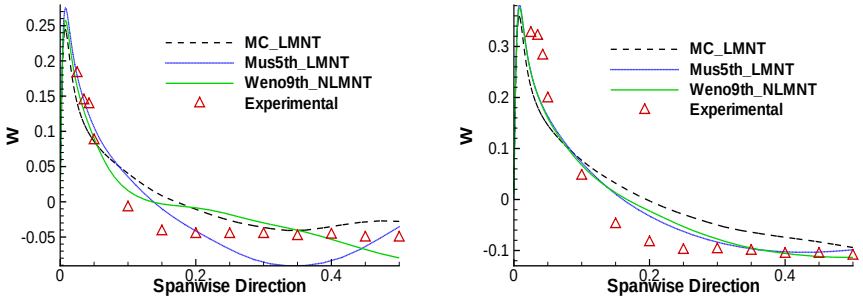

$\theta = 60^o$, $D = 0.3$ and $D = 0.5$

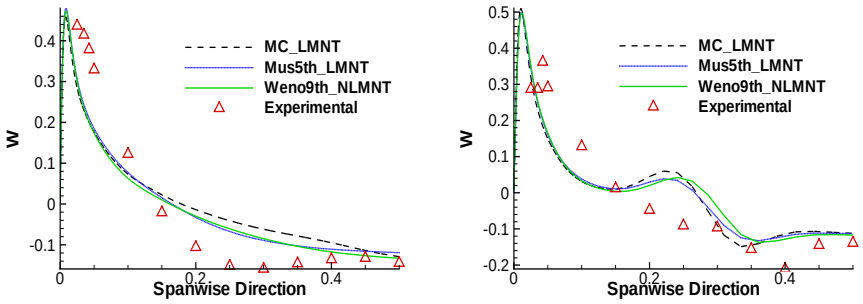

$\theta = 60^o$, $D = 0.7$ and $D = 0.9$

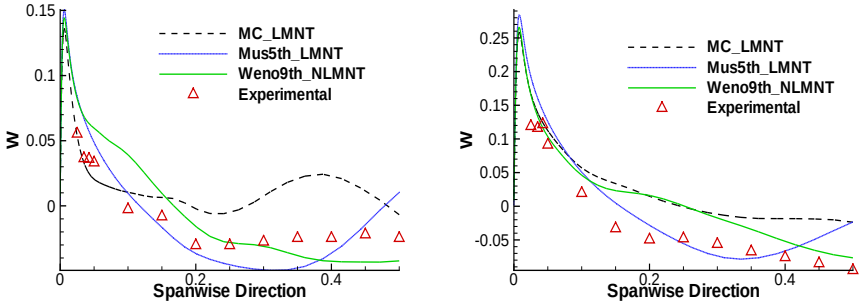

$\theta = 60^o$, $D = 0.7$ and $D = 0.9$

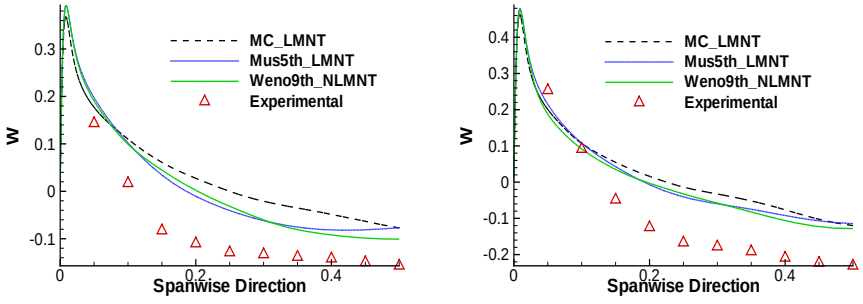

$\theta = 77.5^o$, $D = 0.5$ and $D = 0.7$

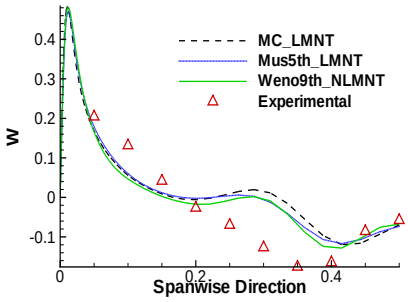

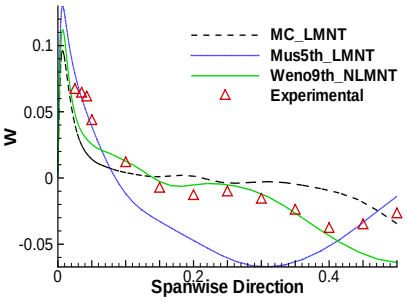

$\theta = 77.5^o$, $D = 0.9$ and $z = 0.25$, $D = 0.1$

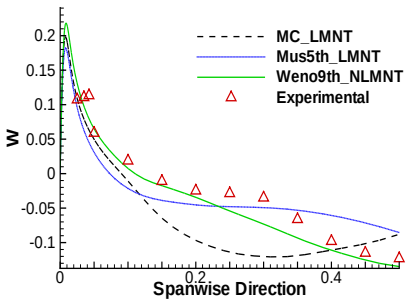

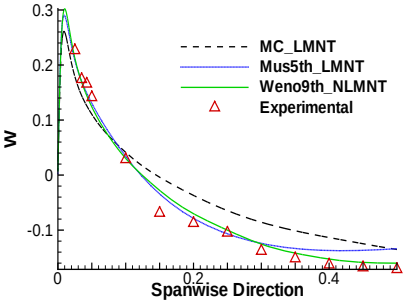

$z = 0.25$, $D = 0.3$ and $D = 0.5$

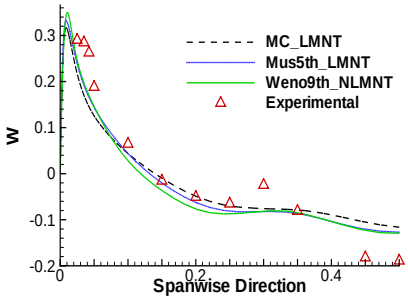

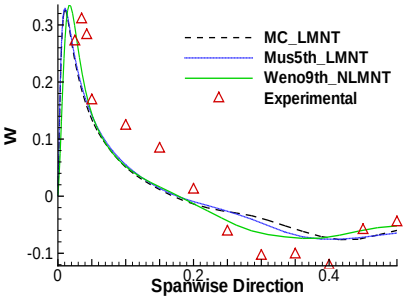

$z = 0.25$, $D = 0.7$ and $D = 0.9$

Streamwise Reynold stresses U_{rms}:

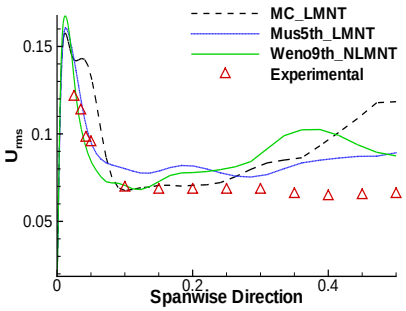

$x = -0.25$, $D = 0.1$

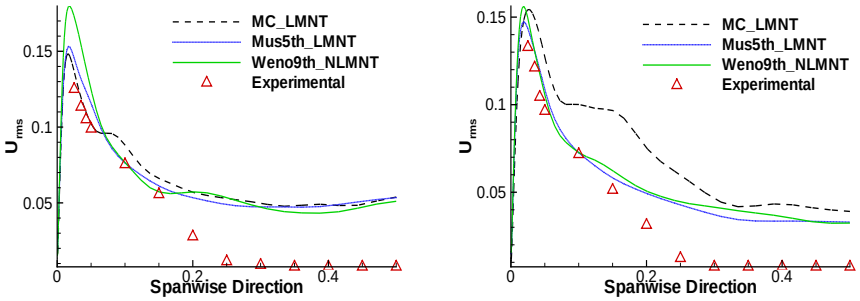

$x = -0.25$, $D = 0.3$ and $D = 0.5$

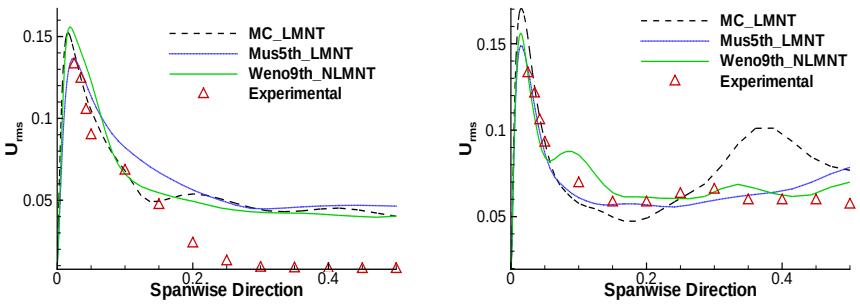

$x = -0.25$, $D = 0.7$ and $D = 0.9$

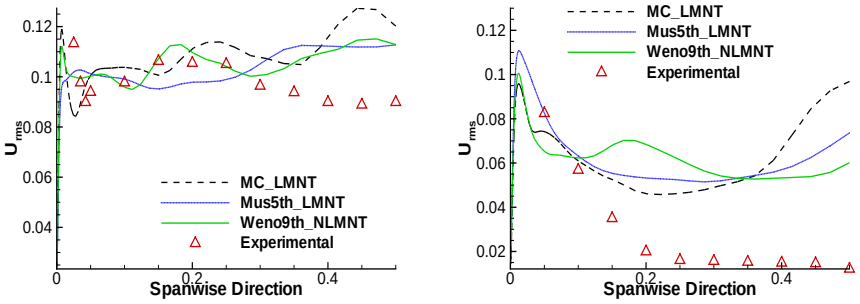

$\theta = 30^o$, $D = 0.1$ and $D = 0.3$

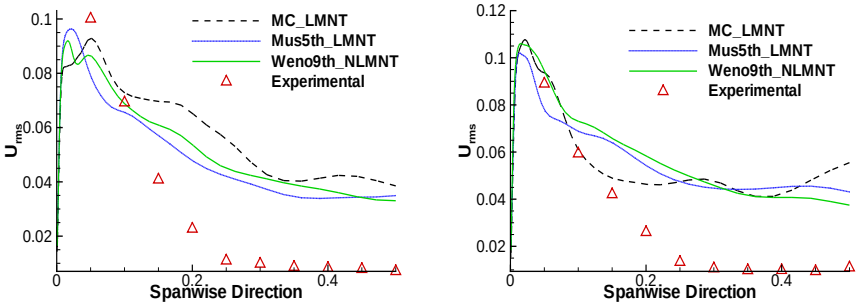

$\theta = 30^o$, $D = 0.5$ and $D = 0.7$

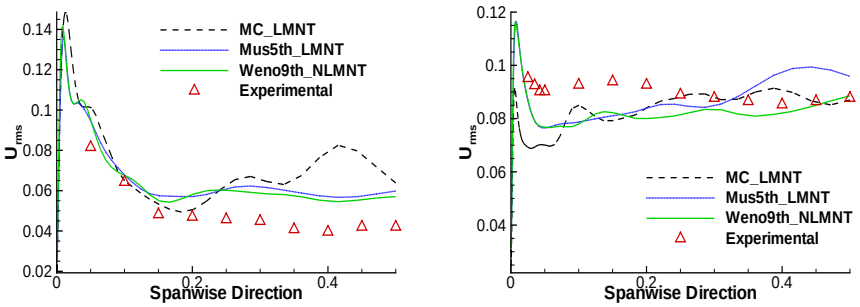

$\theta = 30^o$, $D = 0.9$ and $\theta = 60^o$, $D = 0.1$

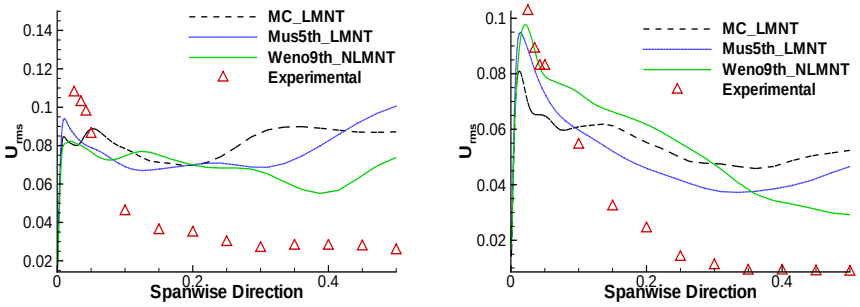

$\theta = 60^o$, $D = 0.3$ and $D = 0.5$

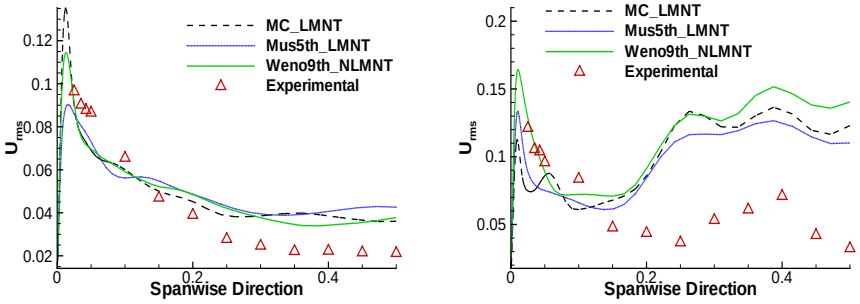

$\theta = 60^o$, $D = 0.7$ and $D = 0.9$

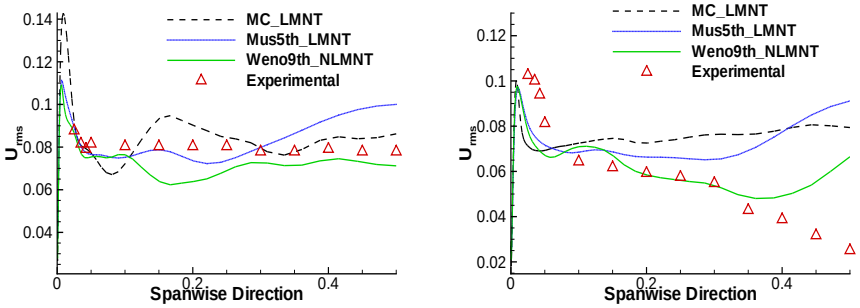

$\theta = 60^o$, $D = 0.7$ and $D = 0.9$

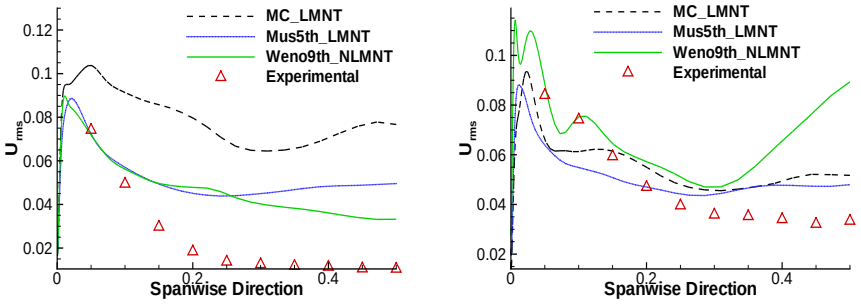

$\theta = 77.5^o$, $D = 0.5$ and $D = 0.7$

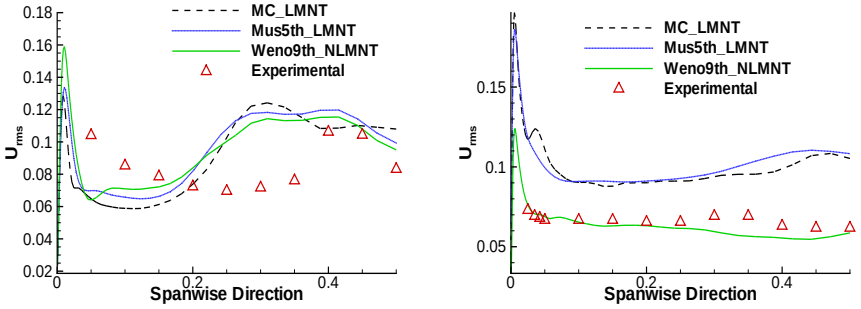

$\theta = 77.5^o$, $D = 0.9$ and $z = 0.25$, $D = 0.1$

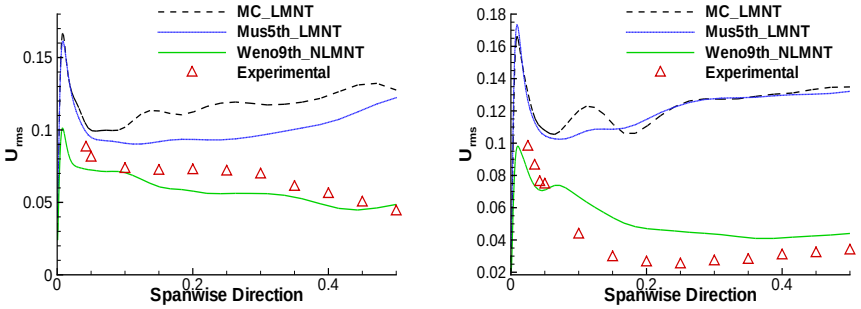

$z = 0.25$, $D = 0.3$ and $D = 0.5$

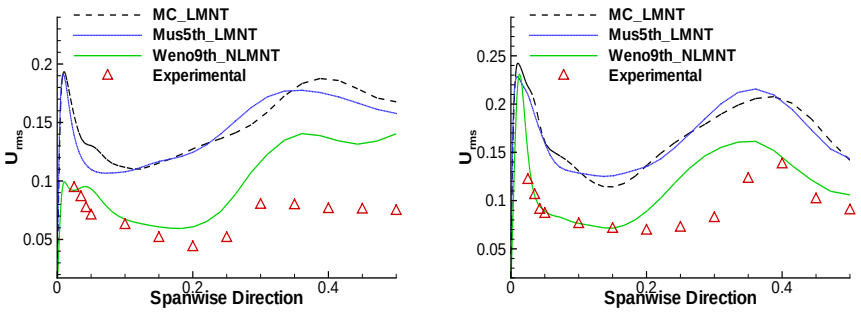

$z = 0.25$, $D = 0.7$ and $D = 0.9$

Streamwise Reynold stresses W_{rms}[1]:

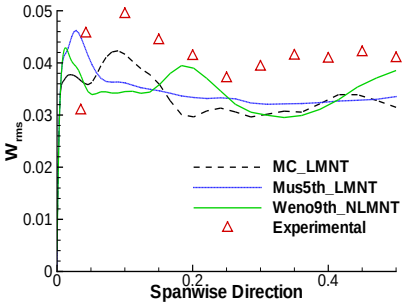

$x = -0.25$, $D = 0.1$

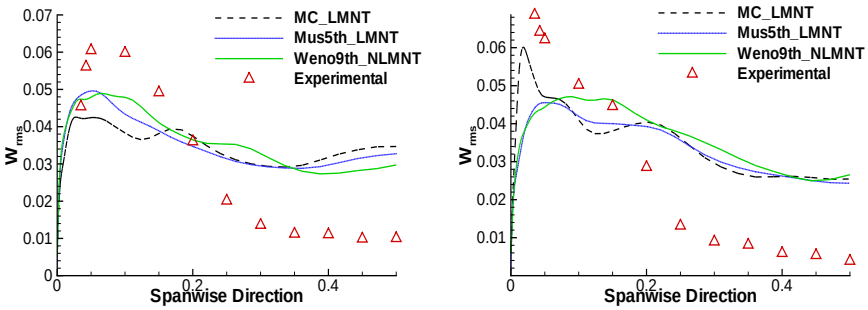

$x = -0.25$, $D = 0.3$ and $D = 0.5$

[1]Some discrepancies can be expected here since comparisons are done using high order statistics of low value variables and this is the reason why the simulation results can be easily affected by the slightest numerical errors. Finally the experimental data include errors as well[107] that again can influence the produced data significantly at these low values.

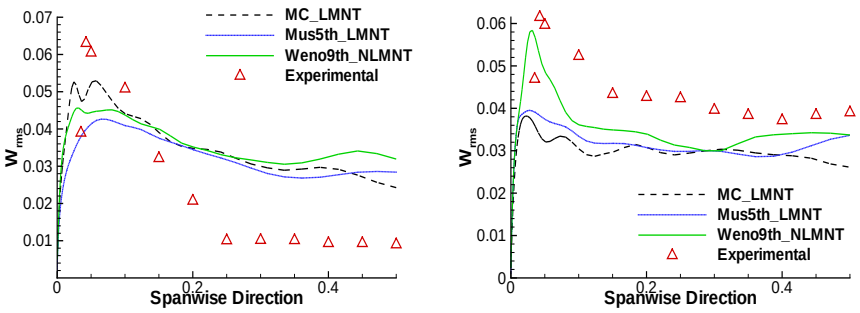

$x = -0.25$, $D = 0.7$ and $D = 0.9$

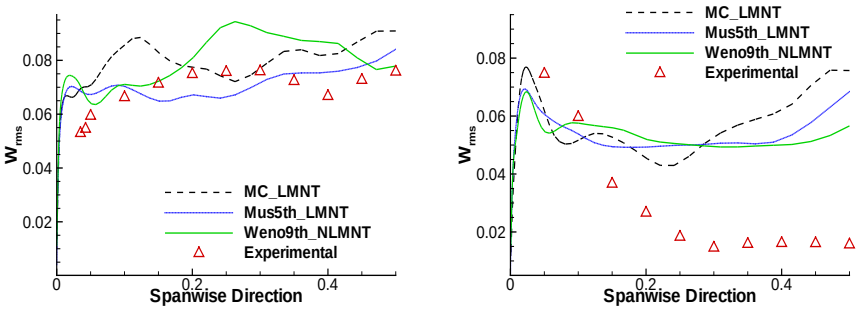

$\theta = 30^o$, $D = 0.1$ and $D = 0.3$

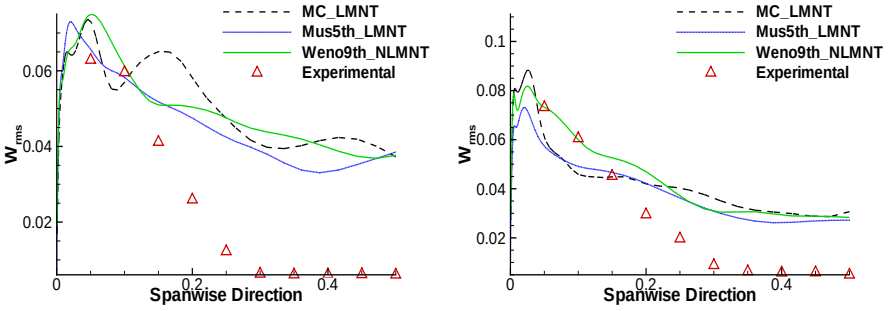

$\theta = 30^o$, $D = 0.5$ and $D = 0.7$

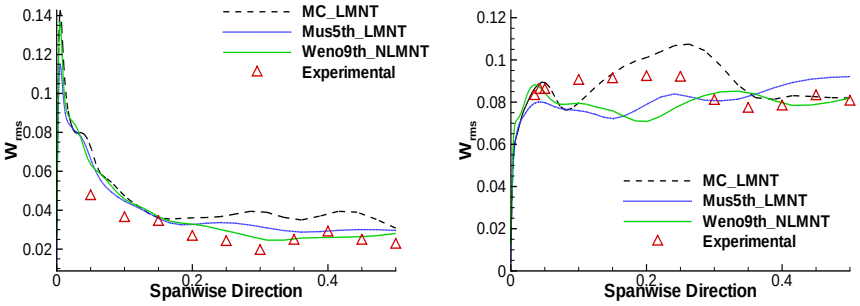

$\theta = 30^o$, $D = 0.9$ and $\theta = 60^o$, $D = 0.1$

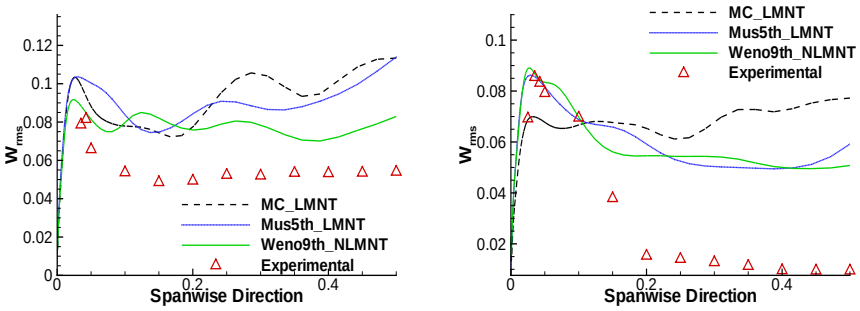

$\theta = 60^o$, $D = 0.3$ and $D = 0.5$

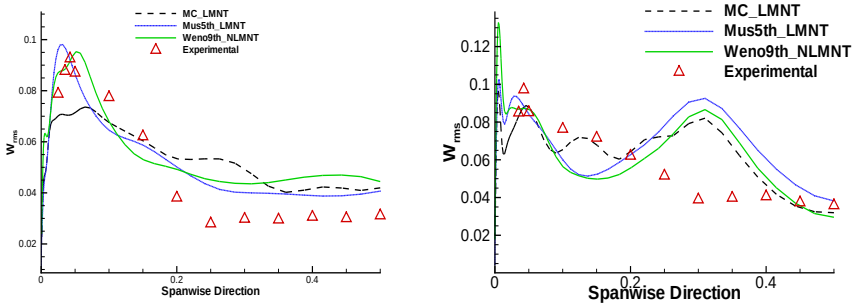

$\theta = 60^o$, $D = 0.7$ and $D = 0.9$

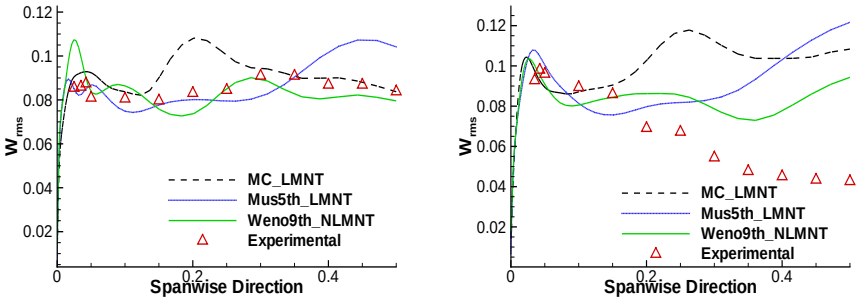

$\theta = 60^o$, $D = 0.7$ and $D = 0.9$

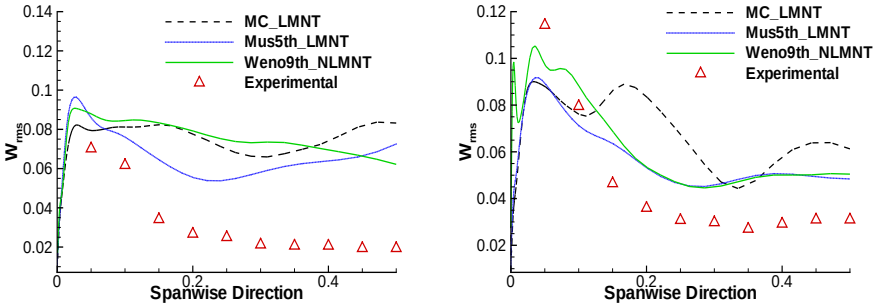

$\theta = 77.5^o$, $D = 0.5$ and $D = 0.7$

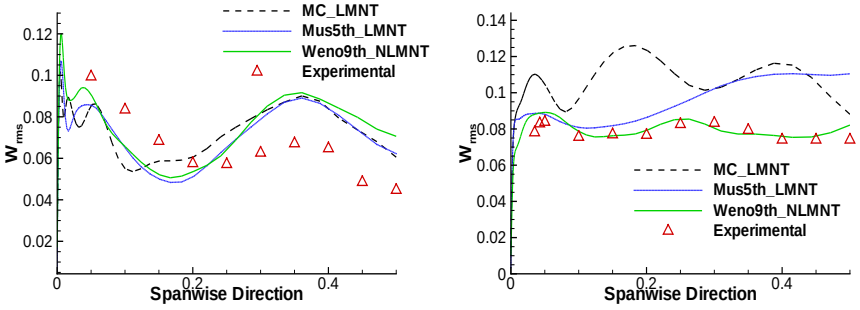

$\theta = 77.5^o$, $D = 0.9$ and $z = 0.25$, $D = 0.1$

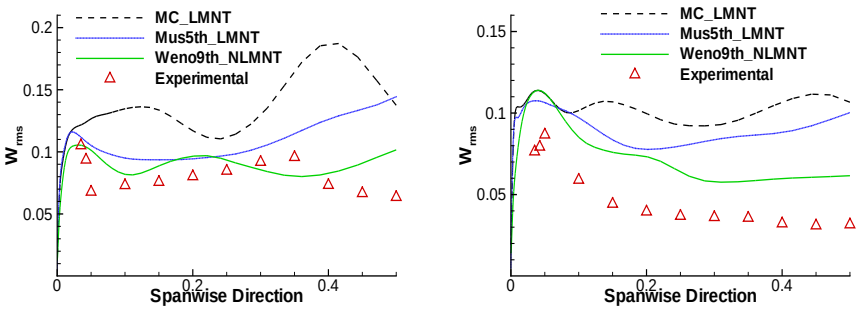

$z = 0.25$, $D = 0.3$ and $D = 0.5$

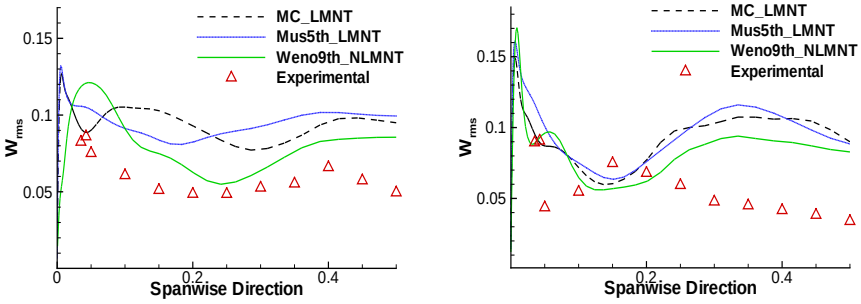

$z = 0.25$, $D = 0.7$ and $D = 0.9$